UFMG

TUNNELING SPECTROSCOPY OF 2D MATERIALS: UNRAVELING THEIR DENSITY OF STATES AND THE RELATIONSHIP WITH LOCAL ATOMIC ENVIRONMENT

Thaís Chagas Peixoto Silva

2020

TUNNELING SPECTROSCOPY OF 2D MATERIALS: UNRAVELING THEIR DENSITY OF STATES AND THE RELATIONSHIP WITH LOCAL ATOMIC ENVIRONMENT

Thaís Chagas Peixoto Silva

Thesis submitted to Universidade Federal de Minas Gerais as a partial requirement for obtaining the Ph.D. degree in Physics.

Supervisor:
Prof. Dr. Rogério Magalhães Paniago
(Universidade Federal de Minas Gerais)

Co-Supervisors:
Prof. Dr. Ângelo Malachias de Souza
(Universidade Federal de Minas Gerais)

Prof. Dr. Carsten Busse
(Universität Siegen)

UFMG

Departamento de Física - ICEx
Universidade Federal de Minas Gerais

March 2020

Dados Internacionais de Catalogação na Publicação (CIP)

S586t Silva, Thaís Chagas Peixoto.
Tunneling spectroscopy of 2D materials: unraveling their density of states and the relationship with local atomic environment. – 2020.
154f., enc. : il.

Orientador: Rogério Magalhães Paniago.
Coorientadores: Ângelo Malachias de Souza e Carsten Busse.
Tese (doutorado) – Universidade Federal de Minas Gerais, Departamento de Física.
Bibliografia: f. 133-154.

1. Espectroscopia de tunelamento. 2. Propriedades eletrônicas. 3. Física do estado sólido.

I. Título. II. Paniago, Rogério Magalhães. III. Universidade Federal de Minas Gerais, Departamento de Física.

Ficha catalográfica elaborada por Romário Martins – CRB6 3595
Biblioteca Professor Manoel Lopes de Siqueira – Departamento de Física - UFMG

UNIVERSIDADE FEDERAL DE MINAS GERAIS
INSTITUTO DE CIÊNCIAS EXATAS
PROGRAMA DE PÓS GRADUAÇÃO EM FÍSICA

ATA DA SESSÃO DE ARGUIÇÃO DA 368ª TESE DO PROGRAMA DE PÓS-GRADUAÇÃO EM FÍSICA, DEFENDIDA POR THAIS CHAGAS PEIXOTO SILVA orientada pelo professor Rogério Magalhães Paniago, para obtenção do grau de **DOUTORA EM CIÊNCIAS, área de concentração física**. Às 13:00 horas de cinco de maio de de dois mil e vinte reuniu-se, por videoconferência, a Comissão Examinadora, composta pelos professores **Rogério Magalhães Paniago** (Orientador - Departamento de Física/UFMG), **Walber Hugo de Brito** (Departamento de Física/UFMG), **Gilberto Medeiros Ribeiro** (Departamento de Ciências da Computação/UFMG), **Roberto Hiroki Miwa** (Instituto de Física/UFU) e **Carsten Busse** (Universidade de Siegen/Alemanha) para dar cumprimento ao Artigo 37 do Regimento Geral da UFMG, submetendo a Mestre **THAIS CHAGAS PEIXOTO SILVA** à arguição de seu trabalho de Tese de Doutorado, que recebeu o título de **"Tunneling spectroscopy of 2D materials: unraveling their density of states and the relationship with local atomic environment ".** A candidata fez uma exposição oral de seu trabalho durante aproximadamente 50 minutos. Após esta, os membros da comissão prosseguiram com a sua arguição, e apresentaram seus pareceres individuais sobre o trabalho, concluindo pela aprovação da candidata.

Belo Horizonte, 05 de Maio de 2020.

Prof. Rogério Magalhães Paniago
Orientador da estudante
Departamento de Física/UFMG

Prof. Walber Hugo de Brito
Departamento de Física/UFMG

Roberto Hiroki Miwa
Instituto de Física/UFU

Prof. Carsten Busse
Universidade de Siegen/Alemanha

Prof. Gilberto Medeiros Ribeiro
Departamento de Ciências da Computação/UFMG

Candidata

Documento assinado eletronicamente por **Walber Hugo de Brito**, **Professor do Magistério Superior**, em 23/11/2020, às 16:08, conforme horário oficial de Brasília, com fundamento no art. 6º, § 1º, do Decreto nº 8.539, de 8 de outubro de 2015.

Documento assinado eletronicamente por **Rogerio Magalhaes Paniago**, **Professor do Magistério Superior**, em 24/11/2020, às 10:03, conforme horário oficial de Brasília, com fundamento no art. 6º, § 1º, do Decreto nº 8.539, de 8 de outubro de 2015.

Documento assinado eletronicamente por **Roberto Hiroki Miwa**, **Usuário Externo**, em 03/12/2020, às 18:11, conforme horário oficial de Brasília, com fundamento no art. 6º, § 1º, do Decreto nº 8.539, de 8 de outubro de 2015.

Documento assinado eletronicamente por **Thais Chagas Peixoto Silva**, **Usuário Externo**, em 10/12/2020, às 17:38, conforme horário oficial de Brasília, com fundamento no art. 6º, § 1º, do Decreto nº 8.539, de 8 de outubro de 2015.

Documento assinado eletronicamente por **Carsten Busse**, **Usuário Externo**, em 15/12/2020, às 18:10, conforme horário oficial de Brasília, com fundamento no art. 6º, § 1º, do Decreto nº 8.539, de 8 de outubro de 2015.

Documento assinado eletronicamente por **Gilberto Medeiros Ribeiro**, **Presidente de comissão**, em 17/12/2020, às 07:44, conforme horário oficial de Brasília, com fundamento no art. 6º, § 1º, do Decreto nº 8.539, de 8 de outubro de 2015.

A autenticidade deste documento pode ser conferida no site https://sei.ufmg.br/sei/controlador_externo.php?acao=documento_conferir&id_orgao_acesso_externo=0, informando o código verificador **0426243** e o código CRC **BB7F1E19**.

Referência: Processo nº 23072.242106/2020-92 SEI nº 0426243

*"*For God so loved the world that he gave his one and only Son, that whoever believes in him shall not perish but have eternal life."

Holy Bible, John 3:16

ACKNOWLEDGEMENTS

There are a number of special people I had the privilege to meet and work with during this stage of my life. I am immensely grateful for all the help and support I have received. Here, I would like to acknowledge and deeply thank each of them.

First of all, I thank God for the countless blessings; for giving me strength, health and skills to accomplish this work. Without You none of this would be possible, as it is written “apart from Me you can do nothing”.

I thank my mother Cinara Peixoto and my grandparents Valdívia Peixoto and Gildésio Peixoto for the unconditional love, invaluable support and constant encouragement they have given me and will continue to do so. You are the basis of everything in my life.

I thank my supervisor Rogério Paniago (UFMG, Brazil) for sharing his knowledge with me and his concern with my academic education. Thank you for giving me the chance to work in all these interesting projects.

I thank my co-supervisor Ângelo Malachias (UFMG, Brazil) for his guidance and constant support, always approaching problems with clever ideas and proposing elegant solutions.

I thank my co-supervisor Carsten Busse (Universität Siegen, Germany) for accepting me in his group, giving me the opportunity to do part of my Ph.D. in Germany under his supervision. Thank you for your complete support and all the scientific discussions.

I thank all the members (including some of its former ones) of the 'Nanoscopia UHV' laboratory (UFMG, Brazil) for the amazing environment of friendship and cooperation: Pedro Gonçalves, Luan Calil, Everton Andrade, Igor Antoniazzi, Lucas Marçal, Yuri Marçal, Samuel Martins, Eduardo Campos, Gilberto Rodrigues Jr., Maria Heiderick, Thiago Carvalho, Aline Winders, Bárbara Rosa, Diogo dos Reis, Ingrid Barcelos, Otávio Alves, Muriel de Pauli, Alejandro Rios and Lorena Rodrigues. I especially thank Pedro Gonçalves for his friendship and his continuous help in all the experiments we have done together and Luan Calil also for his friendship and for his work growing Bi-Te systems.

I thank all the members of the 'AG Experimentelle Nanonophysik' (Universität Siegen, Germany) for the unique environment of friendship and for all the teamwork: Kai Mehlich, Jiaqi Cai, Dennis Rybakowski, Paulus Aleksa, Veronika Blecker, Dina Wilks, Alice Bremerich, Robin Ohmann, Daniela Dombrowski, Joshua Fuhrmann and Madad Abbasli. I especially thank Kai Mehlich for his friendship, for teaching me how to use TuMa III and for the additional measurements of TaS_2; Jiaqi Cai also for his assistance and for all the scientific discussions; and Dennis Rybakowki for his valuable help setting up TuMA III in our new laboratory in Siegen and for his continuous support regarding technical issues.

I thank Mario Mazzoni and Guilherme Ribeiro (UFMG, Brazil) for collaborating to this work with the DFT calculations for the topological insulators project. Thank you for your commitment to this work and for all the scientific discussions we have had. In addition, I also thank Mario Mazzoni for his excellent lectures and his dedication teaching physics the way he does. I thank Guilherme Ribeiro as well for his invaluable support, helping me to understand many concepts concerning topological insulators.

I thank Wendell Simões e Silva (LNLS, Brazil) for the fruitful collaboration concerning the ARPES measurements and his commitment to this work. Thank you also for all the scientific discussions and for helping me to understand the physics behind our experimental data.

I thank Myriano Oliveira Jr. (UFMG, Brazil) and João Marcelo Lopes (Paul-Drude-Institut Festkörperelektronik, Germany) for their contributions to the triangular graphene nanostructures project.

I thank Marta Pelc, Jhon González and Andres Ayuela (Donostia International Physics Center, Spain) for all the contributions added to this work and also for all the scientific discussions we have had regarding the triangular graphene nanostructures project. I also would like to thank you for all the theoretical calculations you have done.

I thank Abdus Samad and Udo Schwingenschlögl (King Abdullah University of Science and Technology, Kingdom of Saudi Arabia) for the calculations of the triangular trimers project.

I thank Juan González and his students (UFMG, Brazil) for the collaboration regarding the GaAs nanowires, providing us with samples to investigate.

I thank Yves Petroff (LNLS, Brazil) for the collaboration on the Bi_4Te_3 project.

I thank Omar Ashour, Zhenglu Li and Steven Louie (University of California, USA) for the calculations in progress on the Bi_4Te_3 project.

I thank Joaquim Mendes (UFV, Brazil) for the collaboration regarding the YIG on graphene project.

I thank Rogério Paniago, Ângelo Malachias, Carsten Busse, Guilherme Ribeiro and Wendell Simões e Silva for proofreading different parts of this thesis and for all the suggestions I have received from them.

I thank Caio Tavares for carefully proofreading this whole Ph. D. thesis.

I thank Gustavo Sáfar (UFMG, Brazil) for the contribution to my education and constant support.

I thank Ullrich Pietsch (Universität Siegen, Germany) for the collaboration regarding the GaAs nanowires.

I thank Antônio Pádua e Rubens Menezes (UFMG, Brazil) for the technical support given to our laboratory.

I thank Leandro Lemos, Klaus Krambrock and staff (UFMG, Brazil) for the liquid nitrogen/helium supply.

I thank Thiago Albegaria and the entire working group of the mechanical workshop of UFMG for all the support given to our laboratory.

I thank Michael Ziolkowski, Waldemar Stroh and the entire working group of the electronic workshop of the Universität Siegen for the support regarding all the technical issues we have faced in our laboratory.

I thank the entire working group of the mechanical workshop of the Universität Siegen for the support given to our laboratory.

I thank Rogério Paniago, Marcus Baeta e Júlio César de Souza (UFMG, Brazil) for giving me my first opportunity to work in a laboratory as a monitor of experimental physics. What I learned from this experience, which opened up the doors for everything that came next, was essential.

I thank my family for the immense love, encouragement and constant support: Gilva Teixeira, Gláucia Tavares, Hudson Peixoto, Zélia Peixoto, Adla Maria, Adelaide Andrade, Helton Tavares, Ricardo Teixeira and all my other relatives. I cannot thank you enough. I also thank our good friend Maria Januario and my beloved dogs Mia and Sunny.

I thank my cousins for being constantly present in my life making my days certainly happier: Caio Tavares, João Tavares, Lucas Peixoto, Gabriel Peixoto, Athos Barreiros and Davi Barreiros. You are the joy of my life.

I thank Wilfried Klauer, Roland Hauck and Elena Hauck for being like a family to me in Germany. You have done so much more for me that I can put into words. Special thanks to Wilfried for the uncountable journeys with our bikes and for being a friend for life.

I thank Welberth Magalhães for being an extraordinary friend always present despite the miles away. I deeply value our friendship.

I thank Gabriela Guimarães for her friendship and excellent German lessons. Our conversations always made me see life from a different perspective.

I thank my dear friends and colleagues for the good moments and help over the years: Ana Clara Pimenta, Bábara Elza Nogueira, Samuel Vasconcelos, Renan Cunha, Paula

D'Ávila, Filomeno Aguiar Jr., Sheilla de Oliveira, Raphaela de Oliveira, Danielle Ferreira, Flávio Noronha, Leonel Meireles, Nathan Giovanni, Matheus Matos, Nilton Neto and Angelus Simões. I apologize if I forgot someone.

I also thank my dear friends and colleagues from Universität Siegen that made me deeply appreciate my stay in Germany: Lisa Randolph, Ali Al Hassan, Mahmoud Al Humaidi, Danial Bahrami, Mohammad Mostafavi, Arman Davtyan, Hendrik Rahmann, Ahmed Al-Masoodi, Clementine Lovato, Sonja Timmermann, Kevin Lopata, Anna-Lena Becker and Mohammad Shokr.

I thank Renan Cunha, Paula D'Ávila, Matheus Kim, Tiago Abreu, Alexandre Soares and Daniel Elias for the good discussions we had regarding faith and science. You are a great source of support to me.

I thank Luiz Cury (UFMG, Brazil) for his friendship and support.

I thank Andreas Ketterer (Universität Siegen, Germany) for helping me with the rental process in Germany and Michaela Krex (Universität Siegen, Germany) for helping me to find a follow-up tenant.

I thank the librarians Shirley Maciel da Silva and Gislene Rodrigues, along with all the staff of the library Prof. Manoel Lopes de Siqueira (UFMG, Brazil), for their attention and organization of this space.

I thank Kerstin Semma (Universität Siegen, Germany) for all the support with paperwork, always very helpful.

I thank the Physics Secretariat, in particular Juliana Miranda Silva, Ana Luiza de Souza and Marília Pacheco Diniz (UFMG, Brazil) for their attention and support with all the paperwork.

I thank Brazilian Synchrotron Light Laboratory (LNLS, Brazil) for the experimental support. In particular, I thank the staff of XRD2 and PGM beamlines for all their help.

I thank the funding agencies FAPEMIG, INCT-Nanocarbono, CNPq and CAPES (PDSE 88881.188652/2018-01) for the financial support I received during different stages of my academic life.

TABLE OF CONTENTS

FREQUENTLY USED SYMBOLS AND ABBREVIATIONS

STM ..... Scanning tunneling microscopy

STS..... Scanning tunneling spectroscopy

ARPES ..... Angle-resolved photoemission spectroscopy

2D..... Two-dimensional

DFT ..... Density functional theory

LEED ..... Low-energy electron diffraction

3D..... Three-dimensional

TMDC ..... Transition metal dichalcogenide

PSD..... Phase-sensitive detection

AC..... Alternating current

DC..... Direct current

QMS ..... Quadrupole mass spectrometer

CVD ..... Chemical vapor deposition

CCD ..... Charge coupled device

MCP..... Microchannel plate

MLG..... Monolayer graphene

BL (in chapter IV)..... Buffer layer

MLG + BL ..... Partially attached bilayer graphene

BLG ..... Bilayer graphene

CTR ..... Crystal truncation rod

LDOS ..... Local density of states

BL (in chapter V) ..... Bismuth bilayer

QL ..... Quintuple-layer

PDOS ..... Projected density of states

fcc ..... Face-centered cubic

hcp ..... Hexagonal close-packed

RESUMO

Neste trabalho utilizamos as técnicas de microscopia (STM) e espectroscopia de tunelamento (STS), além da espectroscopia de fotoemissão resolvida em ângulo (ARPES), para estabelecer conexões entre as propriedades estruturais e eletrônicas de materiais bidimensionais (2D). Em particular, esta tese é composta por três projetos complementares relacionados a três diferentes materiais, a saber, nanoestruturas de grafeno, isolantes topológicos e dicalcogenetos de metais de transição.

No trabalho sobre grafeno observou-se uma resposta eletrônica *dual* em nanoestruturas triangulares deste material. Relatamos a observação dessas nanoestruturas, que resultam de falhas de empilhamento prolongadas no substrato de SiC, e seus efeitos nas camadas de grafeno que se formam sobre elas. Medidas espectroscópicas revelaram respostas eletrônicas distintas em uma fração das nanoestruturas observadas como consequência de um processo de intercalação de hidrogênio incompleto. Essa observação resulta do fato de que a camada inferior da bicamada de grafeno ainda está ligada ao substrato em algumas áreas. Tal configuração gera, portanto, regiões em que a bicamada de grafeno apresenta uma assinatura eletrônica que se assemelha a de uma única folha de grafeno.

Também será reportada aqui a síntese, através do método de Bridgman, do isolante topológico Bi_4Te_3. Caracterizações feitas utilizando a técnica de difração de raios X revelaram a coexistência do Bi_4Te_3 com fases minoritárias de Bi_2 e Bi_2Te_3. Uma análise teórica, feita através da teoria do funcional da densidade (DFT), permitiu um estudo da estrutura de bandas e da densidade de estados do Bi_4Te_3 bem como de seus constituintes. A combinação das técnicas de STM e STS, através da análise de perfis de

altura e de espectros de densidade de estados, tornou possível ainda a identificação de regiões de diferentes terminações do Bi_4Te_3 (Bi_2 e Bi_2Te_3). Além disso, medidas de ARPES se assemelham bastante a assinatura do Bi_4Te_3 com terminação em pentacamada. Contornos de energia constante revelaram ainda um formato hexagonal similar a um floco de neve com braços mais alongados se comparado diretamente ao Bi_2Te_3.

Por fim, na última parte desta tese apresentaremos também um estudo sobre filmes de TaS_2 crescidos sobre substratos de Au(111). Esse material foi sintetizado através da evaporação de tântalo em Au(111) numa atmosfera de H_2S (usado como fonte de enxofre) e caracterizado utilizando difração de elétrons de baixa energia (LEED) e STM/STS. Verificou-se que sob condições específicas de crescimento (altas temperaturas de aquecimento e pressão de H_2S) o número de ilhas sob o substrato é significativamente reduzido dando lugar à formação aglomerados nanométricos de S. O aparecimento desses aglomerados de morfologia triangular distorce o padrão de reconstrução *herringbone* do substrato de Au(111). Imagens de STM atomicamente resolvidas revelaram que esses aglomerados apresentam diferentes orientações dependendo da região da superfície de Au(111) na qual eles estão localizados e espectros de tunelamento exibiram um comportamento semicondutor.

P A L A V R A S – C H A V E: microscopia/espectroscopia de tunelamento, espectroscopia de fotoemissão resolvida em ângulo, propriedades estruturais e eletrônicas, grafeno, isolantes topológicos, dicalcogenetos de metais de transição, nanoestruturas, sistemas de Bi-Te, TaS_2, aglomerados nanométricos triangulares.

ABSTRACT

In this work we have used scanning tunneling microscopy/spectroscopy (STM/STS) and angle-resolved photoemission spectroscopy (ARPES) to study the interplay between atomic and electronic structure of two-dimensional (2D) materials. In particular, this thesis is set of three complementary projects, related to three different materials, namely, triangular graphene nanostructures, topological insulators and transition metal dichalcogenides.

First, a dual electronic response of triangular graphene nanostructures grown on SiC was investigated. We report on the observation of triangular nanostructures resulting from extended stacking faults in the SiC substrate and their effects on graphene layers that are formed on top of them. Spectroscopic measurements revealed distinct electronic responses as a consequence of the incomplete hydrogen intercalation process in a fraction of the observed nanostructures, in which the bottom layer of the bilayer graphene is still bonded to the substrate. Such a configuration generates regions where the bilayer graphene presents an electronic signature that resembles those of single layer graphene systems.

In addition, the topological insulator Bi_4Te_3, synthetized using the Bridgman method, was also investigated here. X-ray diffraction measurements confirmed the formation of Bi_4Te_3 as a major phase in a system also composed of minority phases of Bi_2 and Bi_2Te_3. Density functional theory (DFT) of Bi_4Te_3 and its constituents allowed, through the calculation of their band structures and density of states, for a systematic study of their electronic properties. The combined use of STM and STS, analyzing height-profiles

and conductance spectra, permitted us to identify different terminations of Bi_4Te_3 (Bi_2 and Bi_2Te_3) with different electronic responses. ARPES measurements highly resemble quintuple-layer terminated Bi_4Te_3 signatures. Constant energy contours also reveal a hexagonal shape similar to a snowflake with more elongated branches when directly compared to Bi_2Te_3.

Finally, in the last part of this thesis, a study of TaS_2 films grown on Au(111) is presented. This material was synthetized through the evaporation of tantalum on Au(111) in a background of H_2S (used as source of sulfur) and it was investigated using low-energy electron diffraction (LEED) and STM/STS. It was found that under specific growth conditions (high annealing temperatures and H_2S pressure) the quantity of TaS_2 islands on the substrate is significantly reduced giving rise to a number of S trimers. The emergence of these trimers with triangular morphology distort the Au(111) herringbone reconstruction. Atomically-resolved STM images revealed distinct orientations of the trimers depending on the regions of the Au(111) surface where they sit and tunneling spectrum exhibits a semiconducting behavior.

K E Y W O R D S: scanning tunneling microscopy/spectroscopy, angle-resolved photoemission spectroscopy, structural and electronic properties, graphene, topological insulators, transition metal dichalcogenides, nanostructures, Bi-Te systems, TaS_2, triangular trimers.

I.

INTRODUCTION

The discovery of graphene, a two-dimensional (2D) material composed of carbon atoms organized in a honeycomb structure, has attracted the attention of the scientific community due to its unique properties. Particularly important is its approximately linear dispersion relation for energies close to the Fermi level, which gives electrons a massless behavior of Dirac fermions [1-4]. Over the past years an extensive research has been carried out aiming to investigate its structural and electronic properties under the most diverse conditions such as, for example, synthetizing it on different types of substrates and subjecting it to external fields and stresses [5-10]. A number of studies, both theoretical and experimental, have revealed remarkable properties not only of graphene on distinct platforms, but also of graphene nanostructures, nanoribbons and quantum dots. In addition to its ballistic transport, high electron mobility at room temperature [11-15], moderate chemical inertness [15] and high thermal conductivity [16], it was found that free-standing graphene is much stronger than steel assuming the same thickness [15, 17, 18]. Also, scientific research revealed that graphene islands with zigzag terminations can host spin-polarized states [19] and that graphene quantum dots are able to confine Dirac fermions [20]. Furthermore, graphene nanoribbons may be used for DNA translocations [21], molecular band gap engineering [22] and may present magnetic order at room temperature [23]. These are just a few examples of the properties of

graphene and much more can still be further explored using the latest advanced experimental tools.

In addition to these remarkable properties, there are important limiting features considering practical application in nanoelectronics devices, one of which: the absence of an electronic band gap. Usually this can be overcome, but not without decreasing its mobility [24]. This is one of the reasons that drove and renewed the interest of the scientific community in other low-dimensional materials. In this context, one particular class of materials became very important: the layered materials such as topological insulators, transition metal dichalcogenides, phosphorene, silicene, hexagonal boron nitride among others. Similar to graphene, which can be obtained from graphite through mechanical cleavage, other layered materials also can be reduced to thin films through simple procedures like scotch tape exfoliation. This is a consequence of the fact that the atomic layers are connected, in the out-of-plane direction, through van der Waals interactions [25]. Furthermore, the important advances established in sample preparation of thin films since the rise of graphene allowed the optimized epitaxial growth of a number of distinct classes of quasi 2D materials on different types of substrates in ultra-high vacuum conditions. This enabled the study of structural and electronic properties of these systems using various experimental techniques without unwanted contamination sources that could modify their intrinsic properties.

Three-dimensional topological insulators are known to present an electronic band gap separating their conduction and valence bulk bands and spin-polarized surface states, making them promising candidates for spintronic devices [26-28]. These properties make them insulators in the bulk, but conductors at the surface. This is a consequence of a strong spin-orbit coupling, more significative in heavy materials. Such a fact originates a band-inversion mechanism that results in the emergence of surface states between the conduction and valence bulk bands of the material [29, 30]. Some of the properties that make them attractive include high mobility, low power dissipation, spin-polarized electrons, quantum spin Hall effect among others [31].

Since the first generation of topological insulators has risen with $Bi_{1-x}Sb_x$ binary alloys, which are not ideal for practical applications due to their complex surface structure

and narrow band gap [31-33], important progresses have been achieved starting the second generation of topological insulators. Some materials that belong to this generation are Bi_2Se_3, Bi_2Te_3 and Sb_2Te_3 [34]. The experimental realization of these compounds, accompanied by the verification of their simple band structure through angle-resolved photoemission spectroscopy measurements, was a significative step. In the case of Bi_2Se_3 and Bi_2Te_3 the surface states have a linear dispersion relation, similar to graphene, but here they are localized close to the Γ point of the Brillouin zone [35, 36]. These findings boosted more research in the area, stimulating a number of theoretical and experimental studies on the subject since there is still a lot to be understood.

Transition metal dichalcogenides are formed of a transition metal (M) and a chalcogen (X) in a formula MX_2 and, depending on their composition and atomic coordination, they can host distinct properties [37-39]. In particular, the electronic response of layered transition metal dichalcogenides may range from semiconductor to a metallic electronic response. Also, a number of properties that are thickness-dependent have a direct influence on the study of thin films over materials in bulk form. In the case of MoS_2, for instance, the evolution of the band gap from indirect to direct as the number of layers is reduced makes this material attractive for nanophotonic devices [40]. Moreover, atomic defects introduced in monolayers of transition metal dichalcogenides have been extensively investigated as quantum emitters [41-43]. Differently, metallic transition metal dichalcogenides like TaS_2 exhibit properties of superconductivity and charge density waves [44-46]. Different materials of this class can also be combined both in-plane as well as out-of-plane forming heterostructures representing also an important platform for device applications [47-50].

Considering the content above, in order to incorporate these classes of materials into electronic devices, an in-depth comprehension of how their properties are modified under different conditions is required. In this context, experimental research, using the most varied techniques, plays a crucial role in assisting and unraveling the understanding of the interplay between the local atomic environment and electronic properties, including band structure and density of states.

This thesis, which is a set of three complementary projects of three different materials, aims to build up the scientific knowledge about 2D materials. It is organized as follows: in chapter II an overview of the layered materials studied in this work is presented. The basic theoretical inputs about graphene, topological insulators and transition metal dichalcogenides are introduced, aiming to familiarize the reader with important concepts necessary to better comprehend the experimental works presented in the following chapters. In chapter III the major experimental techniques used in this work, i. e. scanning tunneling microscopy/spectroscopy and angle-resolved photoemission spectroscopy are presented and discussed. In chapter IV structural and electronic properties of graphene nanostructures on SiC substrates are examined. The influence of the stacking of bilayers and quintuple-layers on the electronic response of the topological insulator Bi_4Te_3 is explored in chapter V. Finally, the self-assembly of triangular S trimers on Au(111) substrates is investigated in chapter VI. Summary and outlooks are presented in chapter VII. Finally, a list of publications and references is presented in chapters VIII and IX, respectively.

II.

LAYERED MATERIALS

This chapter contains an overview of the fundamentals of the layered materials investigated in this work. Theoretical inputs will be demonstrated about graphene, topological insulators and transition metal dichalcogenides. These discussions are particularly important to understanding the experimental results shown in the following chapters.

2.1 GRAPHENE

A. K. Geim and K. S. Novoselov were awarded the Nobel Prize in Physics in 2010 after isolating and characterizing graphene, a two-dimensional material composed of carbon atoms organized in a honeycomb lattice [10, 51, 52]. This important achievement represents a great breakthrough and it was followed by a number of other studies that revealed interesting properties like high thermal [16] and electrical conductivity [12], high mechanical resistance [15, 17, 18], among others, that increased the interest of the scientific community. In this section we use the crystal structure of this material to calculate its dispersion relation close to the K point of the first Brillouin zone as well as its density of states.

2.1.1 ATOMIC STRUCTURE

In this two-dimensional material the carbon atoms have sp^2 hybridization and, as a consequence, graphene has a honeycomb lattice [53, 54]. See the scheme shown in Fig. 2.1.

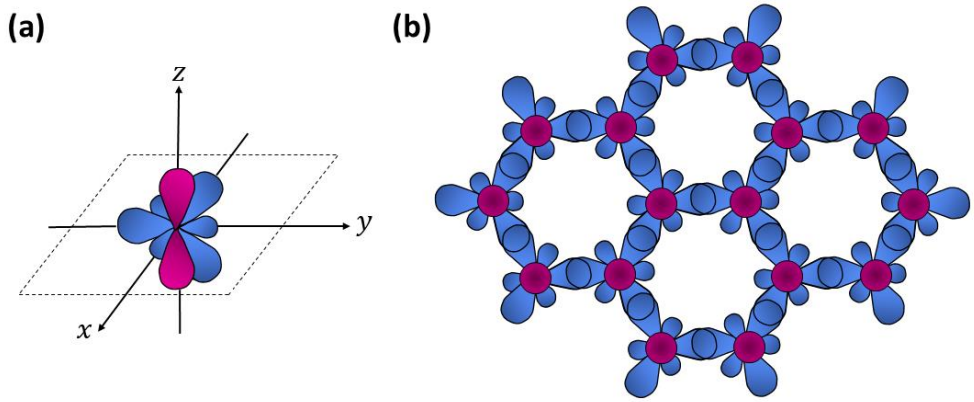

FIG. 2.1 – (a) Schematic view of the sp^2 hybridization. (b) Honeycomb lattice of graphene showing its electronic orbitals (top view). Figure based on reference [54].

The honeycomb lattice of graphene is composed of two interpenetrating triangular Bravais sublattices, namely, A and B [53, 54]. In addition, its unit cell has two carbon atoms, each of which belongs to one of these two sublattices (see Fig. 2.2).

Moreover, the interatomic distance is $a = 0.142$ nm and the primitive vectors, $\boldsymbol{a_1}$ and $\boldsymbol{a_2}$, form an angle of 60°. According to the coordinate system illustrated in Fig. 2.2 these vectors can be written as [53, 54]:

$$\boldsymbol{a_1} = \frac{a}{2}\left(3\boldsymbol{x} + \sqrt{3}\boldsymbol{y}\right) \quad \text{and} \quad \boldsymbol{a_2} = \frac{a}{2}\left(3\boldsymbol{x} - \sqrt{3}\boldsymbol{y}\right). \tag{2.1}$$

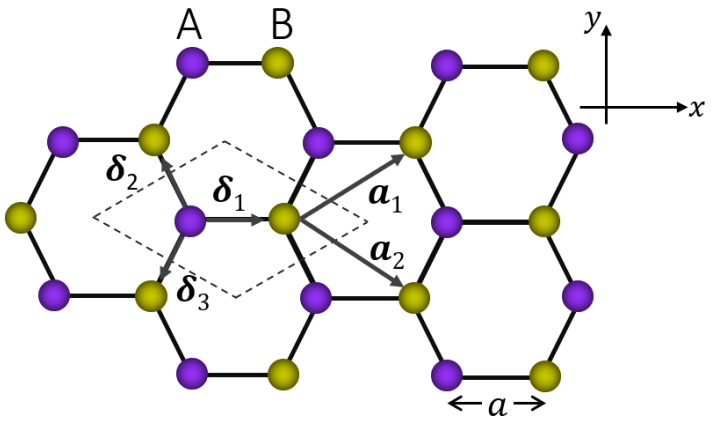

FIG. 2.2 – (a) Honeycomb lattice of graphene showing its unit cell (dashed rhombus), the primitive vectors ($\boldsymbol{a_1}$ and $\boldsymbol{a_2}$) and the nearest-neighbor vectors ($\boldsymbol{\delta}$). The carbon atoms of sublattices A and B are colored purple and yellow, respectively. The interatomic distance, $a = 0.142$ nm, is also indicated.

One can define high symmetry points in the first Brillouin zone, i. e. Γ, K, K' and M (see Fig. 2.3), which will be especially useful in representing its band structure. In addition, the primitive vectors of the reciprocal lattice are:

$$\boldsymbol{b_1} = \frac{2\pi}{3a}\left(\boldsymbol{k_x} + \sqrt{3}\boldsymbol{k_y}\right) \quad \text{and} \quad \boldsymbol{b_2} = \frac{2\pi}{a}\left(\boldsymbol{k_x} - \sqrt{3}\boldsymbol{k_y}\right). \tag{2.2}$$

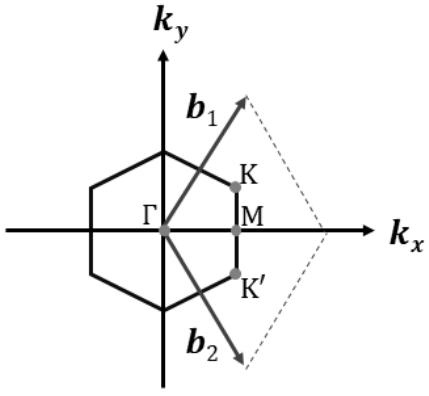

FIG. 2.3 – (a) Scheme of the first Brillouin zone of graphene. The primitive vectors of the reciprocal lattice ($\boldsymbol{b_1}$and $\boldsymbol{b_2}$) and high symmetry points (Γ, K, K' and M) are indicated.

2.1.2 DISPERSION RELATION

In the simplest approximation to describe the dispersion relation of graphene close to the Fermi level one can consider only the hopping of electrons between orbitals perpendicular to the atomic plane (i. e. between different sublattices) with energy $V_{pp\pi}$. Let us consider the state that describes an A/B-sublattice electron belonging to the unit cell identified by the vector $\boldsymbol{R_n}$, as [53, 54]:

$$| n, (A \text{ or } B)\rangle. \tag{2.3}$$

In the nearest-neighbor tight-binding approximation, demonstrated here, the Hamiltonian that describes the hopping between a single electron among orbitals perpendicular to the atomic plane can be written as [53, 54]:

$$H = V_{pp\pi} \sum_{<n,m>} | n, A\rangle\langle m, B | + h.c., \tag{2.4}$$

in which the left-hand side of the first term represents the creation of an electron belonging to the orbital perpendicular to the atomic plane in an A-sublattice and the right-hand side is related to the annihilation of an electron in a B-sublattice. Thus, the first term of this sum describes hopping of an electron from a B-sublattice to an A-sublattice. Also, $V_{pp\pi}$, as previously mentioned, corresponds to energy associated with this electronic transition and is commonly referred to as hopping element. The Hermitian conjugate indicates the reverse process and the total Hamiltonian is obtained considering this effect throughout the crystal lattice, i. e. summing over m and n [53, 54].

To obtain an analytical expression of the dispersion relation of graphene is necessary to replace $| n, A\rangle$ by its Fourier transform:

$$| n, A\rangle = \frac{1}{\sqrt{N}} \sum_{\boldsymbol{k}} e^{i\boldsymbol{k}\boldsymbol{R_n}} | \boldsymbol{k}, A\rangle, \tag{2.5}$$

in which N is a normalization factor related to the number of atoms.

Repeating this procedure for $\langle m, B |$ and replacing it in the expression 2.4, one obtains [53, 54]:

$$H = V_{pp\pi} \sum_{\boldsymbol{k},\boldsymbol{k'}} | \boldsymbol{k}, A\rangle\langle \boldsymbol{k'}, B | \frac{1}{N} \sum_{<n,m>} e^{i(\boldsymbol{k}\boldsymbol{R_n} - \boldsymbol{k'}\boldsymbol{R_m})} + h.c. \tag{2.6}$$

It is possible to simplify this expression introducing the nearest-neighbor vectors, $\boldsymbol{\delta}$, as depicted in Fig. 2.2, and taking into account the relation $\boldsymbol{R_m = R_n + \delta}$. One can write:

$$\frac{1}{N}\sum_{<n,m>} e^{i(\boldsymbol{kR_n - k'R_m})} = \frac{1}{N}\sum_{n,\delta} e^{i[\boldsymbol{kR_n - k'(R_n+\delta)}]}$$

$$= \sum_{\delta} e^{-i\boldsymbol{k'\delta}} \frac{1}{N}\sum_{n} e^{i\boldsymbol{(k-k')R_n}}. \tag{2.7}$$

Considering yet $\sum_{\boldsymbol{\delta}} e^{-i\boldsymbol{k'\delta}} = \gamma_{\boldsymbol{k'}}$ and using the relation $\frac{1}{N}\sum_n e^{i\boldsymbol{(k-k')R_n}} = \delta_{\boldsymbol{k,k'}}$ one obtains [53, 54]:

$$H = V_{pp\pi}\sum_{\boldsymbol{k}} (|\, \boldsymbol{k}, A\rangle\langle \boldsymbol{k}, B \,|\, \gamma_{\boldsymbol{k}} + |\, \boldsymbol{k}, B\rangle\langle \boldsymbol{k}, A \,|\, \gamma_{\boldsymbol{k}}{}^{*}). \tag{2.8}$$

The matrix elements of H are:

$$\langle \boldsymbol{k}, A \,|\, H \,|\, \boldsymbol{k}, A\rangle = 0,$$

$$\langle \boldsymbol{k}, B \,|\, H \,|\, \boldsymbol{k}, B\rangle = 0,$$

$$\langle \boldsymbol{k}, A \,|\, H \,|\, \boldsymbol{k}, B\rangle = V_{pp\pi}\gamma_{\boldsymbol{k}},$$

$$\langle \boldsymbol{k}, B \,|\, H \,|\, \boldsymbol{k}, A\rangle = V_{pp\pi}\gamma_{\boldsymbol{k}}{}^{*}.$$

Thus, one can simply write H using matrix notation as:

$$H = \sum_{\boldsymbol{k}} \begin{pmatrix} 0 & V_{pp\pi}\gamma_{\boldsymbol{k}} \\ V_{pp\pi}\gamma_{\boldsymbol{k}}{}^{*} & 0 \end{pmatrix}. \tag{2.9}$$

Solving the Schrödinger equation for this problem, one obtains the following eigenvalues of H, $E_{\pm}(\boldsymbol{k})$:

$$E_{\pm}(\boldsymbol{k}) = \pm V_{pp\pi}\,|\,\gamma_{\boldsymbol{k}}\,|. \tag{2.10}$$

One can also calculate the value of $\gamma_{\boldsymbol{k}}$ [53, 54]:

$$\gamma_{\boldsymbol{k}} = \sum_{\boldsymbol{\delta}} e^{-i\boldsymbol{k\delta}} = e^{-i\boldsymbol{k\delta_1}} + e^{-i\boldsymbol{k\delta_2}} + e^{-i\boldsymbol{k\delta_3}}, \tag{2.11}$$

where:

$$\boldsymbol{\delta_1} = a\boldsymbol{x}, \qquad \boldsymbol{\delta_2} = \frac{a}{2}\left(-\boldsymbol{x} + \sqrt{3}\boldsymbol{y}\right) \quad and \quad \boldsymbol{\delta_2} = \frac{a}{2}\left(-\boldsymbol{x} - \sqrt{3}\boldsymbol{y}\right). \tag{2.12}$$

One can demonstrate [53, 54]:

$$| \gamma_{\boldsymbol{k}} | = \left| \sqrt{3 + 4\cos\left(\frac{k_x a}{2}\right)\cos\left(\frac{\sqrt{3}k_y a}{2}\right) + 2\cos\left(\sqrt{3}k_y a\right)} \right|. \tag{2.13}$$

Replacing this result into expression 2.10 $E_{\pm}(\boldsymbol{k})$ can be written as:

$$E_{\pm}(\boldsymbol{k}) = \pm V_{pp\pi} \left| \sqrt{3 + 4\cos\left(\frac{k_x a}{2}\right)\cos\left(\frac{\sqrt{3}k_y a}{2}\right) + 2\cos\left(\sqrt{3}k_y a\right)} \right|. \tag{2.14}$$

This result describes very well the dispersion relation of graphene close to the K points in the first Brillouin zone, i. e. the linearity of the bands close to the Fermi level, which is known as Dirac cone. In Fig. 2.4 one sees the conduction and valence bands of graphene obtained through a more sophisticated calculation, which takes into account a larger number of electronic transitions.

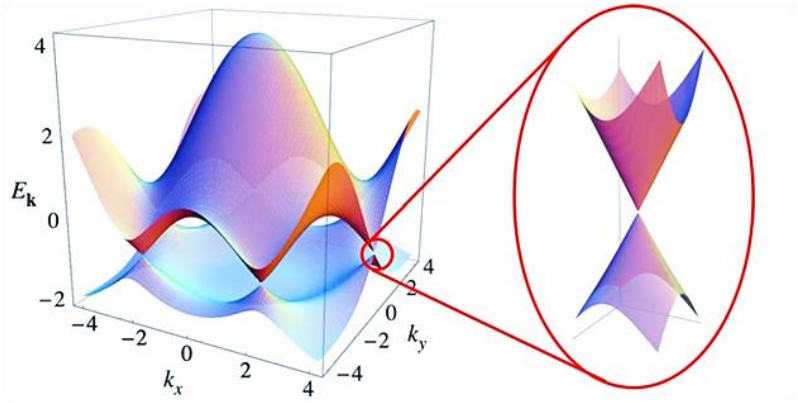

FIG. 2.4 – (a) Dispersion relation of graphene highlighting the Dirac cone. Figure taken from reference [3].

The Fermi energy of graphene is exactly at the junction of these two bands (known as π-bands), which allows one to identify it as a semimetal (zero band gap semiconductor). By zooming in at the region between these bands an approximately linear relation between energy and momentum (the Dirac cone) is observed. This is one of the properties that makes graphene so appealing compared to other materials that present parabolic dispersion relations and, consequently, a massive behavior of electrons

close to the Fermi level. Dirac cones are located at high symmetry points K and K' of reciprocal space. The vector K is [53, 54]:

$$\boldsymbol{K} = \frac{2\pi}{a}\left(\boldsymbol{k_x} + \frac{\boldsymbol{k_y}}{\sqrt{3}}\right). \tag{2.15}$$

A more complete band diagram, in which both π- and σ-bands, related to π- and σ-bonds, respectively, is shown in Fig. 2.5. Due to the position of the Fermi level in this system, i. e. between π- and π^*- bands, transition processes take place in the low energy region of the Dirac cone. This shows the validity of the approach used here, taking into account only π-bonds, to calculate energy bands of graphene close to the Fermi level.

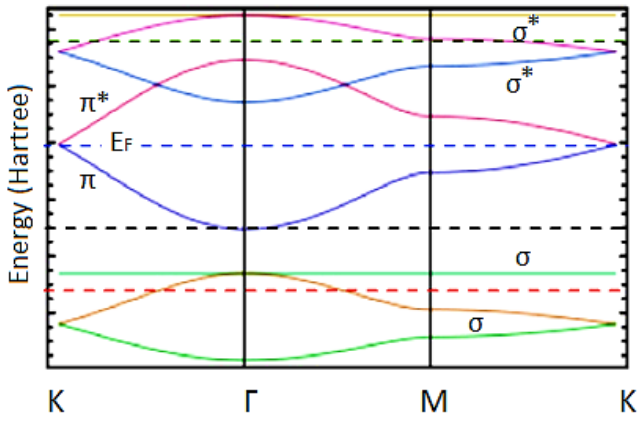

FIG. 2.5 – Band structure of graphene. Figure adapted from reference [54].

2.1.3 ELECTRONIC DENSITY OF STATES

Another equally important result to be discussed here is the density of states, N, particularly in the region of the Dirac cones. One can calculate the density of states per unit energy-area simply as [53, 54]:

$$N(E) = \frac{1}{A}\sum_{n} \delta(E - E_n). \tag{2.16}$$

Replacing energy eigenvalues E_n with momentum ones E_k:

$$N(E) = \frac{1}{A}\sum_{\boldsymbol{k}} \delta(E - E_{\boldsymbol{k}}). \tag{2.17}$$

As we focus our interest in the region where energy and momentum are approximately linear one can assume that $E_{\boldsymbol{k}} = v_f k$, in which $v_f = \frac{3}{2} V_{pp\pi} a$ or, equivalently, the Fermi velocity $v_f = dE/dk$. Summing electronic states in the first Brillouin zone and, thus considering the two Dirac cones at K and K' as well as the spin it is possible to write [53, 54]:

$$N(E) = 4 \int \frac{d^2k}{(2\pi)^2} \delta(E \pm v_f k). \tag{2.18}$$

Limiting the region of interest to Dirac cones by introducing limits in the integral and rearranging its terms 2.18 becomes [53, 54]:

$$N(E) = \frac{2}{\pi v_f} \int_0^{\Lambda} k\delta\left(\frac{E}{v_f} \pm k\right) dk. \tag{2.19}$$

$$N(E) = \frac{2 \mid E \mid}{\pi {v_f}^2}. \tag{2.20}$$

Thus, one verifies that the density of states like the dispersion relation also presents a linear behavior in the low energy range (in the approach used here only the energy interval close to the Fermi level was considered). Fig. 2.6 depicts a plot of the density of states as a function of energy where one clearly sees the linearity of this relationship especially in the right panel of this figure (a zoom close to the Fermi level). Moreover, one also observes regions where the density of states diverges (the van Hove singularities), which are related to regions where the slope of the bands is zero (high symmetry M points) [53, 54].

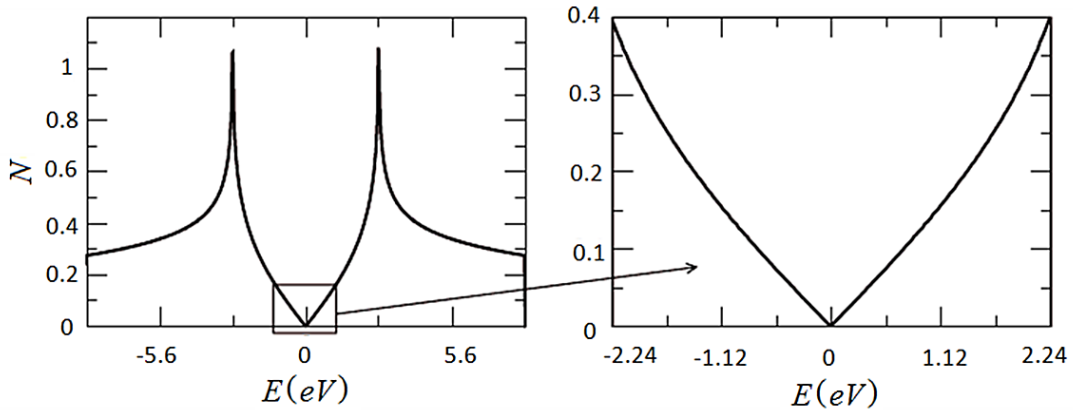

FIG. 2.6 – Density of states (N) as an energy function of a perfect graphene sheet highlighting the linearity of this relationship in a low energy range. Figure adapted from reference [3].

2.2 TOPOLOGICAL INSULATORS

Topological insulators are a new state of quantum matter that present an insulating behavior in the bulk but conducting channels at the surface. This class of materials was first theoretically predicted in 2005/2006 and just shortly afterwards experimentally realized. D. J. Thouless, F. D. M. Haldane and J. M. Kosterlitz were awarded with the Nobel Prize in Physics for their theoretical contributions to topological phases of matter, which permitted important advances in this field [55]. In these materials high spin-orbit coupling gives rise to a band-inversion mechanism that leads to spin-polarized surface states. In the particular case of Bi_2Se_3 and Bi_2Te_3 these surface states have also a linear dispersion close to the Γ point and are protected by time-reversal symmetry [56, 57]. Remarkable properties of the mentioned states may enable the application of topological insulators in spintronic devices. Here we present an overview on the subject introducing a number of concepts and revisiting important effects. The starting point is the mathematical concepts of topology and how they relate to band theory. Next, we introduce Chern insulators through a discussion of the quantum Hall effect and finally, $\mathbb{Z}_2$ topological insulators are presented.

2.2.1 TOPOLOGY AND BAND THEORY

The mathematical concept of topological invariance was introduced to classify different objects according to their fundamental geometrical properties, discarding small details. In this context, the surface of a sphere is topologically equivalent to the surface of a bowl, since they can be smoothly deformed into one another. On the contrary, the surface of a sphere cannot be converted into a doughnut unless a hole is created, which makes them topologically distinct. In geometry this classification is related to the genus g, which is the number of holes of a given surface and therefore assumes only integer values. Thus, objects with different genuses, like a sphere and a doughnut, are said to be topologically distinct, since smooth deformations cannot create holes at the surface [58]. The theorem of Gauss-Bonnet defines the topological invariant called Euler characteristic [58, 59], χ, which is related to the geometrical integral of the Gaussian curvature, K, over the surface S, as [58]:

$$\int_S K dA = \chi = 2 - 2g. \tag{2.21}$$

As one sees, this integral groups objects with common geometrical properties to the same topological class despite differences in their shape. In addition, the right-hand side of this expression is quantized and arbitrary changes in K that do not create holes also do not modify its topology [58, 60]. The concept of topology can be connected to band theory and, thus, be used to characterize different phases of matter. A number of physical quantities such as the Hall conductance is not affected by small changes, which may include defects or thermal fluctuations in the investigated system. Thus, many topologically quantities can be expressed in terms of invariant integrals [61, 62]. In this context, the Gauss-Bonnet theorem was generalized by Chern [28, 63, 64], being used to define its invariant, which groups different band structures. In solid state physics, for instance, insulators have an energy gap that separates ground and excited states. Here, the topological equivalence between two insulators is defined if one can be converted into another by slow changes in the Hamiltonian, in such a way that the energy gap remains finite during this adiabatic process [58, 60, 65]. If such path does not exist the two insulators are not topologically equivalent and a connection between them involves a quantum phase transition, which closes the energy gap [58]. Thus, whenever two topologically distinct materials, i. e. with different Chern invariants, are in contact gapless states will arise at the interface. This is a consequence of closing the energy gap necessary to change the topological invariant when one goes from one system to the other [28]. Other concepts of topology like topological order parameter, which may lead to quantization of physical properties, and topological field theory can also be introduced to describe topological states [64].

There are gapped systems that belong to different topological classes regarding conventional insulators and vacuum (which according to Dirac's relativistic quantum theory also has an energy gap) and, therefore, present remarkable properties [28]. Before discussing so-called topological insulators, it is very useful, for a better understanding of ideas and concepts introduced here, to analyze the quantum Hall state. This phenomenon is described in the next section and can be comprehended in terms of topology.

2.2.2 QUANTUM HALL EFFECT

The integer quantum Hall effect is an important example of a gapped state that is electronically distinct from conventional insulators. This phenomenon was first observed by von Klitzing et al. in the 80s when a 2D gas of electrons in a semiconductor was subjected to low temperatures and a strong magnetic field [66]. Under such conditions it was verified that the current, which flows only in one direction along the edge of the 2D insulating bulk sample, also gives rise to a quantized Hall effect [28].

In order to understand this in comparison with a conventional insulator it is useful to picture a scenario where we consider both a schematic view of the materials and also of their band structure. Kohn et al. [67] proposed the theory of an insulating state in which the electrons are considered to be occupying localized orbitals (moving bound to their atoms), insensitive to effects at the edges of the sample (see Fig. 2.7a) [67, 68]. The band structure of these materials consists of an occupied valence band separated by an energy gap to the empty conduction band as depicted in Fig. 2.7b. In the quantum Hall state Lorentz forces lead the electrons to move in circular orbits with quantized energies known as Landau levels. The energy can be written as:

$$E_n = \left(n + \frac{1}{2}\right)\hbar\omega_c, \tag{2.22}$$

where n is an integer number (in the case of integer quantum Hall state), $\hbar$ is the reduced Planck constant and $\omega_c = eB/m$ is the cyclotron frequency, e the electron charge, B the magnetic field and m is the electron mass. In this regime electrons move in cyclotron orbits in the bulk, but skipping orbits along the edges (see Fig. 2.7c). This conduction mechanism only at the edges of the material is a consequence of blocking the natural trajectory of electrons due to the vacuum barrier [68]. In addition, the Landau levels can be viewed as a band structure. Considering that a number of Landau levels are filled and the remaining ones are empty, this state can be seen at first glance as an insulator, with an energy gap separating conduction and valence bands [28]. However, differently from a conventional insulator, cyclotron orbits respond to an electric field, giving rise to a Hall conductance [28]. Thus, this state has a bulk energy gap, but also edge states at the boundary as schematically illustrated in Fig. 2.7d.

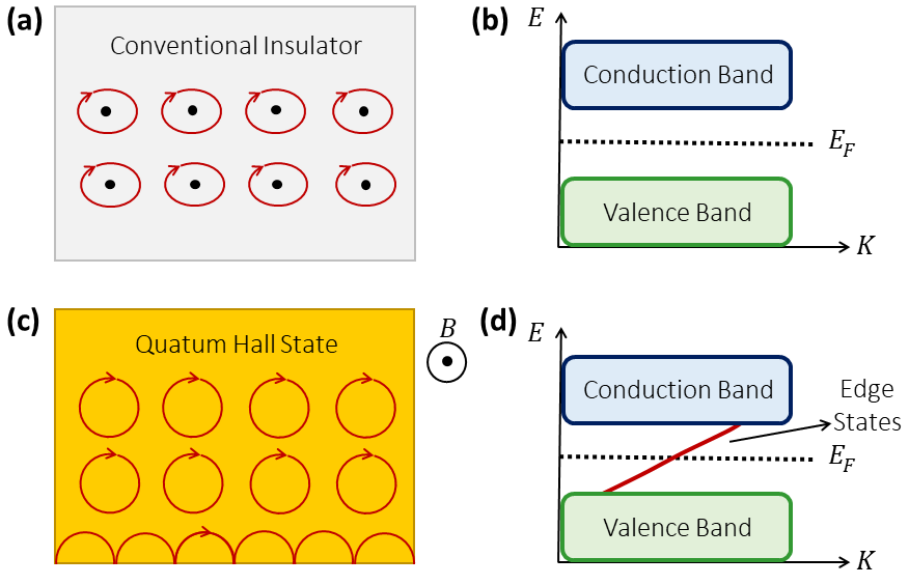

FIG. 2.7 – (a) Schematic representation of a conventional insulator with electrons occupying atomic orbitals. (b) Typical band structure of an insulator with a band gap separating the conduction and valence bands. The Fermi level is indicated by E_F. (c) Schematic representation of a quantum Hall state with the electrons moving in cyclotron orbits. This state is characterized by edge states (see text). The direction of the magnetic field B is indicated in the panel. (d) Band structure of a quantum Hall state. Here an edge state connects the conduction and valence bulk bands.

As previously stated, one of the findings of the experiment performed by von Klitzing et al. [66] was the quantization of the Hall conductance as a function of the magnetic field. One can write the Hall conductance, σ, as:

$$\sigma = \frac{ne^2}{h}, \tag{2.23}$$

where h is the Planck constant, e is the electron charge and n is an integer. In Fig. 2.8 one sees the plot of the Hall resistance, the reciprocal of the Hall conductance, versus the magnetic field applied perpendicularly to the 2D electron gas in a semiconductor at low temperature. This measurement demonstrates the quantization of the Hall conductance as highlighted by its stair-like behavior with well-defined plateaus [28, 63]. Interestingly, the Hall conductance could be measured with extremely high precision independently of the geometry and quality of the sample [69]. This set of results that include the edge states together with the quantization of the Hall conductance is closely related to the concepts of topology presented in section 2.2.1.

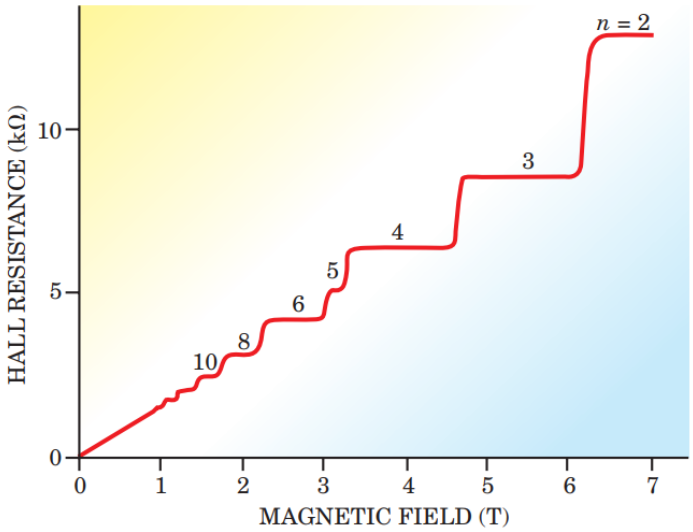

FIG. 2.8 – Hall resistance versus magnetic field measured for a quantum Hall state. The stair-like behavior of the curve indicates the quantization of the Hall conductance. Figure taken from references [63, 70].

In the topological framework the existence of edge states arises simply as a result of closing the energy gap at the interface between materials that do not have the same topology, in this case the quantum Hall state and the vacuum. As depicted in Fig. 2.9a for the quantum Hall state, the Chern invariant is 1, but for the conventional insulators it is 0. As explained before, it is not possible to change the topological invariant without creating a gapless state at the interface that separates the two systems [28]. Therefore, the quantum Hall state (or the Chern insulators) will present an edge state connecting its conduction and valence bulk bands (see Fig. 2.9b). In addition, Thouless et al. [61] demonstrated that n in expression 2.23 is equivalent to the Chern invariant. As a consequence, small changes in the Hamiltonian that describes the sample like defects or its own geometry do not affect this value [61, 71], which explain the robust quantization of the Hall conductance.

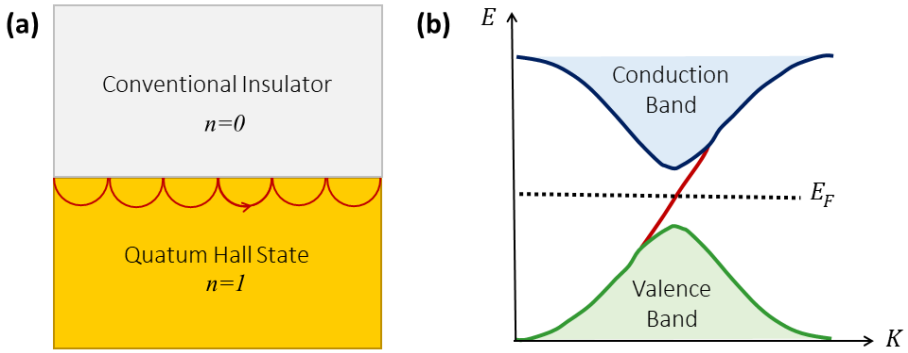

FIG. 2.9 – (a) Scheme showing the edge state that appears at the interface of a quantum Hall state ($n = 1$) and a conventional insulator ($n = 0$) materials that belong to different topological classes (see text). (b) Typical band structure of a quantum Hall state with edge states (red) crossing the insulating gap that separates the conduction and valence bulk bands.

2.2.3 QUANTUM SPIN HALL EFFECT

The extreme conditions in which the quantum Hall state was experimentally observed, i. e. very low temperatures and high magnetic fields, represent an important limiting factor regarding practical applications. This motivated the search for a broader class of topological states that would not require such conditions. In 2005 and 2006 different groups theoretically proposed the quantum spin Hall state, in which the spin-orbit coupling would act similarly to the magnetic field in the quantum Hall state [72-74]. The experimental observation of such state came soon in 2007 with the study of HgTe quantum wells [29, 30].

In the quantum spin Hall state insulators have spin-polarized conducting channels at the edges, which arise due to a high spin-orbit coupling. Differently from the previous case, however, here the time-reversal symmetry is not broken [60, 75]. This requires the definition of a new topological invariant $\mathbb{Z}_2$, which characterizes this new class of topological states.

In the quantum Hall effect the electrons of the chiral edge state propagate only along one direction. As schematically illustrated in Fig. 2.10a such conditions make these channels extremely robust against the presence of impurities, circumventing them without backscattering [75, 76]. The quantum spin Hall state can be pedagogically

understood as two helical edge states (meaning that the spin is directly related to the direction of the movement of the electrons), each of which have opposite spins, with the electrons travelling in opposite directions (see Fig. 2.10b). Also, for this state there is no backscattering by nonmagnetic impurities. Even though forward and backward conducting channels are available in this case, quantum mechanics imposes a destructive interference between the electronic paths of the two edge states [76].

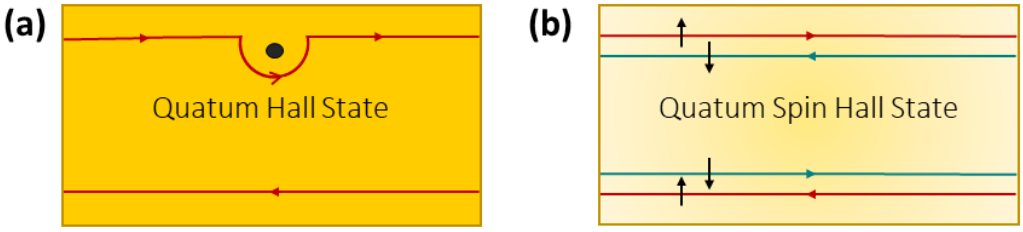

FIG. 2.10 – (a) In the quantum Hall state chiral edge states propagate along one direction defined by the applied magnetic field. These conducting channels are robust against impurities and backscattering is forbidden. (b) In the quantum spin Hall state two helical edge states with opposite spins travel in opposite directions.

As previously stated, the quantum spin Hall effect was experimentally confirmed in HgTe quantum wells by König et al. [29, 30]. In this work HgTe layers with different thicknesses were synthesized by molecular beam epitaxy in between CdTe layers (see Fig. 2.11). As the thickness of the quantum well increases the spin-orbit coupling, which is more pronounced in heavy elements, also increases. This effect changes the band structure of the quantum well inverting its bands. For this particular case the valence band, formed from electrons in p orbitals, is pushed down and, consequently, inverted, for a certain critical thickness, with the conduction band, formed from electrons in s orbitals [76]. In this regime edge states with opposite spins emerge. In addition, time-reversal symmetry imposes the crossing of these bands as depicted in Fig. 2.11.

The edge states of HgTe quantum wells have a linear dispersion relation close to the Γ point, where the two states cross each other (see Fig. 2.11b, lower panel). The fact that this dispersion relation is identical to the one obtained from the Dirac equation for a massless relativistic fermion in quantum field theory allows one to use it to describe the edge states of quantum spin Hall systems [76].

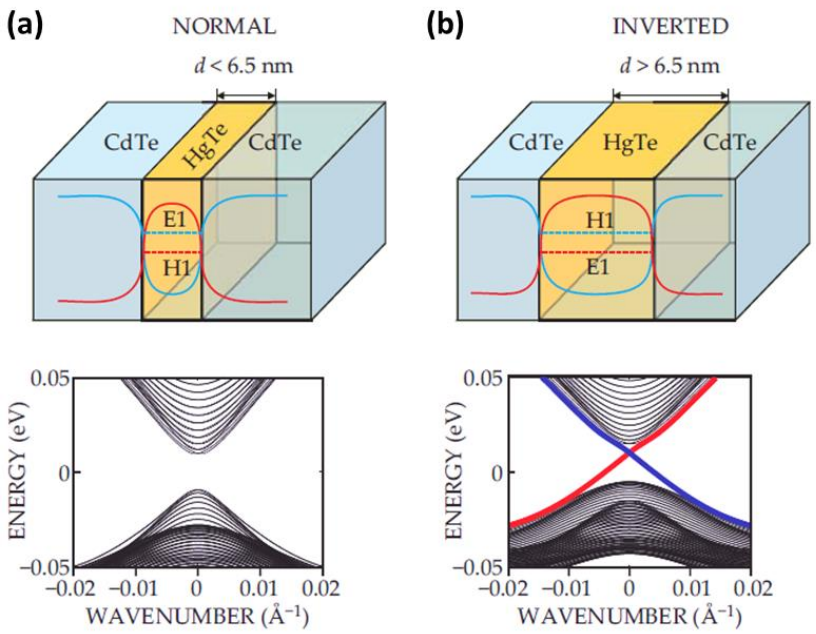

FIG. 2.11 – (a, Upper panel) Schematics of a HgTe quantum well with a thickness below a critical value. The electrons in the conduction band (blue curve) experience a potential-energy well as depicted in this panel. The holes of the valence band (red curve) face a potential barrier. This traps the electrons and holes laterally. (a, Lower panel) Under this condition a band gap separates the conduction and valence bulk bands. (b, Upper panel) Schematics of the HgTe quantum well with a thickness greater than a critical value. Under this condition the lowest conduction band and the highest valence band are inverted due to the increase in spin-orbit coupling. (b, Lower panel) Edge states, shown in red and blue colors, now cross the insulating bulk gap. Figure taken from reference [76].

2.2.4 THREE-DIMENSIONAL TOPOLOGICAL INSULATORS

The Hamiltonian that describes quantum spin Hall states could be generalized to three dimensions [77-79] and shortly after the experimental evidence of the three-dimensional (3D) topological insulators was found in $Bi_{1-x}Sb_x$, Bi_2Se_3 and Bi_2Te_3 [80-82]. In analogy to the previous case, the surface state of a 3D topological insulator is given now by one single Dirac cone per Brillouin zone. Similarly to graphene, the electrons behave as massless Dirac fermions. In Bi_2Se_3 and similar compounds the atoms have an ABC stacking and present a layered structure in which Se-Bi-Se-Bi-Se atoms are grouped together forming a quintuple-layer. These quintuple-layers are connected to each other by van der Waals interactions, permitting their exfoliation (see Fig. 2.12a). The chemical bonds within individual layers, on the other hand, have a covalent character [83]. Angle-resolved photoemission spectroscopy measurements showed a linear dispersion relation

at the Γ point with circular surface energy contours for the Dirac cone (not shown) as theoretically predicted [35, 84, 85]. However, it was verified that the bulk of this system was not purely insulating, which was attributed to the presence of Se vacancies in the system that n-doped the material (see Fig. 2.12b). Hsieh et al. [86] have overcome this issue by doping the sample with Ca and, thus adjusted the Fermi level in between the conduction and valence bulk bands. Also, experiments revealed that the spin of the electrons is always perpendicular to the linear momentum in this case.

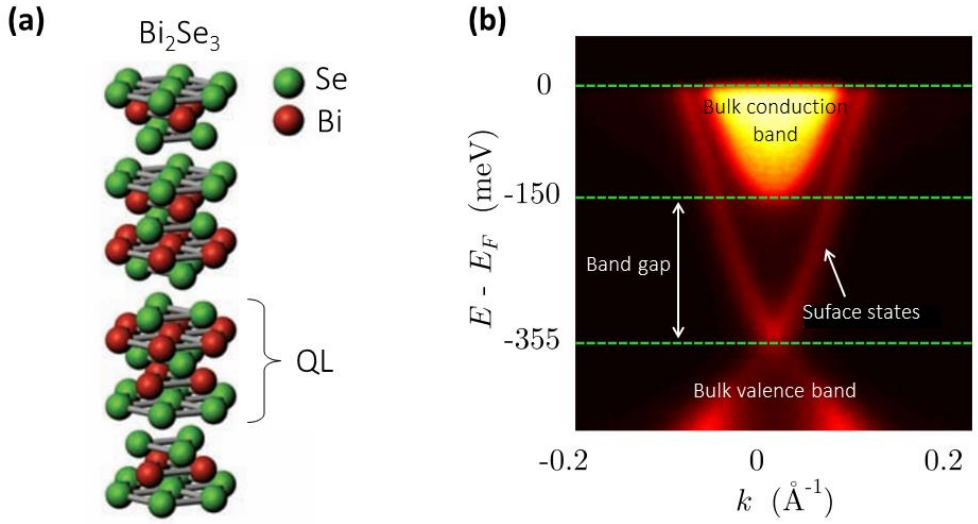

FIG. 2.12 – (a) Crystal structure of the 3D topological insulator Bi_2Se_3. This material is composed of layers of Se-Bi-Se-Bi-Se, forming quintuple-layers (QL), stacked along the (111) direction. (b) ARPES measurements of the band dispersion of Bi_2Se_3. Figure adapted from references [35] and [36].

In Bi_2Te_3 similar features were observed and also in this system the Fermi level crosses the conduction bulk band, but in this case, this is caused by Te vacancies. This is seen in Fig. 2.13a, which shows its dispersion relation along the K-Γ-K and M-Γ-M paths in the first Brillouin zone. However, differently from the previous case, Fermi surfaces are not circular, but rather warped and present a snowflake shape as depicted in Fig. 2.13b. Maps of the Fermi surface using different photon energies confirm the surface state character of the Dirac cone, since its shape remains unaltered, differently from what one observes for inner conduction bulk bands [36]. Another important feature of the band structure of Bi_2Te_3 is that its bulk conduction band is partially nested inside the Dirac

cone. Therefore, sole electronic conduction at the surface only occurs in a limited energy range. Bi_2Te_3 preserves all properties of a true topological insulator such as Bi_2Se_3, in the energy range -355 meV to -150 meV.

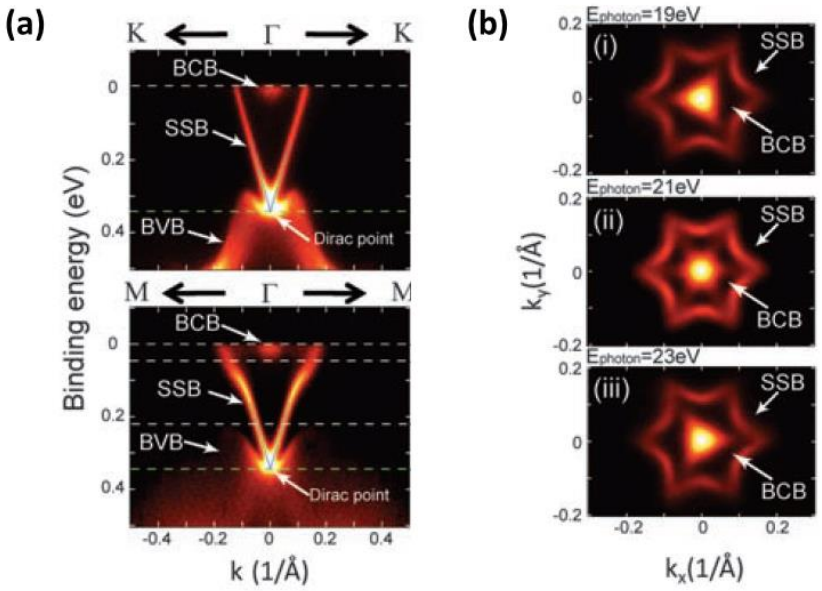

FIG. 2.13 – (a) ARPES measurements of the band dispersions of Bi_2Te_3. (b) Fermi surface maps for different photon energies (indicated in each panel). Figure taken from reference [36].

In the 3D case, differently from the previous one, there are four $\mathbb{Z}_2$ invariants: ν_0; (ν_1, ν_2, ν_3). This set of invariants can be used to classify 3D topological insulators into two different classes, namely, strong or weak, depending on the nature of their surface states. This nomenclature is directly related to the degree of robustness of the system to different types of perturbations [87, 88].

2.3 TRANSITION METAL DICHALCOGENIDES

Transition metal dichalcogenides (TMDCs) also form an important class of materials. They present the formula MX_2, in which M is a transition metal and X is a chalcogen [37-39]. Depending on the particular combination of atoms an electronic structure that ranges from an insulating to a metallic behavior can be obtained [37-39, 89]. Important examples are MoS_2 and WS_2, which are semiconductors, differently from TaS_2 which has a metallic behavior and will be the focus of this work (chapter VI). These

materials had their structure first determined by Dickinson et al. [90] in 1923 and already in the 1960s were produced as ultrathin films and later on as single layers [91]. Over the years, many studies focusing on the properties of layered TMDCs made them possible candidates to be used in nanoelectronics and nanophotonics [40, 92]. Therefore, it is relevant and useful for device applications to verify and understand how the properties of transition metal dichalcogenides are affected as the thickness of these layered materials change and how they are influenced by the underlying substrate. Here, we present the basics of TMDCs, including discussions about their atomic structure and some of their electronic properties.

2.3.1 ATOMIC STRUCTURE

As previously mentioned, TMDCs have the formula MX_2 with one transition metal layer sandwiched between two chalcogen ones in hexagonal planes as depicted in Fig. 2.14. M and X are connected through covalent bonds and the bulk form of these layered materials is established by stacking them. These layers are weakly bonded to each other by van der Waals interactions. In addition, these materials may present different polytypes, having distinct atomic orientations and stacking sequences. The metallic atom in TMDCs can present trigonal prismatic or octahedral coordination (among others) which, in fact, characterizes the two most common structural phases of this class of materials, namely 2H (Fig. 2.14a) and 1T (Fig. 2.14b), respectively. In this nomenclature the letters refer to the symmetry in the crystal, i. e. hexagonal or tetragonal for the 2H and 1T phases, respectively, while the number refers to the number of X-M-X units or layers in a repeating unit (see Fig. 2.14, upper panel) [37-39, 47].

In addition, the 2H phase presents an ABA stacking with chalcogen atoms of different layers always on top of each other (see Fig. 2.14a, middle panel), which gives it a honeycomb-like structure similar to graphene (Fig. 2.14a, lower panel). Differently, the 1T phase presents an ABC stacking as indicated in the middle panel of Fig. 2.14b [37-39, 47]. Its top-view also resembles a honeycomb structure with an atom in the middle of each hexagon (Fig. 2.14b, lower panel). A schematic view of these two structures is shown in Fig. 2.14. The stability of these phases varies for different TMDCs, but usually, even

non-favorable configurations can exist as metastable phases under specific conditions [37-39, 47].

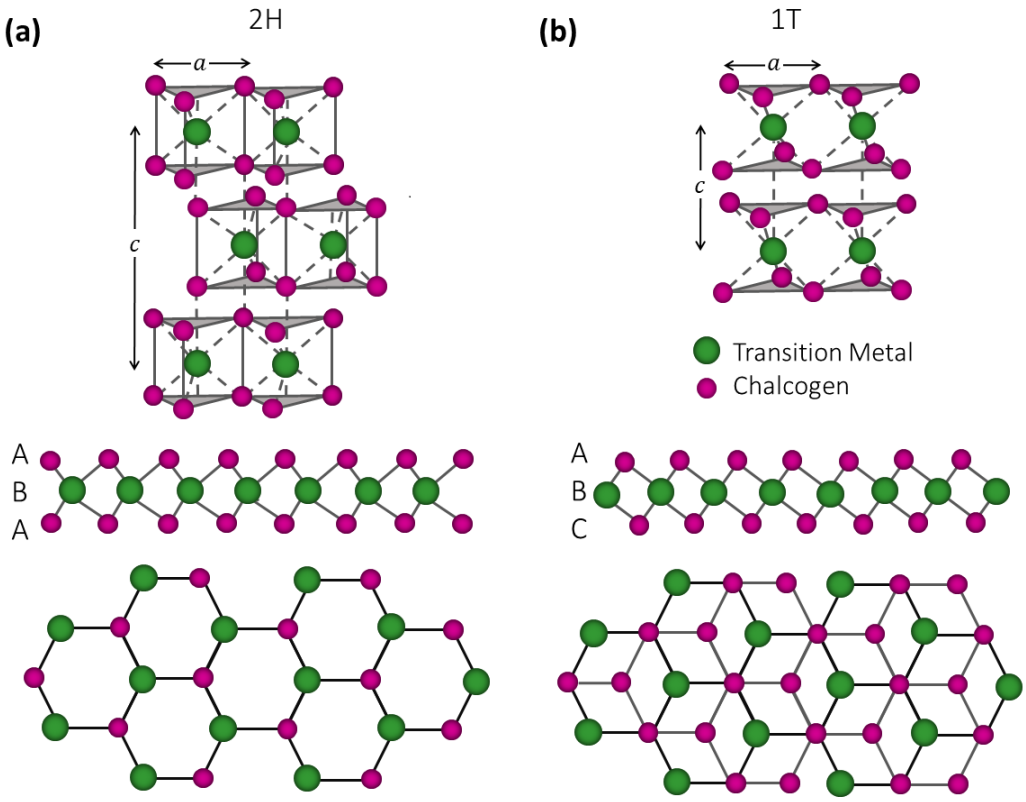

FIG. 2.14 – Schematic view of the structure of TMDCs in the (a) 2H and (b) 1T phases. (Upper panel) Scheme representing the trigonal prismatic and octahedral coordination of atoms in the 2H and 1T polytypes (left and right panels, respectively). The lattice constant (a) varies from 0.31 nm to 0.37 nm for different TMDCs. The parameter c indicates the number of layers in a repeating unit. (Middle panel) Side view of a single TMDC layer in H and T phases (left and right panels, respectively). (Lower panel) Top view of these two TMDC structures.

2.3.2 ELECTRONIC PROPERTIES

The electronic properties of TMDCs depend on their atomic composition as well as the atomic arrangement [37-39], meaning their polytype, discussed in the previous section. A simple example that illustrates this is 2H-MoS_2 and 2H-TaS_2. While MoS_2 is a semiconductor, TaS_2 exhibits a metallic behavior. Depending on the atomic coordination of the materials the band structures will differ. Particularly important are the nonbonding d-bands located between the bonding and the antibonding bands. For a trigonal prismatic coordination, the d-orbitals split into three groups, while for an octahedral coordination

they degenerate into two bands [38, 47]. 2H-MoS_2 and 2H-TaS_2 have exactly the same atomic coordination. The difference however, lies on the metallic atom, Ta and Mo, transition metals from groups V and VI of the period table, respectively. What explains the distinct electronic character is the filling of d-bands. In the case of MoS_2 the valence band is completely full while for TaS_2 it is only partially occupied (see Fig. 2.15) [38, 47]. The role of the chalcogen is related to broadening of these bands [38]. Moreover, an increase of the band gap is observed as its atomic number decreases [38].

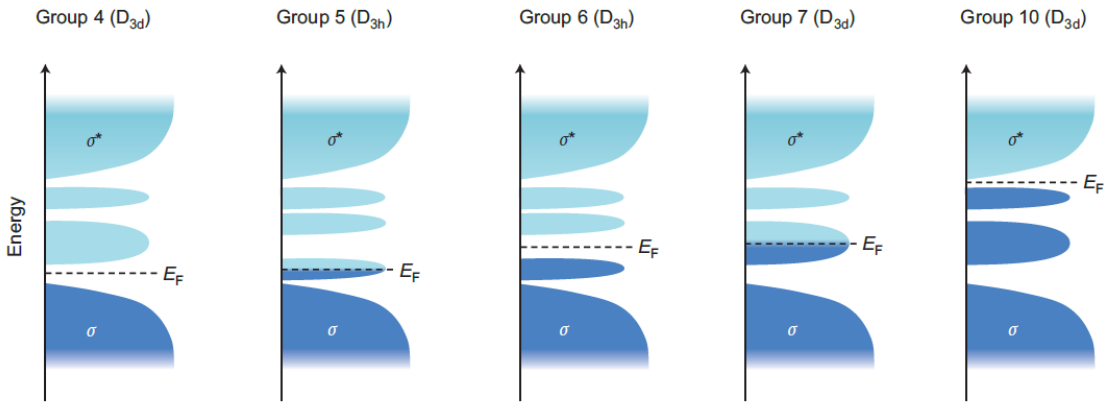

FIG. 2.15 – d-Orbital filling and electronic character in groups IV, V, VI, VII and X TMDCs. Figure taken from reference [38].

The phase also plays an important role, making the same system host completely different properties. In the case of MoS_2, modifications from semiconducting to metallic behavior can take place, as the structure changes from 2H to 1T/1T'. This remarkable change in properties has been strategically used to improve the performance of field-effect transistors creating low-resistance contacts.

Furthermore, the dimensionality is also an important factor in the electronic structure of layered materials, since a number of properties is thickness-dependent. The classic example is graphene, which presents unique properties and band structure, including a Dirac cone at the K point of the Brillouin zone, that is absent in graphite [1-4]. The same is valid for TMDCs. The effect of the number of layers on the electronic properties can be clearly seen in the case of MoS_2. In Fig. 2.16 one observes the band structure of 2H-MoS_2 obtained via first-principle calculations [38, 40]. In this figure it is

possible to see the changes in the electronic bands as the number of layers is reduced to a monolayer. One observes that the conduction bands located at the K point remain unchanged as the thickness of MoS_2 decreases, differently from the bands around the Γ point. This is because different bands can be more or less affected by interlayer interactions. Thus, as the thickness decreases the indirect band gap of 0.88 eV observed in the bulk crystal evolves into a direct band gap of 1.71 eV [38, 40]. These modifications in the electronic properties of the material as its thickness changes are explained by quantum confinement effects, which alter the hybridization of the atoms in the layer. Moreover, the electronic distribution is also affected by atomic configurations [37-39, 47].

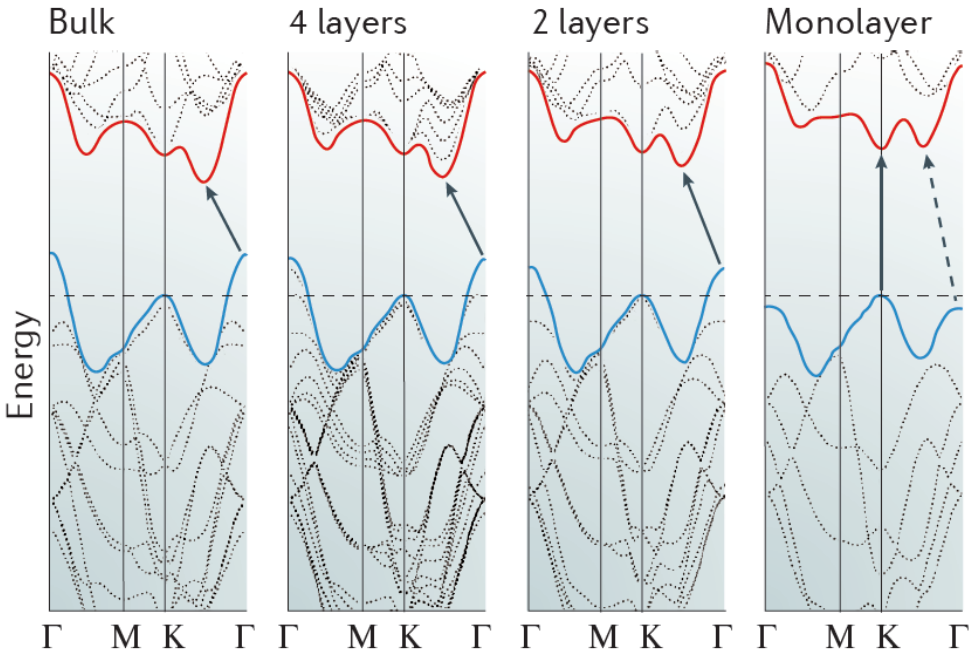

FIG. 2.16 – Evolution of the band structure of 2H-MoS_2 as its thickness changes from bulk form to monolayer. Figure taken from reference [38].

Differently from MoS_2, TaS_2 does not exhibit a semiconducting behavior, but rather a metallic one, as previously stated. Despite the absence of an electronic gap, this material is interesting for distinct reasons. TaS_2 host properties of superconductivity, charge density waves and Mott transitions [44-46, 94, 95] among others in the T phase, but neither charge density waves nor superconductivity was observed in the H phase.

For 2H-TaS_2 the parameters a and c are respectively: 0.3342 nm and 1.254 nm. In the 1T-TaS_2 phase $a = 0.338$ nm and $c = 0.619$ nm [96]. In Fig. 2.17 density functional theory calculations for a free standing single TaS_2 layer are presented [46]. In the left panel of this figure the band structure along the M-Γ-K path in the first Brillouin of 1H-TaS_2 is shown, while in the right panel the band structure of 1T-TaS_2 can be seen. In both cases the metallic character of TaS_2 can be verified since a couple of bands cross the Fermi level.

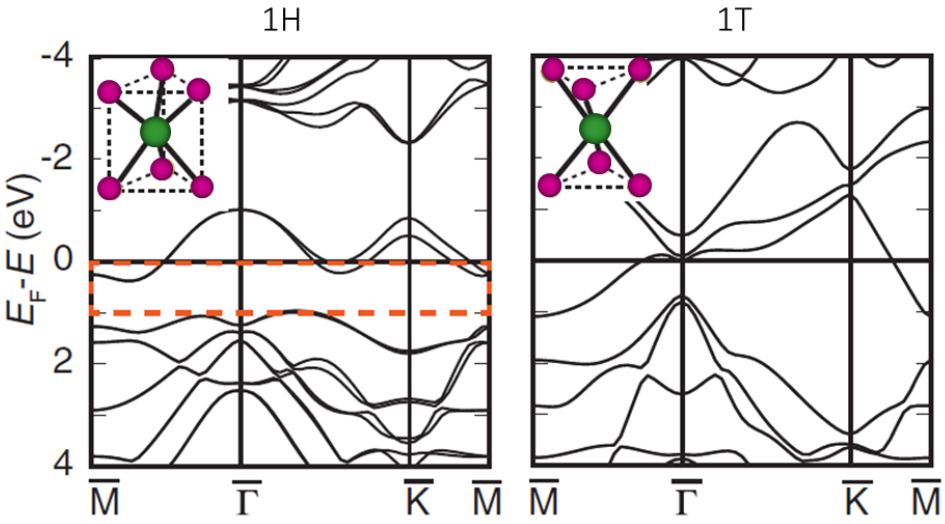

FIG. 2.17 – Band structure of (left panel) single layer 1H-TaS_2 and (right panel) 1T-TaS_2. Figure adapted from reference [46].

III.

EXPERIMENTAL TECHNIQUES

In this work we have used different experimental techniques among which are scanning tunneling microscopy/spectroscopy and angle-resolved photoemission spectroscopy. These experimental tools proved to be essential for the investigation of materials studied in this thesis. In the chapter in question we explain the physical concepts related to these techniques. This knowledge is fundamental for a deeper comprehension of the experimental results that will be shown afterwards.

3.1 SCANNING TUNNELING MICROSCOPY AND SPECTROSCOPY

Scanning tunneling microscopy and spectroscopy (STM/STS) are interesting techniques to investigate not only nanostructures of 2D materials like graphene, but also the surface of other materials such as topological insulators, semiconductors and transition metal dichalcogenides. The scanning tunneling microscope was invented in 1981 by H. Rohrer and G. Binnig [97]. This technique is based on the quantum phenomenon of tunneling and enables imaging of atomic and molecular structures by varying the tunneling current between an atomically thin conducting tip and the investigated sample. Together with microscopy, tunneling spectroscopy is used to obtain information about the local density of states of the sample as a function of the electron energy.

3.1.1 THE TUNNELING CONCEPT

According to the classical mechanics theory, an electron of mass m and energy E subjected to a potential $U(z)$ can be described by the following equation [98, 99]:

$$\frac{p^2}{2m} + U(z) = E. \tag{3.1}$$

Under such conditions the momentum of the electron will be $p = \sqrt{2m(E-U)}$, implying that its motion is limited to regions where the value of its energy E exceeds the value of its potential energy, U.

In quantum mechanics, on the other hand, its motion is described by Schrödinger's equation, whose time independent form is:

$$-\frac{\hbar^2}{2m}\frac{d^2}{dz^2}\psi(z) + U(z)\psi(z) = E\psi(z). \tag{3.2}$$

Considering the relation between $U(z)$ and E specified in Fig. 3.1:

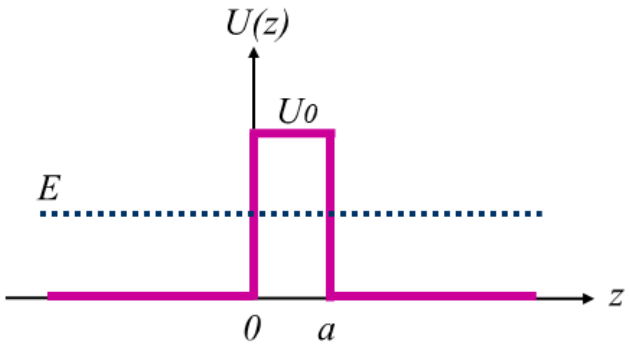

FIG. 3.1 – Rectangular potential barrier $\boldsymbol{U(z)}$.

The solution of the equation 3.2 for each region will be:

$$\psi(z) = A_1 e^{ikz} + B_1 e^{-ikz}, \qquad z \leq 0, \tag{3.3}$$

$$\psi(z) = Ce^{\kappa z} + De^{-\kappa z}, \qquad 0 \leq z \leq a, \tag{3.4}$$

$$\psi(z) = A_2 e^{ikz} + B_2 e^{-ikz}, \qquad z \geq a, \tag{3.5}$$

where $k = \frac{\sqrt{2mE}}{\hbar}$ and $\kappa = \frac{\sqrt{2m(Uo-E)}}{\hbar}$. For $z \leq 0$ and $z \geq a$ the solutions described above correspond to an electron moving with $p = \hbar k$ or simply $v = p/m$ and it is similar to the classical case, previously discussed. On the contrary, the great difference between classical and quantum theories lies on the region $0 \leq z \leq a$. Since the electron wave function has a finite value in the region of the potential barrier, there is a certain probability that it penetrates in the classically forbidden region or even passes through the barrier, a quantum phenomenon known as tunneling (see Fig. 3.2).

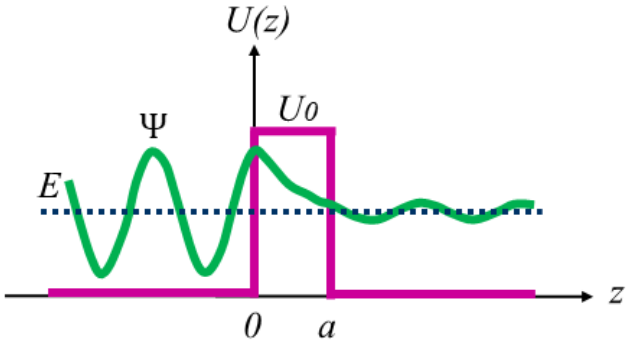

FIG. 3.2 – Quantum tunneling representation.

The constants of the wave function shown in equations 3.3 to 3.5 can be determined by the conditions of continuity of $\psi(z)$ and $d\psi(z)/dz$ for $z = 0$ and $z = a$. These constants give us information about the reflection and transmission coefficients, R and T, respectively. In the matricial form the relation among these constants for $z = 0$ is [98]:

$$\begin{bmatrix} 1 & 1 \\ ik & -ik \end{bmatrix} \begin{bmatrix} A_1 \\ B_1 \end{bmatrix} = \begin{bmatrix} 1 & 1 \\ \kappa & -\kappa \end{bmatrix} \begin{bmatrix} C \\ D \end{bmatrix}. \tag{3.6}$$

Similarly, for $z = a$:

$$\begin{bmatrix} e^{\kappa a} & e^{-\kappa a} \\ \kappa e^{\kappa a} & \kappa e^{-\kappa a} \end{bmatrix} \begin{bmatrix} C \\ D \end{bmatrix} = \begin{bmatrix} e^{ika} & e^{-ika} \\ ike^{ika} & ike^{-ika} \end{bmatrix} \begin{bmatrix} A_2 \\ B_2 \end{bmatrix}. \tag{3.7}$$

The coefficients R and T can be obtained through the transference matrix, $[P]$, which is defined as [98]:

$$\begin{bmatrix} A_1 \\ B_1 \end{bmatrix} = [P] \begin{bmatrix} A_2 \\ B_2 \end{bmatrix}, \tag{3.8}$$

Thus, the reflection and transmission coefficients are:

$$R = \left|\frac{B_1}{A_1}\right|^2 = \left|\frac{P_{21}}{P_{11}}\right|^2, \tag{3.9}$$

$$T = \left|\frac{A_2}{A_1}\right|^2 = \left|\frac{1}{P_{11}}\right|^2, \tag{3.10}$$

respectively, satisfying the condition $R + T = 1$. Explicitly, T can be written as [98]:

$$T = \left\{1 + \frac{{U_0}^2[\mathrm{senh}(\kappa a)]^2}{4E(U_0 - E)}\right\}^{-1}. \tag{3.11}$$

If $\kappa a \gg 1$, then T can be simplified as:

$$T = \left[\frac{4E(U_0 - E)}{{U_0}^2}\right] e^{-2\kappa a}. \tag{3.12}$$

Analyzing this expression, one sees that the transmission coefficient depends exponentially on the width of the potential barrier, a. This was experimentally observed by Binnig et al. [100] and it is what makes possible imaging surfaces of different sorts of materials, with high-resolution.

3.1.2 SCANNING TUNNELING MICROSCOPE

The invention of the scanning tunneling microscope by H. Rohrer and G. Binnig in 1981, not only rewarded them with the Nobel Prize in Physics in 1986, but also opened up a new field for research on condensed matter. It allowed obtaining nanometric images and, consequently, the visualization of atomic and molecular structures [97, 101]. In Fig. 3.3, one can observe a schematic view of a scanning tunneling microscope:

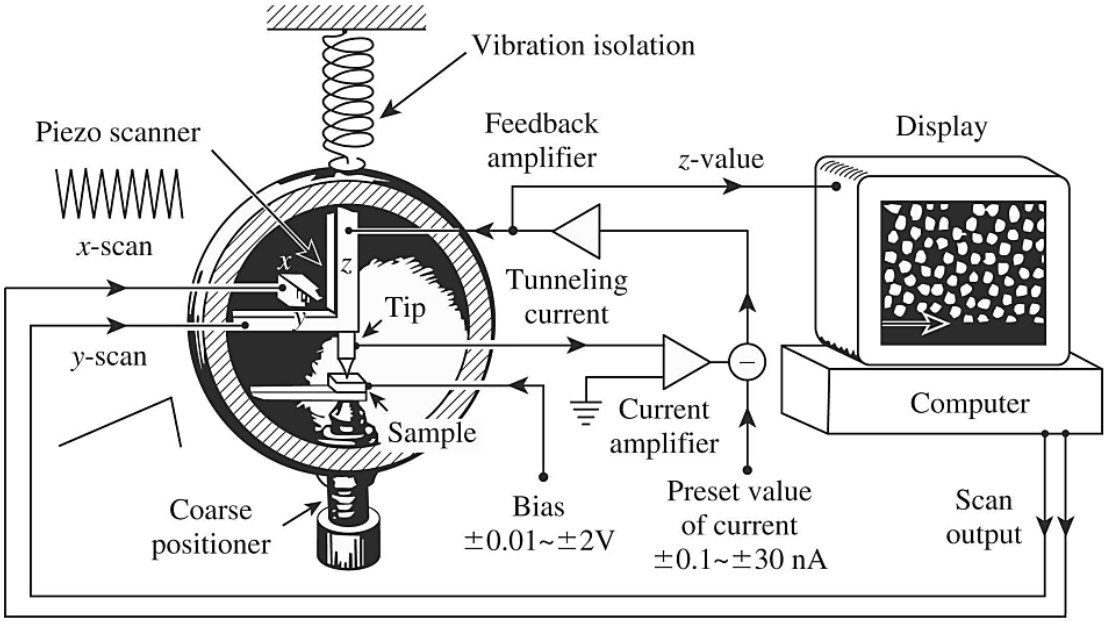

FIG. 3.3 – Schematic view of a scanning tunneling microscope. Figure taken from reference [99].

The scanning tunneling microscope basically works as follows: an atomically thin conducting tip, usually made of W or Pt/Ir is connected to motors with nanometric resolution in the x, y and z directions. These motors are made of piezoelectric materials, which can contract or expand depending on the application of positive or negative bias voltages. The cited property makes this system able to scan the surface of the sample along x and y directions, and also vary its z position. Once the tip and the sample are sufficiently close, but not in Ohmic contact, i. e. in tunneling condition, a bias voltage is applied between these two objects so that a tunneling current flows through the system. Assuming that the STM tip is grounded, V will be, therefore, the voltage applied to the sample. This means that if $V > 0$ electrons will tunnel from the occupied states of the tip

to the unoccupied states of the sample. The tunneling current will be then amplified and through a feedback system, the distance between the tip and the sample surface will be controlled in order to keep the tunneling current constant (constant current operation mode). Thereby, if a tunneling current greater than the reference value is detected, the feedback system, connected to the piezoelectric motors will drive the tip away from the sample surface, decreasing the tunneling current (remember that the transmission coefficient depends exponentially on the potential barrier width, which, in this case, is related to the tip-sample distance). If the detected tunneling current is less than the reference value piezoelectric motors will approach the STM tip towards the sample, increasing the tunneling current to keep it constant (see Fig. 3.4, left panel). As a result of this process the surface of the sample will be mapped into topographic images shown in a color-code that represents a combination between height and electronic variations, since the tunneling current also depends on the density of states of the sample [99], as will be shown in the following sections. In the constant height operation mode, on the other hand, the tip path will be fixed during the entire sample surface scan. As a consequence, the tunneling current will vary according to the structure of the sample (Fig. 3.4, right panel).

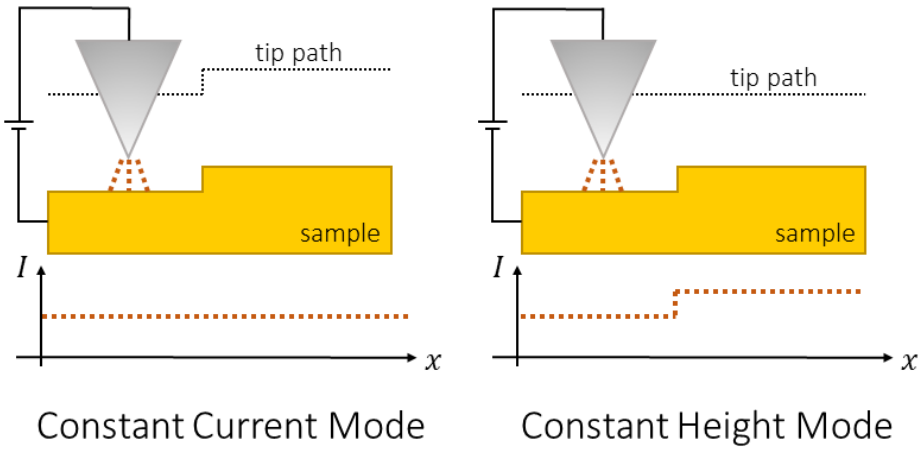

FIG. 3.4 – Operation modes of a scanning tunneling microscope. In the left panel one sees constant current operation mode in which the tunneling current is kept constant and the distance between tip and sample varies. In the right panel, constant height operation mode is presented. In this case, the distance between the tip and the sample is kept constant and, consequently, the tunneling current varies.

3.1.3 BARDEEN THEORY OF TUNNELING

For a better understanding of the STM technique a more sophisticated theory, like the Bardeen theory of tunneling, is required. It will permit us to comprehend some aspects that would, otherwise, be difficult to explain.

To estimate the tunneling current through the potential barrier, we will assume that the STM tip and the sample are far apart from each other, so that their electronic structures can be considered separately. As a consequence, their non-perturbated wave functions will obey independent Schrödinger's equations. Thereby, for the STM tip, it is correct to write [99, 102, 103]:

$$i\hbar\frac{\partial\Psi_{\mathrm{T}}}{\partial t}=\left[\frac{-\hbar^2}{2m}\frac{\partial^2}{\partial z^2}+U_T\right]\Psi_{\mathrm{T}}, \tag{3.13}$$

where $U_T(z)$ is the potential energy of the tip, which is defined as $U_T(z)=U(z)$ for the regions of the tip and the potential barrier, $z>z_1$, and $U_T(z)=0$ for the region of the sample, $z<z_1$ (see Fig. 3.5). Moreover, $\Psi_{\mathrm{T}}=\psi_\mu^T e^{-iE_\mu^T t/\hbar}$ and ψ_μ^T, the spatial wave function of the tip, obeys the equation:

$$\left[\frac{-\hbar^2}{2m}\frac{\partial^2}{\partial z^2}+U_T\right]\psi_\mu^T=E_\mu^T\psi_\mu^T. \tag{3.14}$$

Similarly for the sample [99, 102, 103]:

$$i\hbar\frac{\partial\Psi_{\mathrm{S}}}{\partial t}=\left[\frac{-\hbar^2}{2m}\frac{\partial^2}{\partial z^2}+U_S\right]\Psi_{\mathrm{S}}, \tag{3.15}$$

where $U_S(z)$ is the potential energy of the sample, which is defined as $U_S(z)=U(z)$ for the region of the sample, $z<z_1$, and as $U_S(z)=0$ for the regions of the potential barrier and the tip, $z>z_1$. The solution of this expression is $\Psi_{\mathrm{S}}=\psi_\nu^S e^{-iE_\nu^S t/\hbar}$, where ψ_ν^S, the spatial wave function of the sample, satisfies:

$$\left[\frac{-\hbar^2}{2m}\frac{\partial^2}{\partial z^2}+U_S\right]\psi_\nu^S=E_\nu^S\psi_\nu^S. \tag{3.16}$$

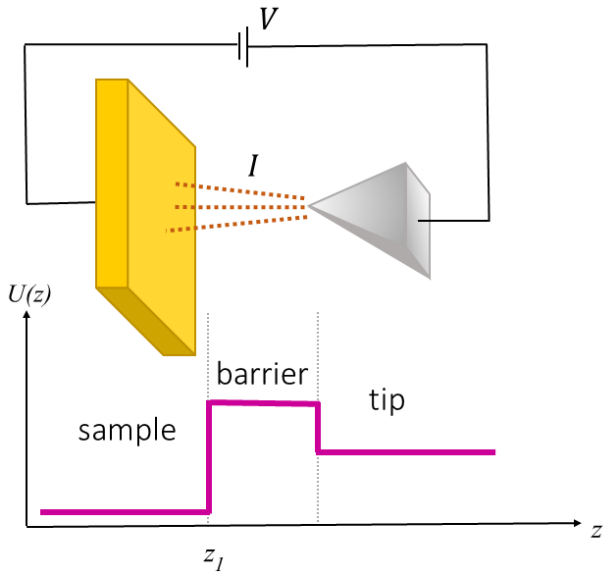

FIG. 3.5 – Simplified schematic view of a scanning tunneling microscope showing the tip and the sample and their potential energies.

As the tip and the sample approach to each other, decreasing the distance between them, the transmission coefficient increases. Once the tunneling condition is reached, i. e. the tip-sample separation is sufficiently small, a tunneling current will be established, as a result of transfer electrons from occupied states of the sample to unoccupied states of the tip, or vice-versa. The tunneling current is influenced by the combined potentials of tip and sample, so that Ψ, the evolved state of the system, is now governed by the following Schrödinger's equation [103]:

$$i\hbar\frac{\partial\Psi}{\partial t} = \left[\frac{-\hbar^2}{2m}\frac{\partial^2}{\partial z^2} + U_S + U_T\right]\Psi. \tag{3.17}$$

In this new approach the term U_T has now a temporal dependency. It will be assumed that for $t \to -\infty$ there is a long distance between tip and sample so that it is correct to consider the electron in a stationary state of the sample, namely ψ_v^S. If the STM tip slowly approaches the sample, we can assume that $U_T(t)$ has an adiabatic behavior [103]:

$$U_T(t) = e^{\eta t/\hbar}U_T, \tag{3.18}$$

where η is a positive integer. At the end of the process, when the tip is close enough to the sample, we will make $\eta \to 0$ and, consequently, the potential will be constant for every

t. In such conditions, ψ_ν^S, described by equation 3.16 at $t \to -\infty$, will not evolve according to 3.15 anymore. This is because the electron has now a probability of tunneling through the potential barrier, since the tip-sample distance is now reduced.

Since the tunneling current is the result of transfer electrons from occupied states of the sample to unoccupied states of the tip, to estimate its magnitude it is essential to determine the probability of electron tunneling through the potential barrier. This requires the determination of the state of the combined tip-sample system, which can be written simply as a linear combination of the wave functions of sample, ψ_ν^S, and tip, ψ_μ^T [99, 102, 103]:

$$\Psi = \psi_\nu^S e^{-iE_\nu^S t/\hbar} + \sum_{\mu=1}^{\infty} c_\mu(t)\psi_\mu^T e^{-iE_\mu^T t/\hbar}, \tag{3.19}$$

where $c_\mu(t)$ was inserted due to the temporal dependency of $U_T(t)$. Assuming that $c_\mu(-\infty) = 0$ and the wave functions ψ_μ^T and ψ_ν^S are orthogonal; substituting expression 3.19 in 3.17 we obtain:

$$i\hbar \sum_{\mu=1}^{\infty} \frac{dc_\mu(t)}{dt}\psi_\mu^T e^{-iE_\mu^T t/\hbar} = U_T \psi_\nu^S e^{-i(E_\nu^S + i\eta)t/\hbar} + U_S \sum_{\lambda=1}^{\infty} c_\lambda(t)\psi_\lambda^T e^{-iE_\lambda^T t/\hbar}. \tag{3.20}$$

Neglecting the second term on the right-hand side of the equation above for being an infinitesimal quantity, the expression becomes:

$$i\hbar \frac{dc_\mu(t)}{dt} = \int_{z>z_1} \psi_\nu^S U_T \, \psi_\mu^{T^*} e^{-i(E_\nu^S - E_\mu^T + i\eta)t/\hbar} d^3\boldsymbol{r}, \tag{3.21}$$

which is only defined for $z > z_1$, where $U_T \neq 0$. Defining the tunneling matrix element $M_{\nu\mu}$, as:

$$M_{\nu\mu} \equiv \int_{z>z_1} \psi_\nu^S U_T \, \psi_\mu^{T^*} d^3\boldsymbol{r}, \tag{3.22}$$

the coefficient $c_\mu(t)$ can be written as:

$$c_\mu(t) = M_{\nu\mu} \frac{e^{-i(E_\nu^S - E_\mu^T + i\eta)t/\hbar}}{(E_\nu^S - E_\mu^T + i\eta)}. \tag{3.23}$$

3.1.4 SCANNING TUNNELING SPECTROSCOPY

Combining expressions 3.19 and 3.23, Ψ can be determined and, consequently, the probability of transferring electrons from occupied states of the sample to the unoccupied states of the tip over time, $P_{\nu\mu}$, can be calculated. $|\, c_\mu(t)\,|^2$, which describes the probability of an electron, initially described by ψ_ν^S at $t = -\infty$, populate the state ψ_μ^T at time t is [103]:

$$|\, c_\mu(t)\,|^2 = |\, M_{\nu\mu}\,|^2 \frac{e^{2\eta t/\hbar}}{(E_\nu^S - E_\mu^T)^2 + \eta^2}. \tag{3.24}$$

Thus, the probability of tunneling per unit of time, defined as $P_{\nu\mu}(t) = \frac{d|c_\mu(t)|^2}{dt}$, will be [103]:

$$P_{\nu\mu}(t) = \frac{2\eta |M_{\nu\mu}\,|^2}{\hbar} \frac{e^{2\eta t/\hbar}}{(E_\nu^S - E_\mu^T)^2 + \eta^2}. \tag{3.25}$$

Taking the limit $\eta \to 0$, for which the tip is sufficiently close to the sample and U_T is constant in time and using $\delta(x) = \frac{1}{\pi}\lim_{\eta\to 0} \frac{\eta}{x^2+\eta^2}$ one obtains:

$$P_{\nu\mu} = \frac{2\pi}{\hbar} |M_{\nu\mu}\,|^2\, \delta(E_\nu^S - E_\mu^T), \tag{3.26}$$

where the term $\delta(E_\nu^S - E_\mu^T)$ guarantees the elastic tunneling condition (the inelastic case will not be studied here).

So far, we have considered the transfer of a single electron from occupied state ν to an unoccupied state μ. However, in order to make this calculation more accurate it is necessary to take into account the state spectrum of the tip and the sample. To do so we will sum the tunneling current over ν and μ for each spin state. In addition, the Fermi distribution, $f(E - E_F) = \{1 + exp[(E - E_F)/k_B T]\}^{-1}$, will also be included into the formulation. Thus, for a bias voltage V applied between tip and sample, the tunneling current ($I \propto eP_{\nu\mu}$) will be [99, 103]:

$$I_{S\to T} = \frac{4\pi e}{\hbar} \sum_{\nu\mu} f\big(E_\nu^S - E_F^S\big)[1 - f(E_\mu^T - E_F^T)]\; |\, M_{\nu\mu}\,|^2\; \delta(E_\mu^T - E_\nu^S - eV), \tag{3.27}$$

$$I_{T\to S} = \frac{4\pi e}{\hbar}\sum_{\nu\mu} f\left(E_\mu^T - E_F^T\right)[1 - f(E_\nu^S - E_F^S)] \mid M_{\nu\mu} \mid^2 \delta(E_\mu^T - E_\nu^S - eV), \qquad (3.28)$$

where $I_{S\to T}$ is related to transfer of electrons from sample to tip and the opposite for $I_{T\to S}$. Note that $f(E - E_F)$ is ascribed to occupied states and $1 - f(E - E_F)$ to unoccupied states. The subtraction of these two tunneling currents gives us the total tunneling current:

$$I = \frac{4\pi e}{\hbar}\sum_{\nu\mu}[f\left(E_\nu^S - E_F^S\right) - f\left(E_\mu^T - E_F^T\right)] \mid M_{\nu\mu} \mid^2 \delta(E_\mu^T - E_\nu^S - eV) \qquad (3.29)$$

Using the electronic density of states, N, one can replace the sum over discrete states spectrum with an integral over energies [99, 103]:

$$I = \frac{4\pi e}{\hbar}\int_{-\infty}^{\infty}\left[f\left(E_F^S - eV + \varepsilon\right) - f(E_F^T + \varepsilon)\right]N_T(E_F^T + \varepsilon)N_S(E_F^S - eV + \varepsilon) \mid M \mid^2 d\varepsilon, \qquad (3.30)$$

where N_T and N_S are electronic density of states of tip and sample, respectively.

The Fermi distribution can be approximated by a step function if k_BT is less than the energy resolution of the system. Thus, the expression of the tunneling current, 3.30, can be written as:

$$I = \frac{4\pi e}{\hbar}\int_0^{eV} N_T(E_F^T + \varepsilon)N_S(E_F^S - eV + \varepsilon) \mid M \mid^2 d\varepsilon. \qquad (3.31)$$

Considering that M does not vary much in the integral range, the tunneling current will be:

$$I \propto \int_0^{eV} N_T(E_F^T + \varepsilon)N_S(E_F^S - eV + \varepsilon)\, d\varepsilon, \qquad (3.32)$$

a convolution between the electronic density of states of tip and sample.

Qualitatively, these concepts can be understood as follows: once a bias voltage, a negative one for instance, is applied between STM tip and sample, electrons will flow from occupied states of sample to unoccupied states of tip (considering that the tip is

grounded). Thus, the tunneling current will be influenced by the density of states of sample and tip as schematically shown in Fig. 3.6.

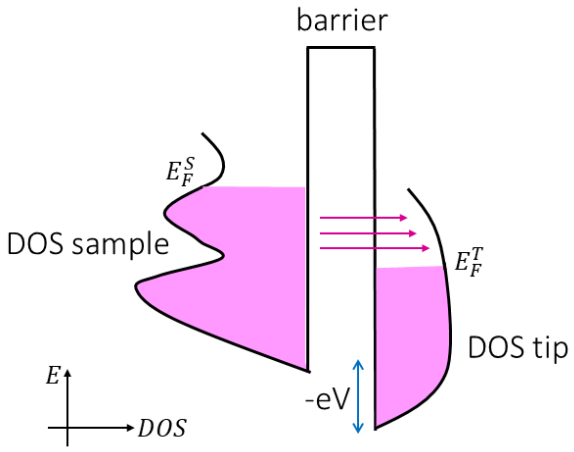

FIG. 3.6 – Schematic view of tunneling between STM tip and sample. In the representation shown, a negative bias voltage is applied to the sample and, consequently, electrons will tunnel from occupied states of sample to unoccupied states of tip.

The scanning tunneling spectroscopy technique basically consists of measuring the tunneling current at a single point of the sample defined by the STM tip position, which is atomically thin, as a function of the electron energy. Therefore, the tunneling current can be rewritten as:

$$I \propto \int_0^{eV} LDOS_{tip}(E_F^T + \varepsilon) LDOS_{sample}(E_F^S - eV + \varepsilon)\, d\varepsilon, \tag{3.33}$$

where the electronic density of states of tip and sample were replaced by the local density of states of sample, $LDOS_{sample}$, and the local density of states of tip, $LDOS_{tip}$.

The derivative of the tunneling current as a function of the bias voltage will be [99]:

$$\frac{dI}{dV} \propto LDOS_{tip}(E_F^T + eV) LDOS_{sample}(E_F^S). \tag{3.34}$$

Analyzing this expression, one sees that for a negative voltage in the sample, with electrons tunneling from occupied states of sample to unoccupied states of tip, the derivative of the tunneling current is proportional to the local density of states of the tip

at the energy $E_F^T + eV$ and to the local density of states of the sample at the Fermi level, E_F^S. Whether one can guarantee that the local density of states of the tip is approximately constant, then one can infer the density of states of the sample (in fact, the local density of states of the tip, which depends on its material and its termination is not a constant, but in general this is a reasonable approximation). For a positive bias, on the other hand, the derivative of the tunneling current will be:

$$\frac{dI}{dV} \propto LDOS_{tip}(E_F^T) LDOS_{sample}\left(E_F^S + eV\right). \tag{3.35}$$

Thus, one sees from expressions 3.34 and 3.35 that depending on the signal of the bias voltage occupied or unoccupied states of the sample may be highlighted in the tunneling spectrum.

Therefore, the tunneling spectrum, dI/dV or STS, gives us information about the local density of states of the sample allowing the study of the electronic properties of different systems.

3.1.5 LOCK-IN AMPLIFIER TECHNIQUE

The combination of a scanning tunneling microscope with a lock-in amplifier, through the superposition of a sinusoidal signal to the STM tip voltage, provides an output signal proportional to the derivative of the tunneling current [104], which is, as previously mentioned, proportional to the local density of states of sample. The advantage of using this amplifier consists not only in the direct acquisition of the dI/dV signal, which allows, for example, spatially-resolved measurements of density of states [99, 104-107], but it also allows for the reduction of the electronic noise in the spectroscopic response [108, 109].

A lock-in is a type of amplifier based on phase-sensitive detection (PSD), which is used in measurements of alternating current (AC) signals. This technique, which basically consists of a phase-sensitive detector and a low pass filter (see Fig. 3.7), multiplies the input signal, which is being investigated, by a reference signal that has specific phase and frequency. This product will only have a non-zero average value over time for the case in

which its input and reference frequencies coincide as a consequence of the orthogonality of sinusoidal functions. Thus, when the lock-in amplifier integrates the multiplied signal over time, which is done through a low pass filter, it will select exclusively a part of the input signal that has the same frequency of the reference signal, attenuating other components with different frequencies or out-of-phase [108-112].

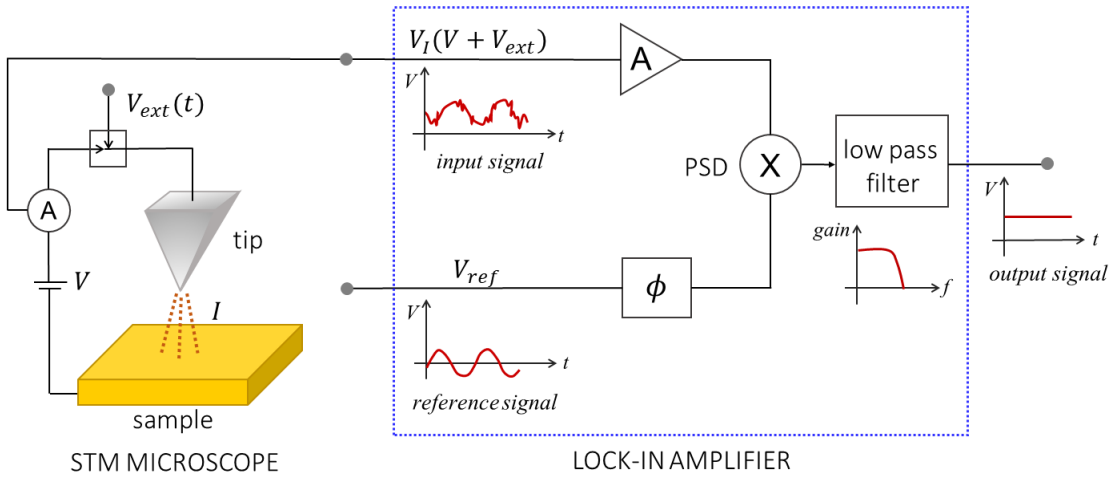

FIG. 3.7 – Schematic view of a scanning tunneling microscope connected to a lock-in amplifier. The tunneling current, modulated by an external sinusoidal signal, is multiplied by a reference signal through a PSD. The product goes into a low pass filter, which extracts its direct current (DC) component.

In particular, a lock-in amplifier can be used for the direct acquisition of the tunneling spectrum. In such case, the addition of a small AC voltage, $V_{ext} = A\sin(\omega t)$ to the STM bias voltage (ω is set so that it does not interfere in the acquisition of the STM images and the microscope's operation) will result in a response signal, i. e. the tunneling current I, also modulated. The tunneling current will act as a stimulus to a voltage, $V_I(V + V_{ext})$, which is directly related to it [104, 108]. In Fig. 3.7 one sees a scheme of a lock-in amplifier connected to a scanning tunneling microscope. If the amplitude of the sinusoidal signal is sufficiently small, then the tunneling current can be expanded into a Taylor series as:

$$V_I(V + V_{ext}) = V_I(V) + \left.\frac{dV_I}{dV}\right|_V A\sin(\omega t) + O(A^2) + \cdots \qquad (3.36)$$

This signal will be the input of the lock-in amplifier and will be amplified and multiplied by a reference signal, $V_{ref} = \sin(\omega_{ref}t + \phi)$. Using trigonometric identities of the sinusoidal functions this product can be written as [104, 108]:

$$V_I(V + V_{ext})\sin(\omega_{ref}t + \phi) = V_I(V)\sin(\omega_{ref}t + \phi) + \frac{A}{2}\frac{dV_I}{dV}\{\cos[(\omega_{ref} - \omega)t + \phi] - \cos[(\omega_{ref} + \omega)t + \phi]\} + \cdots \quad (3.37)$$

Whenever $\omega_{ref} \neq \omega$ this product will be zero in an average over time. However, if one can adjust $\omega_{ref} = \omega$ then this product becomes [104, 108]:

$$V_I(V + V_{ext})A\sin(\omega_{ref}t + \phi) = V_I(V)\sin(\omega t + \phi) + \frac{A}{2}\frac{dV_I}{dV}[\cos(\phi) - \cos(2\omega t + \phi)]. \quad (3.38)$$

Through a low pass filter one can extract the DC signal (this is because the frequency range used in the experiment is very small compared to the adjusted cutoff frequency), which is proportional to the first derivative of the tunneling current regarding to the bias voltage. We recall that this term is directly related to the local density of states of sample as discussed in previous sections. Adjusting the phase, in order to maximize the output signal, the proportionality term will be well-established. Thus, one can write [108]:

$$V_{out} \sim \frac{A}{2}\frac{dV_I}{dV}\cos(\phi) \quad (3.39)$$

Additionally, any other signal or noise with a different frequency will be filtered through the reference signal's adjustment, producing a noiseless signal as the output of the lock-in amplifier. This can be clearly seen in Fig. 3.8, in which tunneling spectra of a Bi_2Se_3 sample obtained with and without the use of a lock-in amplifier, are shown. In the left panel of Fig. 3.8 one sees a tunneling spectrum directly acquired through a lock-in amplifier. In the right panel of Fig. 3.8, on the other hand, it is presented a tunneling spectrum obtained directly from the STM microscope. This curve was acquired by a process of numerical differentiation of the $I(V)$ curve. As one observes from the direct comparison between these two results, the curve acquired without a lock-in amplifier is

much noisier when compared to the curve obtained using the lock-in amplifier. This demonstrates the advantage in using this equipment for STS measurements [113].

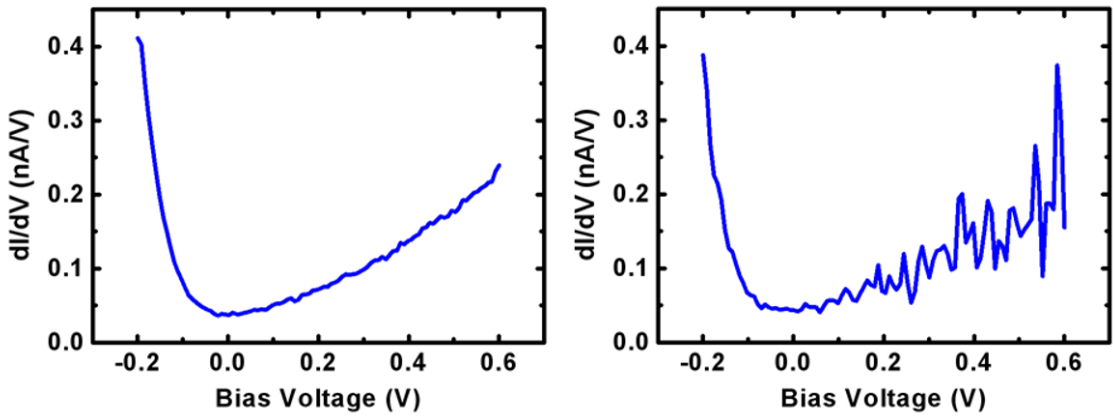

FIG. 3.8 – Tunneling spectra obtained (left panel) with and (right panel) without the use of a lock-in amplifier. The sample measured is a topological insulator, namely Bi_2Se_3. Figure taken from reference [113].

3.1.6 EXPERIMENTAL SETUP AND EXAMPLES OF MEASUREMENTS

In Fig. 3.9 it is presented the experimental setup of the 'Nanoscopia UHV' laboratory at Universidade Federal de Minas Gerais, Brazil. In the left panel one sees a NanoSurf microscope, which works under air conditions and room temperature. In the right panel a variable temperature Omicron VT-STM that works in ultra-high vacuum conditions is presented. These scanning tunneling microscopes were used in the measurements shown in chapters IV and V of this thesis.

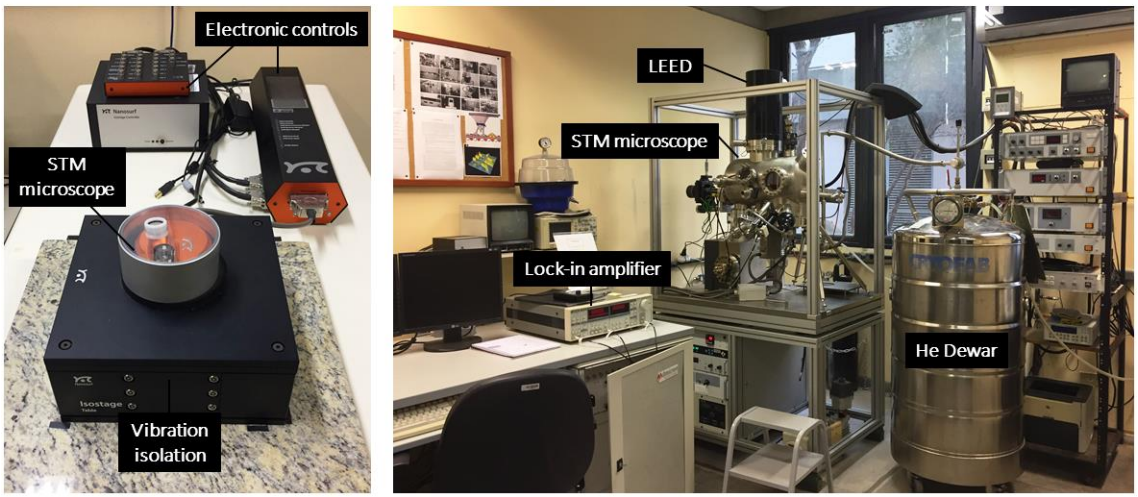

FIG. 3.9 – Scanning tunneling microscopes of the 'Nanoscopia UHV' laboratory, Brazil. (Left panel) A NanoSurf microscope that operates under air conditions and room temperature. This microscope is equipped with a vibration isolation and a lock-in amplifier (not shown in this figure). (Right panel) Omicron variable temperature microscope. In this panel one sees a lock-in amplifier connected to the scanning tunneling microscope, a low-energy electron diffraction (LEED) and helium Dewar used for cooling the system.

In Fig. 3.10 one sees the experimental setup of TuMA III, one of the microscopes of the 'Experimentelle Nanophysik' laboratories at Universität Siegen, Germany. This machine is equipped with an evaporator, a quadrupole mass spectrometer (QMS), LEED, ion gun and a scanning tunneling microscope which operates in ultra-high vacuum conditions and in the temperature range of 140 K up to 600 K. This machine was used during my doctoral stay in Germany to measure the experimental results presented in chapter VI.

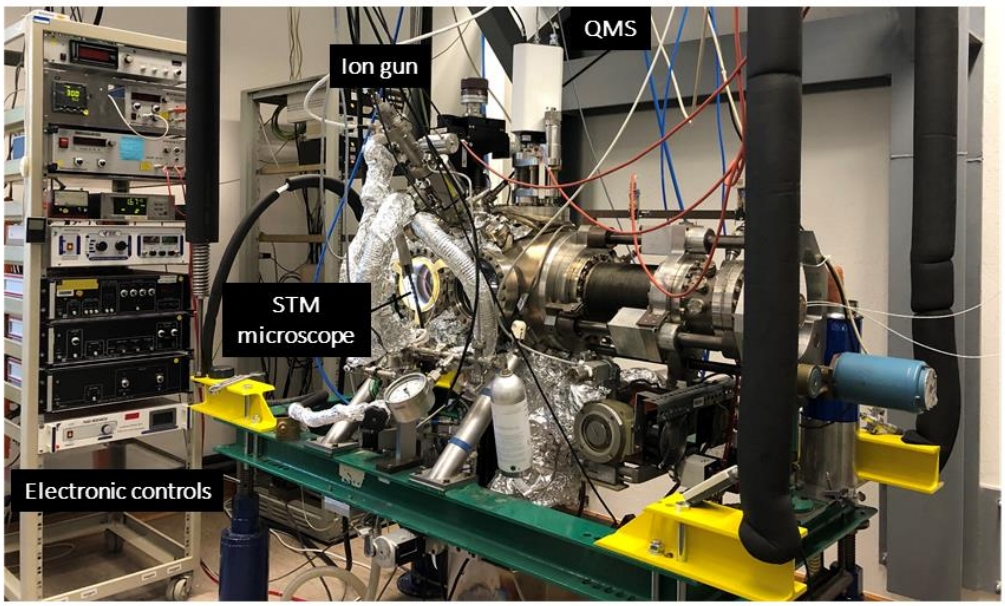

FIG. 3.10 – Microscope TuMA III at the 'Experimentelle Nanophysik' laboratory, Germany. This machine is equipped with an evaporator (not visible in this image), a quadrupole mass spectrometer (QMS), LEED (also not visible) and ion gun. It operates in ultra-high vacuum conditions.

As an example of this technique, we present some results obtained using STM. Fig. 3.11 presents some STM images of a graphene sample grown on a polycrystalline copper substrate via chemical vapor deposition (CVD), which was investigated during my Master's degree. In this work STM and STS were used to study the interplay between atomic and electronic structure of the sample. In particular, STM images revealed the epitaxial match between the graphene sheet and the underlying substrate in different crystallographic orientations, through the observation of distinct moiré patterns [114, 115].

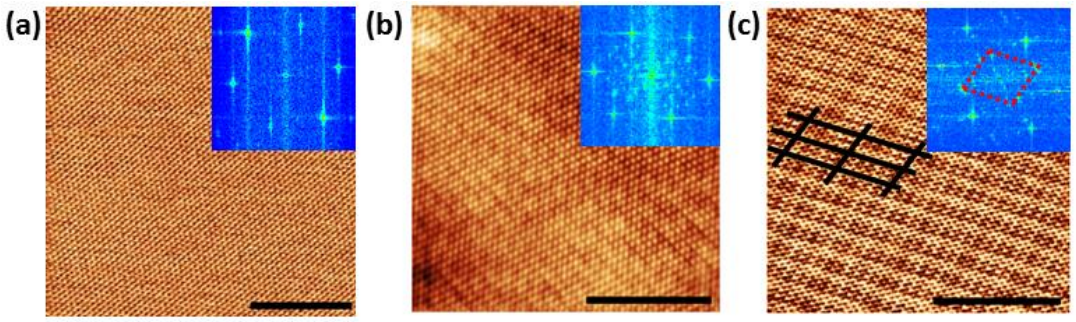

FIG. 3.11 – STM topographic images from different regions of graphene on a polycrystalline copper substrate. Images (a) of a very flat graphene area, (b) of an area with an approximately hexagonal moiré pattern and (c) of a region with a nearly rectangular moiré pattern. In the insets of these figures one sees the corresponding Fourier transforms. The scale bars are: (a) 4 nm, (b) 4 nm and (c) 5 nm. Images adapted from reference [115].

In Fig. 3.11a one visualizes a particular region where there is no strain imposed by the substrate. For the regions shown in Figs. 3.11b and 3.11c, on the other hand, we observe two different moiré patterns formed by the superposition of graphene and copper lattices. These structural differences significantly influence the electronic properties of each of these systems. For further details see reference [115].

Additionally, in Fig. 3.12a we present some STM images of a quantum corral made with Ag adatoms on top of Ag(111) [105]. In this structure, obtained by the manipulation of atoms using the scanning tunneling microscope itself, the Ag adatoms work as a potential barrier able to confine electrons. Spectroscopic maps (see Fig. 3.12b), obtained using a lock-in amplifier, show different standing wave patterns of the surface states confined within the quantum corral, besides scattered waves outside the triangular structure [99, 105].

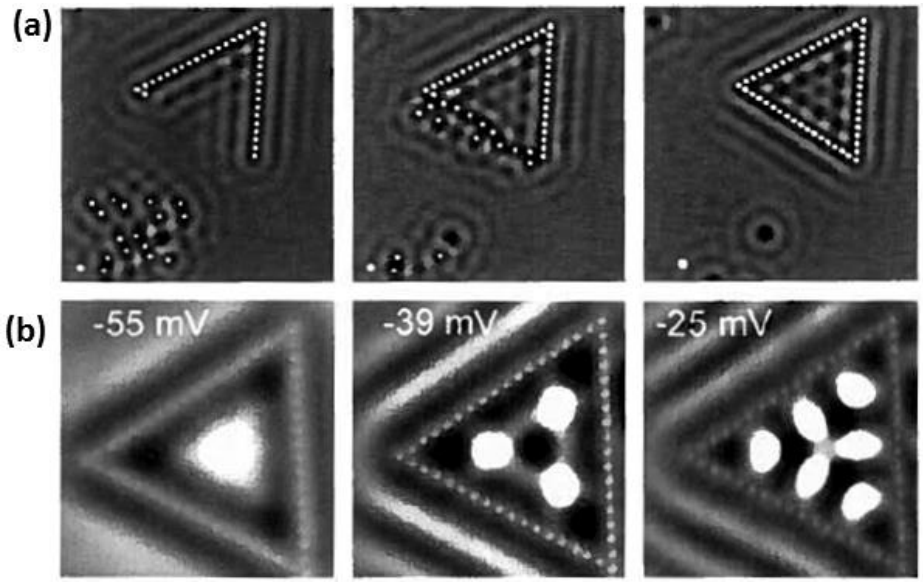

FIG. 3.12 – (a) STM topographic images of a triangular quantum corral formed with Ag adatoms on a Ag(111) substrate. (b) Maps of electronic density of states of the quantum corral shown in (a) for different energies (depicted in each panel). Images taken from references [99] and [105].

3.2 ANGLE-RESOLVED PHOTOEMISSION SPECTROSCOPY

Angle-resolved photoemission spectroscopy (ARPES) is a powerful experimental tool to investigate electronic states near the Fermi level. This technique is based on the photoelectric effect first observed by H. R. Hertz in 1887 and later explained by A. Einstein in 1905 [116]. For this finding he was awarded with the Nobel Prize in Physics in 1921 [117]. Illuminating a sample, either using a He-discharge lamp or synchrotron radiation, will result in the photoemission of its electrons. The analysis of the kinetic energy of these electrons through an angular scan permits the reconstruction of the dispersion relation of the system investigated and an in-depth comprehension of its electronic properties.

3.2.1 PHOTOELECTRIC EFFECT

The experimental observation of the photoelectric effect was made in the 19th century after detecting an electronic current (electrons were attracted to an anode through the application of a bias voltage) when illuminating a metallic plate in a vacuum

environment. Some of the observations of this experiment are shown in Fig. 3.13. Particularly, it was concluded that: (i) there was a cutoff frequency (that varies depending on the material of the plate), below which the photoelectric effect was not observed (Fig. 3.13a and 3.13b); (ii) the number of photoelectrons depended on the intensity of the light source, however, their kinetic energy was not affected by it (Fig. 3.13c and 3.13d); (iii) the electronic current was detected instantaneously, as soon as the metallic plate was illuminated, no delay was observed. These points raised questions about the nature of light that could not be answered by the classical wave theory [118].

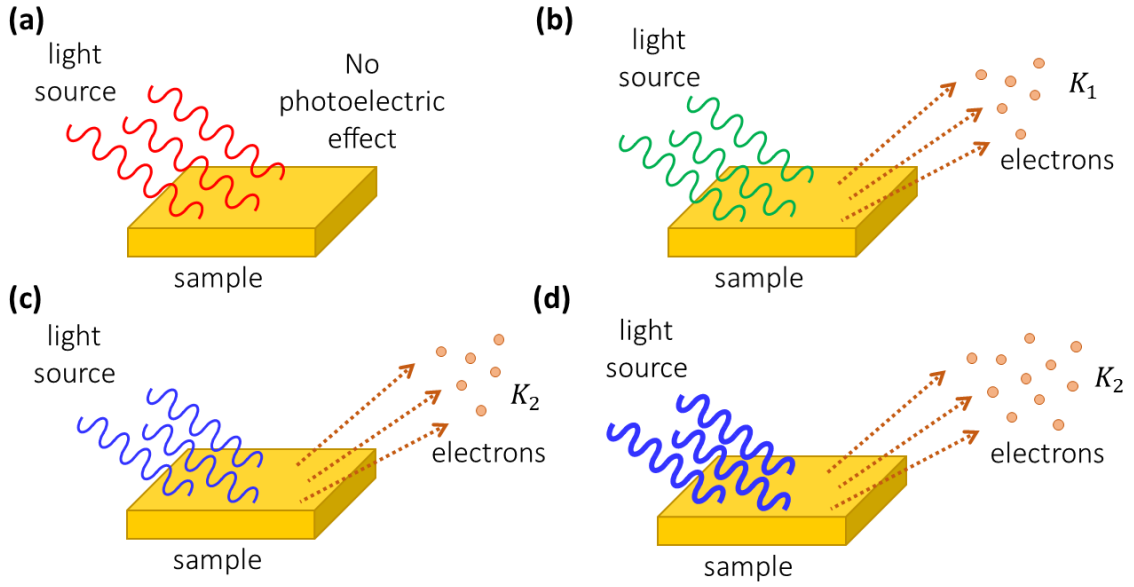

FIG. 3.13 – Schematic representation of the photoelectric effect. (a) Depending on the light source's frequency no electron is ejected from the sample and the photoelectric effect is not observed. (b) For frequencies above a cutoff value, electrons escape from the sample with kinetic energy, K_1. (c) For a more energetic light source (higher frequency) the kinetic energy of the electrons will be greater when compared to the previous case ($K_2 > K_1$). (d) A more intense light source does not alter the kinetic energy of electrons, just the number of electrons ejected.

This phenomenon was explained by A. Einstein who developed the quantum theory of light. He proposed the quantization of light in packets of definite energy, the photons. According to this theory, the energy of the photon is [116, 118]:

$$E = h\upsilon, \tag{3.40}$$

where h is the Planck's constant and υ the frequency of light. The photoemission occurs whenever the photon energy absorbed by the electrons in the sample exceeds the energy that binds them in the material. In particular, the maximum kinetic energy, K_{max}, of an electron ejected from the sample surface is:

$$K_{max} = h\upsilon - \phi, \tag{3.41}$$

where ϕ is the work function that represents the minimum energy necessary to remove an electron from the sample.

With these arguments the experimental observations, previously mentioned, could be explained. The existence of a cutoff frequency, for instance, is understood making $K_{max} = 0$, which results in $h\upsilon_c = \phi$, where υ_c is the cutoff frequency. This expression tells us that photons with energy $h\upsilon_c$ have the minimum energy necessary to eject electrons. Thus, if the light source has a frequency $\upsilon < \upsilon_c$ the photoelectric effect will not occur. Additionally, equation 3.41 shows that K_{max} does not depend on the intensity of the light source, but only the photon energy. Therefore, by increasing the intensity of the light source, the number of photons also increases and, consequently, the number of electrons ejected increases as well. However, this does not affect the kinetic energy of the electrons, since the energy of the photons remains unaltered. Finally, the absence of any delay in the emission of electrons is fully understood by the concept of the photon itself. The idea that the energy is now storage in packets, differently from the classical theory, in which the energy of the light source was uniformly distributed in the front wave, makes the absorption of photons and the emission of electrons an instant process [118].

3.2.2 THEORY OF ARPES

In a typical ARPES experiment either a He-discharge lamp or synchrotron radiation is used to illuminate the sample in a vacuum environment. The electrons emitted through the photoelectric process, ejected from the sample in all directions, will be then collected through an electron analyzer, where one can measure its kinetic energy, K, for a certain emission angle $(\theta, \emptyset)$. In Fig. 3.14a a schematic view of the experimental configuration

of an ARPES measurement is presented. Through this scheme one can determine the relationship between the momentum of the electrons ejected (the superscript o refers to the electrons outside the sample) and the emission angles as [119]:

$$k_x^o = \frac{\sqrt{2Km}}{\hbar}\sin(\theta)\cos(\phi), \tag{3.42}$$

$$k_y^o = \frac{\sqrt{2Km}}{\hbar}\sin(\theta)\sin(\phi), \tag{3.43}$$

$$k_z^o = \frac{\sqrt{2Km}}{\hbar}\cos(\theta), \tag{3.44}$$

where m is the mass of the free electron.

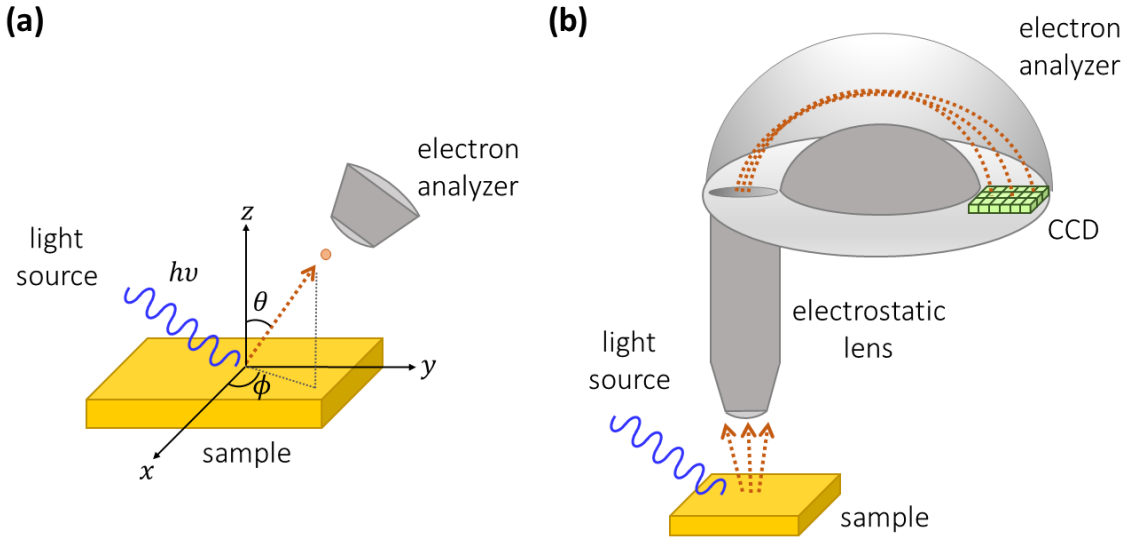

FIG. 3.14 – (a) Schematic representation of the photoelectric effect showing the emission angles θ and ϕ and the entrance of the electron analyzer. (b) Schematic view of a typical ARPES setup showing the electrostatic lens, the electron analyzer, where the electrons are curved by an electric field and the charge coupled device (CCD).

The photoemitted electrons go directly to an electron analyzer after passing through a series of electrostatic lens. In the analyzer the electrons are curved by an electric field and then are detected in a CCD, which works as a detector (Fig. 3.14b). By determining the trajectory of the electrons in the analyzer their kinetic energy can also be known. This, together with an appropriate angle scan, permits us to determine the dispersion relation of the system.

Using the laws of conservation of energy and momentum it is possible to correlate this information with the sample binding energy, E_B, and the momentum of the electrons inside it. In particular, it is correct to write:

$$K = h\upsilon - \phi - |E_B|. \tag{3.45}$$

Using this expression, the binding energy is completely determined. Additionally, neglecting the momentum of the incident photon, for being infinitesimal for low energies, the parallel components of the momentum of the electron (denoted by the symbol //) are conserved:

$$\vec{k}_{//}^{\,i} = \vec{k}_{//}^{\,o}, \tag{3.46}$$

where the superscript i refers to the electrons inside the sample. Combining this expression with equations 3.42 and 3.43 one can directly obtain the momentum of the electrons inside the sample in directions k_x and k_y. Due to the translational symmetry being broken, the momentum is not conserved in the k_z direction. However, information about this direction can be obtained varying the energy of the light source as one sees in the expression below, which is an approximation for electrons near the Fermi level [119, 120]:

$$h\upsilon = \frac{\hbar^2 {k_z^i}^2}{2m} + \phi - V_0, \tag{3.47}$$

where V_0 is the inner potential. Thus, through the variation of the incident photon energy, which requires the use of synchrotron radiation, it is possible to do a complete reconstruction of the dispersion relation of the sample and also differentiate bulk and surface states.

3.2.3 EXPERIMENTAL SETUP

In Fig. 3.15 is presented the experimental setup of the ARPES instrument, used in the measurements presented in this thesis, located at the PGM beamline at the Brazilian Synchrotron Light Laboratory (LNLS) in Campinas, Brazil.

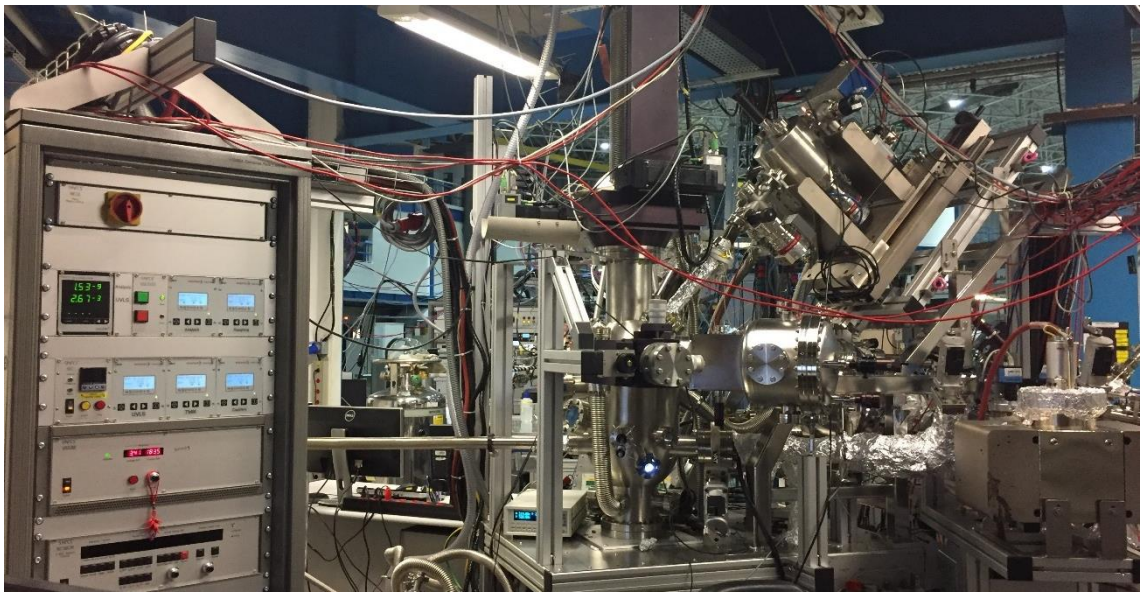

FIG. 3.15 – Experimental setup of the ARPES instrument at the PGM beamline at LNLS, Brazil.

As briefly discussed in the previous section, the sample is positioned in the manipulator where one can control the emission angles with respect to the light source. In the experimental setup used, the emission angles are schematically indicated in Fig. 3.16a, where φ permits the rotation of the sample and ξ is related to the opening angle for the entrance of the electrons in the analyzer. This angle determines the part of the dispersive plane that will be collected by the analyzer for a given φ, which will be varied throughout the experiment [119].

The electrons emitted from the sample, as a consequence of the photoelectric effect, go to a series of electrostatic lenses, which can control the opening angle ξ and also direct them to the electron analyzer (Fig. 3.16a and 3.16b). In the electron analyzer, composed of two concentric hemispheres with a bias voltage applied between them, the electrons are curved by an electric field to then reach a 2D detector (Fig. 3.16b). The configuration of the lenses together with the bias voltage of the analyzer are such that they select the energy range ($E_p \pm \delta$, where E_p is the energy pass) of the electrons that will be detected. Electrons with energy out of the range reach the walls of the analyzer and are not detected in the CCD. The energy pass can be controlled by the user and is directly related to the resolution of the results obtained [119].

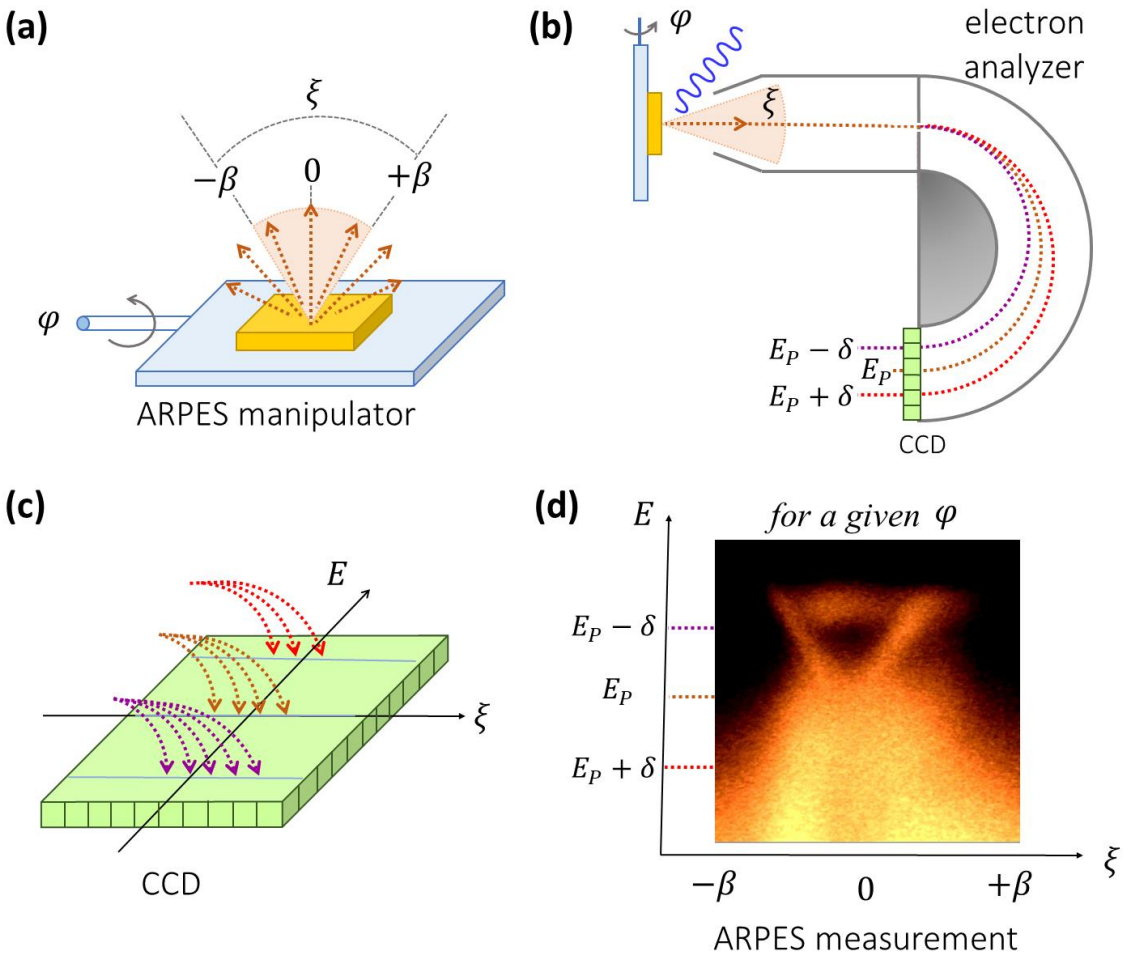

FIG. 3.16 – (a) Schematic representation of the sample in the ARPES manipulator. The angle φ permits the rotation of the sample with regard to the light source and the angle ξ determines part of the dispersive plane of the electrons that will be collect by the analyzer. (b) Schematic view of the electron analyzer. The electrons with different kinetic energies have different trajectories in the analyzer, where they are curved by an electric field. The energy pass, E_p, is chosen to be positioned in the center of the CCD camera, where the electrons are detected. (c) Electrons with the same kinetic energy describe the same trajectory and reach the CCD in a line of fixed energy, but different ξ, which depends on their momentum. (d) ARPES measurement of the topological insulator Bi_4Te_3.

The trajectory of the electrons in the analyzer is determined by their kinetic energy so that electrons with different values of momentum, but with the same trajectory, reach the detector in a line of fixed energy (Fig. 3.16c). During this whole process the momenta of the photoelectrons are preserved and their patch in the analyzer is such that they reach the microchannel plate (MCP). Afterwards they are accelerated into a phosphorous screen where the image is collected by a CCD camera in the correct

positions regarding to the values of k and ξ. Fig. 3.16d presents a typical ARPES measurement, for a sample of Bi_4Te_3 (further investigated in chapter V), which represents a slice of the three-dimensional (E, $\vec{k}_{//}$) Brillouin zone. By varying the angle φ one can access different regions of the Brillouin zone and measure the dispersion relation at different symmetry points and, consequently, obtain different information. Additionally, as mentioned in the previous section, to recover information about the dispersion relation in the z direction, one must vary the energy of the light source.

Considering the angular configuration shown in Fig. 3.16a, $\vec{k}_{//}{}^{o}$ can be written as:

$$\vec{k}_{//}{}^{o} = \left(\frac{2mK}{\hbar^2}\right)^{1/2} [\sin(\xi)\boldsymbol{x} + \sin(\xi)\cos(\varphi)\boldsymbol{y}]. \tag{3.48}$$

Using this equation and 3.45 one can obtain the dispersion relation for the electrons inside the sample and also directly correlate it to theoretical information in order to study properties of different types of materials.

IV.

ELECTRONIC RESPONSE OF SELF-ASSEMBLED TRIANGULAR GRAPHENE NANOSTRUCTURES

In this chapter we investigate, using scanning tunneling microscopy and spectroscopy (STM/STS), structural and electronic properties of bilayer graphene films obtained through the graphitization of SiC(0001). It is reported the observation of triangular graphene nanostructures resulted from extended stacking faults in the SiC substrate, and their effects on graphene layers that are formed on top of them. Spectroscopic measurements revealed distinct electronic responses as a function of the local hydrogen intercalation. Spectroscopic signatures ranging from single- to double-layer graphene, as well as intermediate states were observed as a consequence of the (in)complete hydrogen intercalation process. In addition, high resolution topographic STM images at resonant bias voltages inside triangular nanostructures revealed that the bottom layer of the bilayer graphene film is still bonded to the substrate, indicating the coexistence of carbon atoms in sp^3 and sp^2 hybridizations. Using atomistic calculations, we have modeled the local density of states of these objects reproducing their electronic response.

4.1 INTRODUCTION

Graphene (as discussed in detail in chapter II), a honeycomb 2D crystal composed of carbon atoms, has attracted an extensive research focused on its remarkable properties that arise from its unique band structure and result in a massless behavior of the Dirac fermions [1-4]. Engineering of graphene electronic structures is currently mandatory for the understanding of novel phenomena as well as to develop new technologies based on this material. There are different approaches aiming at the accomplishment of this task: stacking graphene layers, choosing an appropriate substrate and the fabrication of graphene nanostructures, for instance. The properties of stacked graphene depend on a series of parameters that include number of layers, stacking sequence [3, 4, 121] and their interaction with underlying substrates [115, 122-124]. In particular, the dispersion relation of a bilayer graphene with Bernal stacking gives the electrons a massive character that electronically distinguishes it from a single graphene sheet [4].

The role of interface effects is also extremely important, since all the atoms in a graphene layer are directly exposed to the surrounding environment. Alternative routes for graphene synthesis, allowing for scaling areas concerning to graphite exfoliation [51], have been developed using chemical vapor deposition (CVD) in different catalytic metal surfaces [5, 125, 126] as well as controlled sublimation of SiC substrates [127-131]. This last method is extremely relevant, since the graphene layers are formed directly on an insulating substrate, leaving it as the single conducting material of the sample, which is a major step for the development of devices based on graphene [13, 132-135]. In addition, graphene layers grown on SiC substrate do not need transfer procedures and their thickness control takes place through an ordered sheet by sheet growth process [136, 137].

Theoretical and experimental studies have addressed graphene nanostructures in the past years, including the formation and electronic structure of nanoribbons [138-140], islands [141-143] and quantum dots [106, 144, 145]. These works particularly focus on the understanding of properties that arise when graphene is subjected to different structural conditions that may, in the future, turn graphene nanostructures into

important ingredients to be used in novel electronic devices. Among experimental and theoretical results, many interesting features arise, such as the emergence of direct band gaps [138], spatial modulation of the density of states [141] and luminescence due to quantum confinement [144]. Indeed, these results ratify the role that graphene nanostructures may play on future nanodevices.

Here we present experimental conditions in which nanometer-sized triangular graphene nanostructures are stabilized on the surface of SiC(0001), nominally cover with bilayer graphene. The self-assembly of nanostructures by a similar method with respect to the one reported here was observed by Bolen et al. [146] for graphene layers on 4H-SiC substrates, with the coexistence of several distinct morphologies such as dendritic structures (referred as 'fingers'), nano-triangles and hexagons, where these two last conditions appear as secondary morphologies only. The comprehension of the electronic response of these nanostructures is based on the vast knowledge that has been stablished in the past years on graphene monolayers and, more recently, on bilayer structures.

In this chapter we have used atomically-resolved STM and STS to study structural and electronic properties of bilayer graphene films on SiC(0001). Initial graphene samples were obtained by the graphitization of a SiC substrate followed by hydrogen intercalation, resulting in quasi-free-standing bilayer graphene. Our study revealed that triangular graphene nanostructures are formed, consisting of downward and upward steps which we named nanoholes and nanoplateaus, respectively. STM/STS measurements allowed us to unveil the electronic behavior of these nanostructures, which are structurally related to the presence of stacking faults in the SiC substrate. Local spectroscopic measurements also revealed different types of electronic responses, spanning from single to bilayer signatures, i. e. a dual electronic response which is associated with the level of hydrogen coverage. These electronic features were modeled using tight-binding calculations, which allow interpreting the differences in the experimental spectra. All results show that the local density of states below and above the Fermi level behaves asymmetrically because of the interactions within triangular nanostructures with the substrate. The asymmetry stems from quantum confined states in the bottom layer.

4.2 SAMPLE GROWTH: BILAYER GRAPHENE FORMATION

The bilayer graphene grown on SiC(0001) and studied in this work was synthesized in a collaboration with M. H. Oliveira Jr. (UFMG, Brazil) and J. M. J. Lopes (PDI, Germany). This process is composed by two main steps, known as graphitization and hydrogen intercalation. The graphitization consists in the creation of a partially attached bilayer graphene, obtained by the sublimation of a 6H-SiC substrate terminated in Si atoms. Our substrates were obtained from a n-type wafer polished on the (0001) face and cleaned with n-butyl-acetate, acetone and methanol. After this chemical cleaning, the substrate was subjected to an H-etching treatment, carried out at 1673 K for 15 minutes in an Ar:H mixture (95%:5%) atmosphere at 900 mbar. These procedures prepare the surface of the substrate for the graphene synthesis, sketched in Fig. 4.1a. Afterwards the graphitization process takes place at 1873 K for 15 minutes in a 900 mbar Ar atmosphere, as a consequence of the difference in the vapor pressure between the Si atoms (which sublimate more effectively) and C atoms (which remain) [147]. Once the graphene layer (MLG) is formed its interaction with SiC is mediated through a carbon layer partially attached to the substrate, known as buffer layer (BL) [129, 147, 148]. C atoms with sp^3 and sp^2 hybridizations may be found in this structure. This scenario, where a partially attached bilayer graphene (MLG + BL) is obtained is schematically represented in Fig. 4.1b.

STM and STS were used to study the morphology of the sample surface and to investigate its electronic properties. These measurements were performed in an Omicron VT-STM (UFMG, Brazil) operating at low temperature ($T = 25$ K) and ultrahigh vacuum conditions (2.0×10^{-11} mbar) in constant-current mode. All tunneling spectra presented in this chapter were obtained using a lock-in amplifier, connected to the STM, operating in a frequency of 2.67 kHz and a modulation amplitude of 4-10 mV. An STM topographic image of the sample after the graphitization process is presented in Fig. 4.1c. In this figure one observes large atomically flat regions of the sample and the presence of some steps on the left side of the image. In the inset of this figure one also observes a moiré pattern as a result of the high interaction between the MLG, the BL and the SiC(0001) substrate.

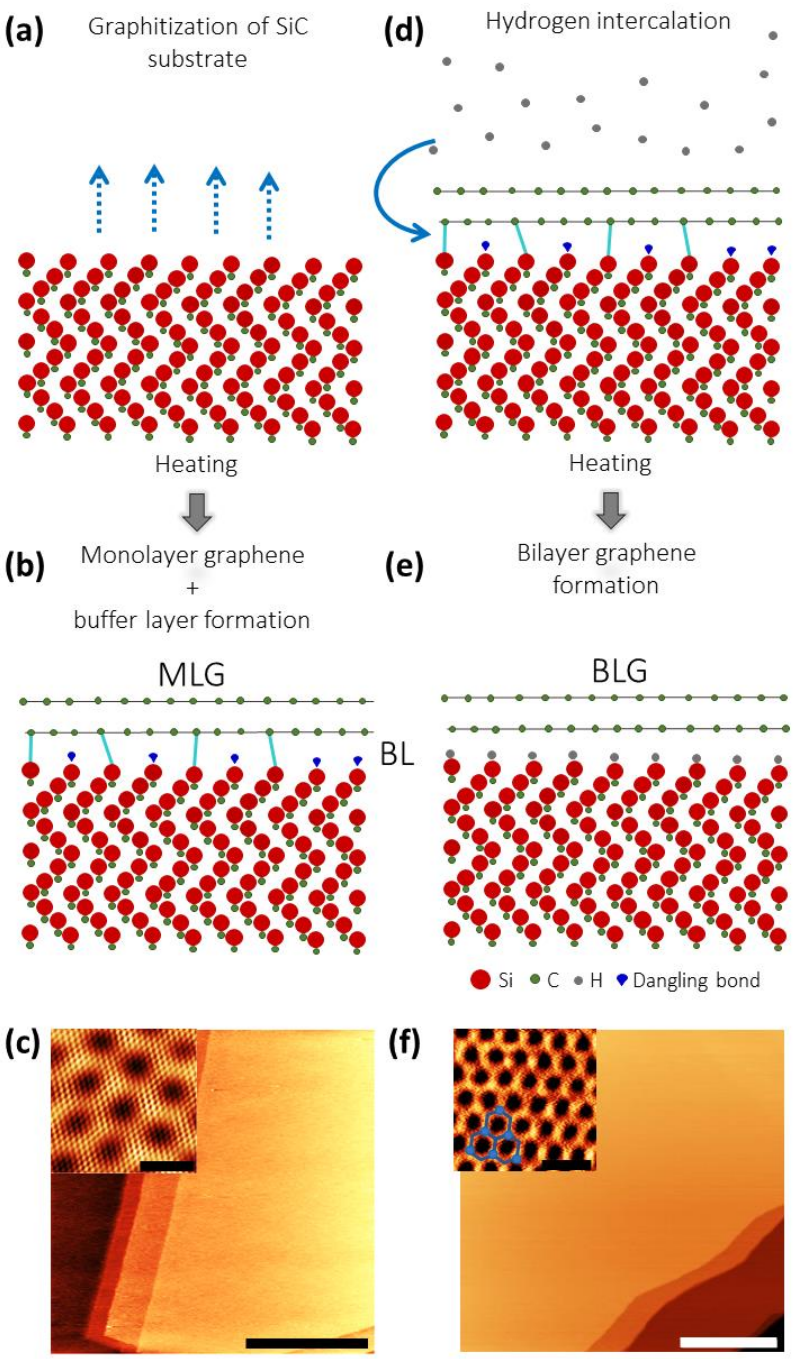

FIG. 4.1 – (a) Schematic view of the bilayer graphene growth. SiC is annealed in Ar atmosphere, resulting in the sublimation of the Si atoms while the C atoms re-organize, forming graphene sheets. (b) MLG formed at the surface is separated from the substrate by a carbon layer (buffer layer), covalently bound to SiC. (c) STM image of the sample after the graphitization process. The inset of this figure shows a moiré pattern that results from the interaction of the MLG, the BL and the SiC substrate. (d) After the hydrogen intercalation process, H atoms break the covalent bonds between SiC and the BL. (e) A detached bilayer graphene is obtained. (f) STM image of the system after the H intercalation. The inset of this figure shows the triangular pattern typical of Bernal stacking. The scale bars are: (c) 50 nm (main panel) and 2 nm (inset); (f) 50 nm (main panel) and 0.5 nm (inset).

The second step process is the H-intercalation, in which the BL is decoupled from the substrate and converted into an additional graphene sheet. In order to perform this second step, the sample is annealed at 1273 K for 2 hours in an Ar:H environment. As a consequence, H atoms intercalate underneath the buffer layer, breaking the covalent bonds that connect it to the substrate and producing a detached bilayer graphene (BLG). This procedure also passivates the SiC substrate [137] (Figs. 4.1d and 4.1e). Hereafter, any mention to MLG + BL refers to the system formed by a fully detached monolayer on top of a partially attached carbon layer (BL), while BLG refers to the fully detached system with two stacked graphene layers. In Fig. 4.1f an STM topographic image of the sample after the hydrogen intercalation is depicted. In the inset of Fig. 4.1f an atomically-resolved magnification of this flat region is shown. In this figure one observes that the structure of the system is completely different and the moiré pattern is no longer noticed. In particular, the triangular pattern that characterizes the Bernal stacking of a BLG is schematically indicated.

Fig. 4.2 shows the Raman spectrum of our sample in which the G and G' Raman peaks are indicated. This measurement allows one to identify the number of graphene layers in a system. In particular, the analysis of the G' Raman peak permits one to distinguish between monolayer and bilayer graphene systems. For the former the G' band can be fitted with only one Lorentzian with a full width at half maximum of 24 cm^{-1}, while for the later four Lorentzian peaks (all with the same full width at half maximum of 24 cm^{-1}) are necessary [130, 149-152]. As one sees in Fig. 4.2b, a zoom of the G' band, four Lorentzian were needed to fit this band which confirms a typical behavior of detached bilayer graphene for the system studied in this work.

A tunneling spectrum measured at a large atomically flat region (Fig. 4.3a) is shown in Fig. 4.3b. It presents a hyperbolic-shaped behavior of the local density of states near zero bias, which is usual for AB-stacked bilayer graphene [4]. Regions with a similar behavior cover up the largest surface fraction in our sample, in good agreement with the Raman measurements.

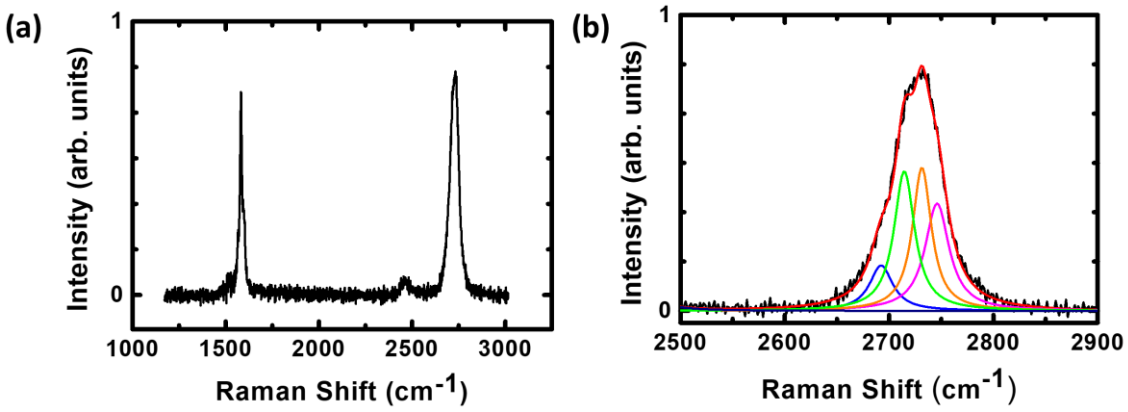

FIG. 4.2 – (a) Raman spectrum of the bilayer graphene on SiC sample. (b) Zoom of the G' peak showing four Lorentzian used to fit the experimental data. This indicates the formation of bilayer graphene films with Bernal stacking.

A careful analysis of the sample also revealed the presence of some regions of coexistence of MLG and BLG, which can be seen in Fig. 4.3c. This was confirmed through tunneling spectra measured at the points marked with blue and red star and shown in Figs. 4.3d and 4.3e, respectively. For the region marked with the blue star one observes the same electronic behavior of the STS presented in Fig. 4.3b, which characterizes a BLG. On the other hand, for the region marked with the red star the STS presents a V-shaped spectrum typical of MLG systems. As one realizes from this experimental observation the MLG is in a higher level when compared to the BLG. This is a consequence of the dynamics of the graphene layers growth on SiC substrates. It is well-known that graphene grows preferentially from the steps. Additionally, the synthesis of the second graphene layer requires three SiC bilayers [153]. It is believed that initially the buffer layer is formed and just afterwards the second layer starts to grow with the thermal decomposition of the SiC underneath the buffer layer. The desorbed Si atoms break the covalent bounds that connect the buffer layer to the substrate converting it into a graphene sheet sp^2 hybridized. The C atoms, on the other hand, reorganize forming a new buffer layer starting at the lower level of the step [154]. This process may continue up to the upper level of the step, but in the case of the region presented here it was interrupted before the complete formation of a BLG. The Raman spectrum indicates, though, that regions like this are minimal considering the size of the sample. Once the hydrogen intercalation is finished the buffer layer is completely detached from the substrate producing regions of BLG (major) and MLG (minor) as presented here.

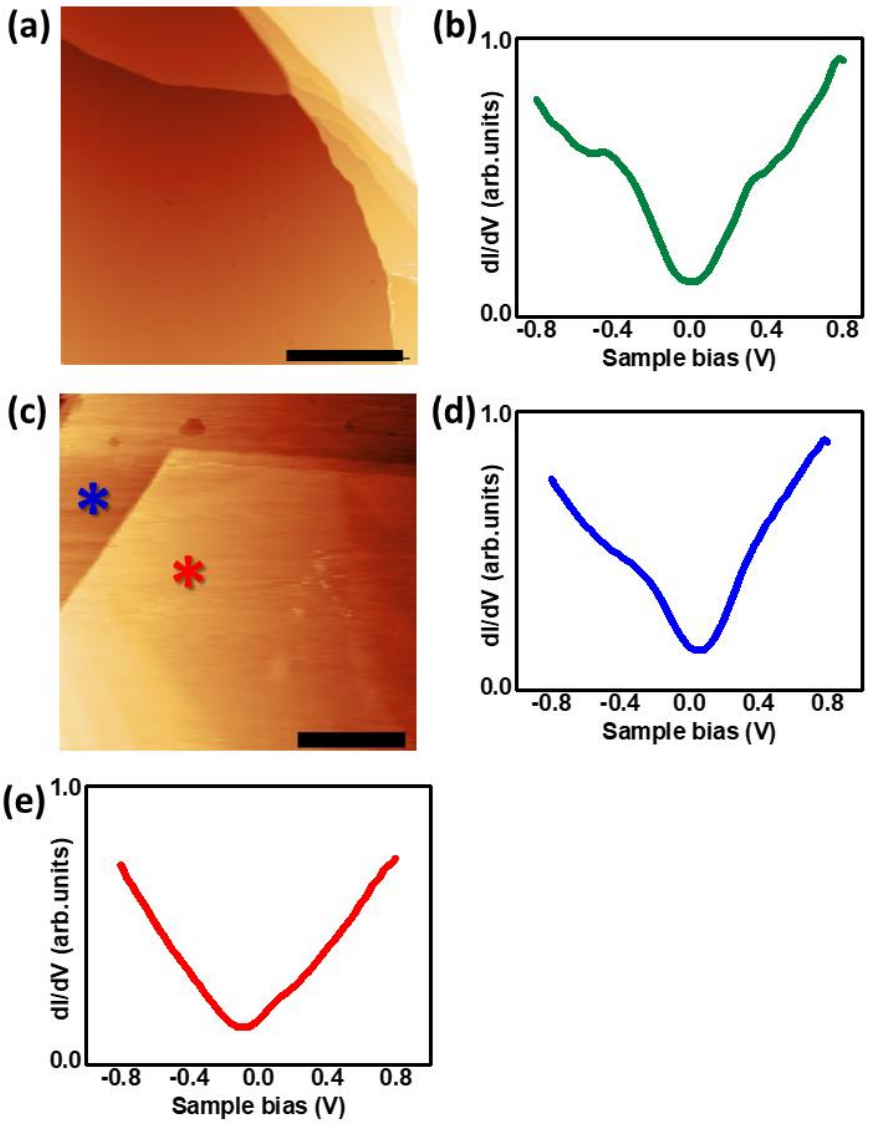

FIG. 4.3 – (a) STM topographic image of the sample after hydrogen intercalation. (b) STS measured at a BLG region. (c) STM image of the sample in a region of coexistence of MLG and BLG. STS measured at the region marked with a (d) blue and (e) red star, i. e. regions with BLG and MLG electronic responses, respectively. The scale bars are (a) 40 nm and (c) 60 nm.

4.3 STACKING FAULTS AND THE FORMATION OF TRIANGULAR GRAPHENE NANOSTRUCTURES

The STM image shown in Fig. 4.3c reveals the presence of shallow nanostructures with a triangular morphology as one sees in the upper left region. A detailed look of the surface shows a region where a number of these triangular nanostructures are seen (Fig. 4.4a). In particular, one observes two distinct types of structures: (i) triangular

nanoplateaus (Fig. 4.4b) and (ii) triangular nanoholes (Fig. 4.4c). These nanostructures, which appear randomly distributed throughout the sample, consist of a number of atomic layers above or below the SiC substrate surface level. Fig. 4.4a also reveals preferential directions for the edges of the nanostructures, following the symmetry of the (0001) surface. For the particular case depicted in Fig. 4.4a the nanoplateau has a rotation of 30° when compared to the triangular nanoholes. High-resolution STM images have also revealed that the triangular graphene nanostructures have well-defined edges. In Fig. 4.4d one observes that there are no discontinuities in the graphene layer (here, the contrast of the STM topographic image was adjusted to highlight the edge of the nanostructure). Additionally, a Bernal stacking pattern is clearly observed for the regions inside and outside these structures (see the blue hexagons shown in Fig. 4.4d), confirming that the substrate is covered by a continuous BLG across the edges of the triangular nanostructures. Fig. 4.4d also indicates that the nanoholes exhibit a zigzag edge termination, rather than armchair.

In order to explain the formation of these nanostructures we propose a scenario where they originate upon the presence of extended defects in the SiC substrate. To understand this more deeply, it is essential to analyze the elementary structure of 6H-SiC. In the left panel of Fig. 4.5a we present a {11-20} view of a 6H-SiC crystal, which is perpendicular to the Si-terminated face (0001). The unit cell is highlighted by the Si atoms drawn in purple and the letters ‘h’ and ‘k’ are related to local hexagonal and cubic vicinities of Si-C bilayers, respectively. Furthermore, the stacking sequence of this structure is indicated in the figure by the characters ABCACB [155]. The 6H-SiC structure represented in the right panel of Fig. 4.5a directly depicts the structure of a stacking fault plane, where the representation plane is normal to the (11-20) direction. Upon the presence of this type of extended defect, adjacent planes establish the configuration drawn in Fig. 4.5b. In this resultant structure, named ‘6H-SiC defect’, one observes the formation of regions of high and low atomic density, which are highlighted by the use of blue and pink colors, respectively.

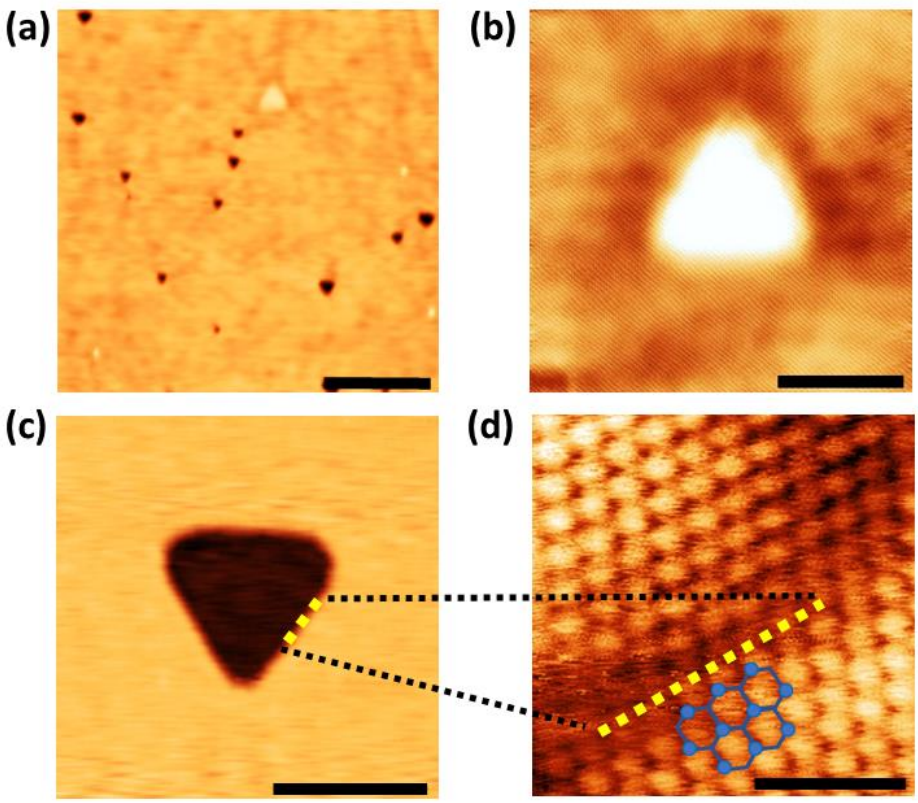

FIG. 4.4 – (a) STM topographic image showing a region with some triangular nanostructures. Two types of structures were observed: (b) triangular nanoplateaus, which builds up above the surface level (c) and triangular nanoholes, which are at a lower topographic level with respect to the surface. (d) Atomically-resolved STM image along the edge of a nanohole showing the continuity of the graphene sheet as well as the zigzag edge termination. The scale bars are: (a) 100 nm, (b) 20 nm, (c) 20nm and (d) 1 nm.

For a crystal in which (11-20) stacking fault planes are present (and cross each other) two main SiC sublimation mechanisms are possible, depending on the out-of-plane distance from the local surface to the high or low atomic density regions that are formed in the vicinity of defects. Whenever the substrate terminates in few bilayers above or exactly in a high atomic density region (but not at a low atomic density region) the area between neighboring defects will be prone to sublimate atoms during the growth process. This is due to the possibility of injecting H atoms into the defect planes during the H-etching procedure, which in turn promotes a release of the atoms located at the high-density regions during the graphitization process. This leads to the formation of seeds that evolve to regular triangular nanoholes after the H-intercalation. As shown in Fig. 4.5b whenever the surface termination is one of those indicated by the dark blue dashed lines, the bilayer graphene fabrication process will generate nanoholes. If the

surface terminates in the atomic layers indicated by the light blue dashed lines the system will locally evolve into nanoplateaus or flat areas. The energetic cost for generating a plateau is slightly higher than the cost of a flat area. Nanoplateaus would then be formed due to the high temperatures involved in the process and local atomic fluctuations.

This qualitative scenario is in agreement with our observations of a large population of nanoholes, in contrast with few observed nanoplateaus (see, e. g., Fig. 4.4a). A schematic view of the process of formation of nanoholes, which takes place if the surface is locally terminated near a high atomic density region is depicted in Fig. 4.5c. Once the growth of graphene layers takes place, the surroundings of the defect-delimitated region form a uniform BLG. Depending on the out-of-plane distance of the high atomic density region the sublimation of the substrate surface will result in nanoholes with different depths (this is compatible with our experimental measurements as discussed in section 4.4 and presented in the right plot of Fig. 4.7b).

Another mechanism takes place if the local surface presents defects, but is terminated exactly in a low atomic density region (as illustrated in Fig. 4.5d). The atoms of the vicinity of (11-20) defects (outside the area delimited by the stacking fault planes) move into this region during the growth process, driving the system locally into a more stable configuration. The proposed migration is possible within the diffusion length of Si and C atoms, which ranges from hundreds of nanometers at 1473 K to tens of micrometers at 1873 K [156]. The result, in this particular case, is the formation of the observed nanoplateaus. In both cases, the graphene formation occurs, covering the nanostructures with the same upper layers.

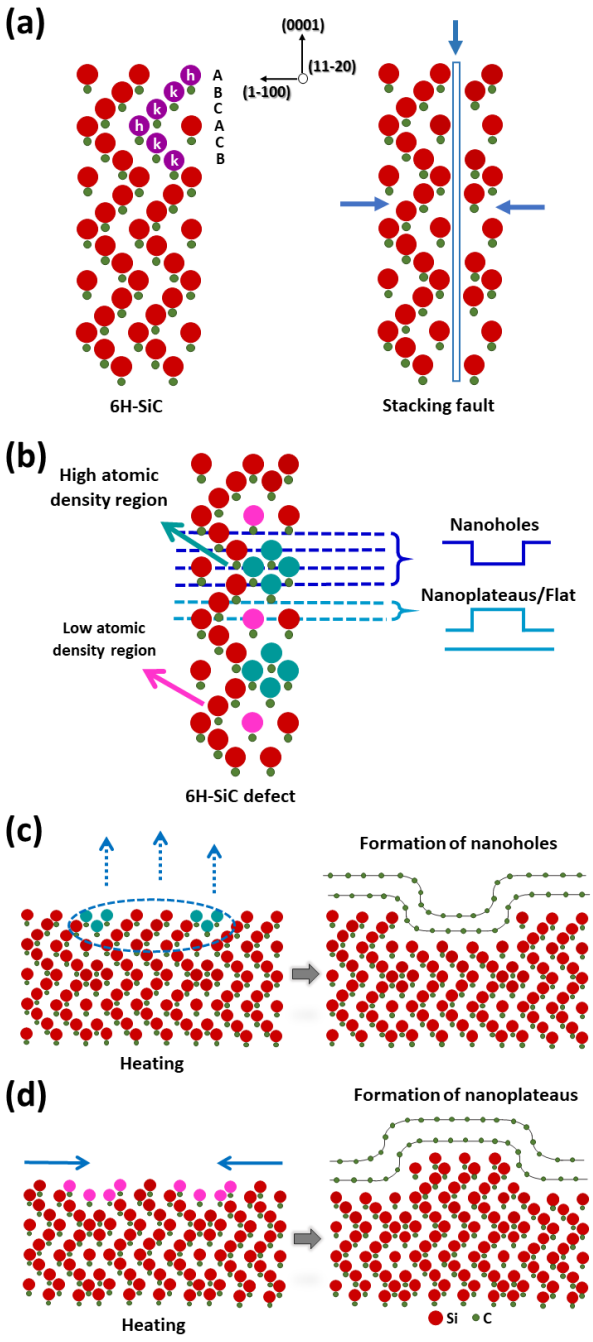

FIG. 4.5 – (a, Left panel) Schematic view of the 6H-SiC crystal structure. The stacking sequence is indicated by the letters A, B and C, while letters 'h' and 'k' are related to local hexagonal and cubic environments, respectively. The Si atoms highlighted in purple indicate the 6H-SiC unit cell. (a, Right panel) Schematic view of the 6H-SiC structure with a stacking fault plane normal to figure plane and propagating along the (11-20) direction. (b) The established configuration, named '6H-SiC defect', presents regions of high and low atomic density, which are highlighted by blue and pink colors, respectively. (c) Whenever the surface terminates in few bilayers above or in a high atomic density region, i. e. positions indicated by the dark blue dashed lines, nanoholes will be formed. (d) If the substrate surface locally terminates in a low atomic density region, represented by the light blue dashed lines, nanoplateaus or flat areas will be formed. Both mechtically represented in figures (c) and (d).

4.4 EXPERIMENTAL EVIDENCES OF STACKING FAULTS

A qualitative X-ray diffraction study was also carried out in order to identify structural changes in the sample prior and after the hydrogen intercalation. Our X-ray measurements were performed at the XRD2 beamline at the Brazilian Synchrotron Light Laboratory (LNLS), Brazil. This beamline delivers 10^{13} photons/second on the sample with an energy of 10.190 keV (wavelength 0.12166 nm). In this experiment a longitudinal (θ-2θ) scan, running along the (00L) crystal truncation rod (CTR) was measured.

In Fig. 4.6 two diffractograms are shown: the black curve refers to the bare 6H-SiC substrate and the gray curve is related to a BLG film on the SiC substrate. In both curves it is possible to observe the CTR of the substrate, including the SiC(00 12) and SiC(00 18) peaks. In addition, the broad humps indicated by the dashed red arrows, shown in the upper curve, are directly related to the formation of the BLG. The other peaks (blue arrows) can be ascribed to extended defects, i. e. stacking faults. These stacking faults, as explained in our phenomenological model, are related to the origin of the triangular nanostructures observed in our system. Besides the growth parameters such as temperature and pressure, which play a role on atom sublimation and surface re-growth kinetics, the density of triangular nanostructures may be directly related to the density of stacking faults. In particular, stacking faults which are observed as broader peaks (arrows marked with a star) are originated from nanometer-sized planes of defects (by Scherrer equation), which are interrupted by the surface. Once the BLG is formed, these peaks present reduced intensity or vanish (see the case of low-angle peaks). This is an indirect indication of the role of stacking faults on the formation of nanostructures.

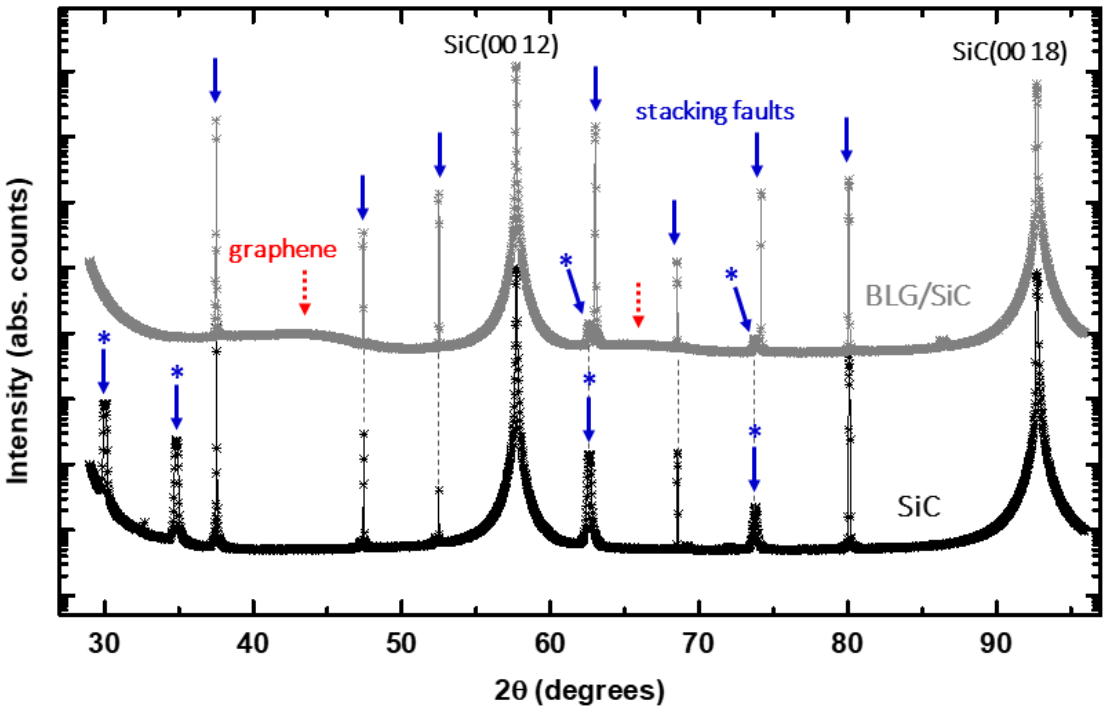

FIG. 4.6 – Longitudinal X-ray diffraction scan along the SiC(00 12) to SiC(00 18) peaks. The black (bottom) and grey (top) curves are related to the bare SiC substrate and the BLG on SiC substrate obtained after H-intercalation, respectively. The dashed red arrows indicate the graphene formation while the solid blue ones indicate the presence of stacking faults. Arrows marked with a star (broad peaks) indicate peaks originated by stacking faults interrupted by the surface (see text). These peaks show reduced intensity or are no longer observed after the BLG formation. Such indirect evidence of stacking fault volume change is related to the formation of nanostructures at the sample surface.

In addition, regions with a high density of structural defects, as depicted in the left panel of Fig. 4.7a, were also observed. In this image one sees a series of planes crossing the surface and forming triangular edges. A magnification of this region (Fig. 4.7a, right panel) evidences a triangular nanohole in the middle of neighboring crossing planes, suggesting that the formation of the observed triangular nanostructures is related to stacking faults in the SiC substrate as previously assumed. The inset sketch represents a triangular nanohole formed among defect planes. The electronic contrast shown in these STM images is due to a higher atomic density at the crossing of defect planes (bright lines), which gives rise to bright areas. They are not related to topographic features, and could not be observed by pure height-sensitive techniques such as atomic force microscopy.

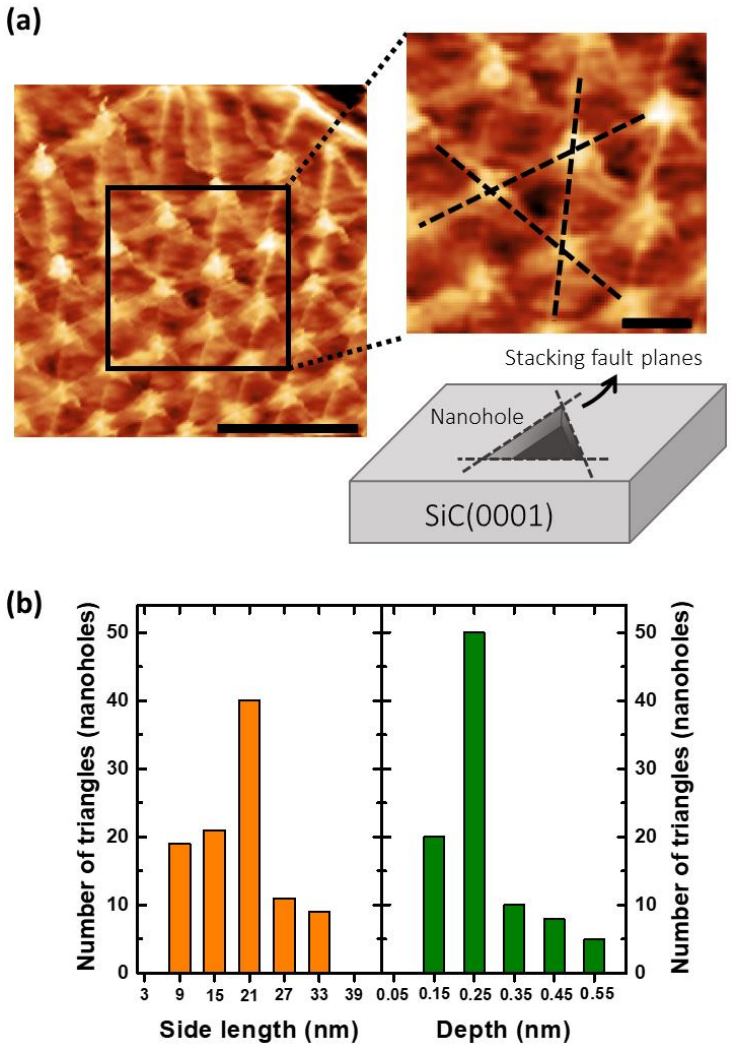

FIG. 4.7 – (a) STM images of a BLG film on SiC showing a region of high density of defects (brighter areas) where one observes the formation of a nanohole. The magnification of this region highlights stacking fault planes crossing in a triangular pattern and the appearance of a nanohole. The inset shows a scheme of the formation of a nanohole among stacking fault planes. (b) Histograms of the (left panel) side length and (right panel) depth distributions over the observed nanoholes. The scale bars are: (a, left panel) 100 nm and (a, right panel) 30nm.

In the histogram presented in the left plot of Fig. 4.7b one sees the size distribution of the investigated ensemble of nanoholes. The average lateral size measured for these structures is (20 ± 1) nm. Each histogram bar represents a total side variation of 6 nm centered at the value displayed in the graph. The nanoholes depths also vary, ranging from 0.13 nm to 0.59 nm. The depth distribution is shown in the right plot of Fig. 4.7b, where each bar has a 0.10 nm width, centered at the values shown in the x-axis. The average nanohole depth is found to be (0.27 ± 0.10) nm, which is centered at

the Si-C bilayers (0001) step width. Considering the low number of nanoplateaus observed – only six – it was not possible to provide histograms. The average lateral width of all nanoplateaus measured is (40 ± 10) nm of side length and (0.28 ± 0.10) nm height.

4.5 SPECTROSCOPIC SIGNATURES OF TRIANGULAR GRAPHENE NANOSTRUCTURES

In order to investigate the electronic behavior of nanoholes and nanoplateaus, tunneling spectra were measured in several triangular nanostructures. Selected STS results are summarized in Fig. 4.8. In all measurements, STS was carried out outside and inside the nanostructures, with some line-scans performed to elucidate electronic conditions along a defined path. In Fig. 4.8a STS were measured at the points marked with a purple circle, i. e. outside the triangular nanohole and at the point marked with a pink circle, i. e. centered in the middle of the nanohole. The two conditions are marked in the STM image of the inset of the tunneling spectra. The spectroscopic responses, shown in Fig. 4.8a, of regions inside and outside the triangular nanohole exhibit exactly the same electronic behavior, similar to the one shown in Fig. 4.3b, and indicate the existence of a simple BLG covering of the triangular nanohole (see Fig. 4.8b).

On the other hand, some nanoholes show an electronic behavior distinct from their vicinity. This is the case of the nanohole shown in Fig. 4.8c. Tunneling spectra acquired along the nanohole (positions of each spectrum are indicated in Fig. 4.8c) show that regions outside this triangle present a BLG electronic signature, while STS measured inside the nanohole exhibit a slightly asymmetrical V-shaped spectra. This dual electronic response can be understood assuming that the bottom layer still has a strong interaction with the substrate for the region inside the nanohole, i. e. MLG + BL covers the triangular region. Such local configuration may be the result of an incomplete hydrogen intercalation, since during this process step it is unlikely that all covalent bonds between the substrate and the buffer layer are broken. This scenario is schematically presented in Fig. 4.8d. Intermediate spectroscopic states were also observed, and depend on the degree of completeness of the hydrogen intercalation process. These scenarios will be further discussed in the following paragraphs.

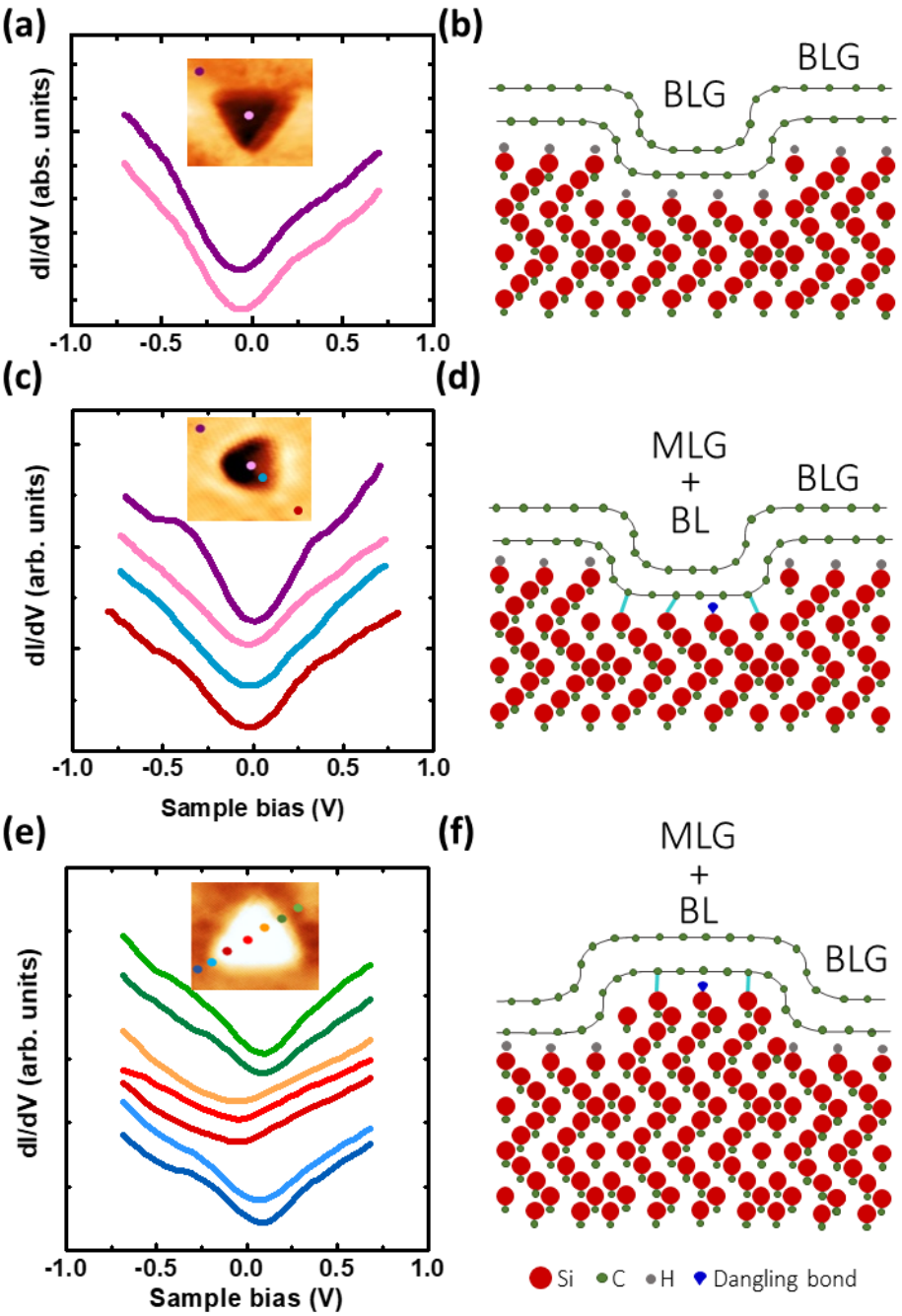

FIG 4.8 – (a) STS measurements carried out inside (pink curve) and outside (purple curve) a nanohole with BLG response (positions indicated at the inset). (b) Sketch of the bilayer configuration related to the spectroscopic measurement. (c) Line-scan with tunneling spectra crossing the nanohole (positions indicated by the color-coded points at the inset). For this nanostructure a V-shaped response is observed inside the triangle (pink and blue curves). (d) Sketch of the local atomic configuration, with some covalent bonds between the buffer layer and the substrate inside the nanohole (MLG + BL scenario). (e) Line-scan with tunneling spectra crossing the nanoplateau (positions indicated by the color-coded points). (f) Representation of the local atomic configuration, with the presence of some covalent bonds. In all figures hyperbolic-like STS are related to BLG while V-shaped spectra indicate a MLG + BL condition.

Finally, the buffer layer interaction with the substrate was also observed for the triangular nanoplateau shown in Fig. 4.8e. This denotes the presence of the MLG + BL configuration. Tunneling spectra measured in a series of points (line-scan) along the nanostructure are presented (positions for each spectrum are shown as an inset in Fig. 4.8e). This STS sequence also evidences a transition between BLG and MLG + BL since a V-shaped spectrum is observed as the tunneling spectra are acquired inside the nanoplateau. This phenomenon is also explained assuming an incomplete intercalation scenario, where a considerable amount of covalent bonds still connects the buffer layer to the substrate (see Fig. 4.8f). The difference between nanoholes and nanoplateaus in this case lies on morphology: the triangular nanoplateau surface placed a number of layers above the substrate height, while the surface of nanoholes lies a number of layers below it.

It is known that the hydrogen intercalation mechanically decouples the graphene from the substrate, releasing the original strain and modifying the electronic interaction between them [130, 157, 158]. The MLG + BL system on top of the SiC substrate is typically n-doped, with a carrier concentration of 4.0 x 10^{12} cm^{-2} [159]. However, after the H-intercalation and generation of the complete BLG, the system becomes p-doped [130, 157, 160] with carrier concentration ranging between 4.0 × 10^{12} cm^{-2} to 1.5 × 10^{13} cm^{-2} depending on the SiC polytype [157]. According to Ristein et al. [160], the p-type doping of graphene after H-intercalation is related to the spontaneous polarization of the SiC. In contrast, the n-type doping of MLG + BL configuration has been attributed to the donor states associated to the BL and its interface with the SiC [160]. Furthermore, this new doping configuration after intercalation is asymmetric for the BLG, i. e. the carrier concentrations of the bottom and top graphene layers are different [130, 157]. Particularly, for the nanoplateau of Fig. 4.8e, regions outside the triangle exhibit STS minima at positive values, corroborating the p-type doping, while inside the triangle the STS minima are slightly shifted towards negative bias.

For nanoholes, a non-deterministic shift of the STS minima was observed for regions inside and outside the triangles, with an approximately equal number of spectra denoting p- and n-type doping of the structure and its vicinity. In Fig. 4.9 one observes shifts in the tunneling spectra denoting p- and n-type doping for the nanoholes that

electronically respond as BLG (Fig. 4.9a) as well as MLG + BL (Fig. 4.9b). Since the H-intercalation provides a well described doping behavior, the observation of such results (arbitrary doping) can be interpreted as an indirect indication of the presence of extended defects, which would act as carrier traps or introduce localized states, changing the local density of states near $V = 0$, probed by STS.

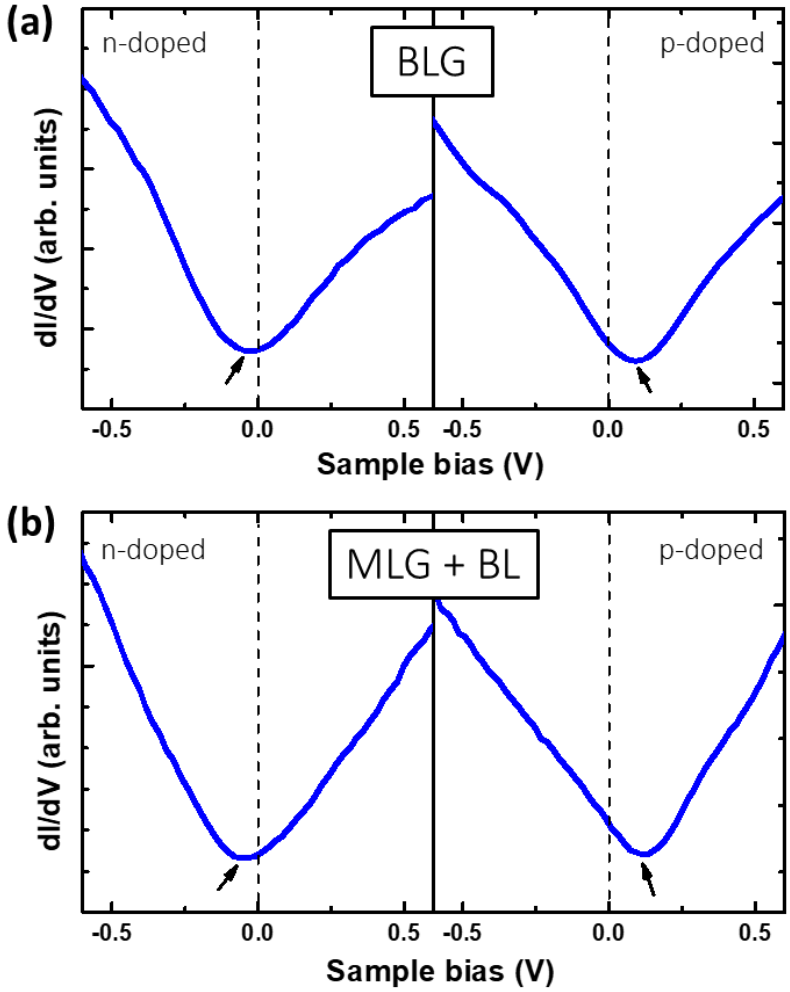

FIG 4.9 – (a) Tunneling spectra of nanoholes that electronic respond as BLG (left plot) with n-type doping and (right plot) p-type doping. (b) Tunneling spectra of nanoholes that electronic respond as MLG + BL (left plot) with n-type doping and (right plot) p-type doping.

Besides our STS results, STM topographic images were also measured for triangular nanoholes varying the tip voltage. Since such images are a combination of topography and local density of states (LDOS), one can map out the electronic occupation of states throughout a given nanostructure. Measurements with distinct tip voltages (specified in each figure panel) for a single nanohole are shown in Fig. 4.10. In such

condition, local topography does not vary, and the differences observed are related to variations in the LDOS. In order to avoid experimental artifacts due to scanning conditions our data analysis was carried out summing forward and backward STM images. The scanning bias conditions are indicated in the tunneling spectra of Fig. 4.10, where BLG, MLG + BL and an intermediate spectrum condition are shown for reference (all them measured inside triangular nanoholes). One notices that, at $V = 300$ mV, where the LDOS of all types of triangles are similar, the color-coded response of STM mapping varies smoothly inside the triangle (Fig. 4.10b). On the other hand, using the condition $V =$ -500 mV, one can obtain the maximum response contrast between regions that behave as BLG and MLG + BL, due to the presence of the hump at the STS measurements of BLG regions. In this condition, the upper left corner of the STM map, shown in Fig. 4.10c, exhibits a region in which we observed a higher LDOS contrast indicating, again, the coexistence of BLG and MLG + BL behavior inside the nanohole. This can also be interpreted as the dual electronic response mentioned above. Therefore, the scenario in which dominant BLG, MLG + BL or intermediate states – with an electronic response whose shape is an averaged combination of BLG and MLG + BL features – are found by STS in the whole population of nano-triangles meets its nanometric counterpart within the nanohole that are mapped such as in Fig. 4.10. The intermediate states measured by STS are, therefore, a superposition of states in the vicinity of the tip position, in which some C atoms of the bottom layer remain partially bonded to the substrate, while others are detached.

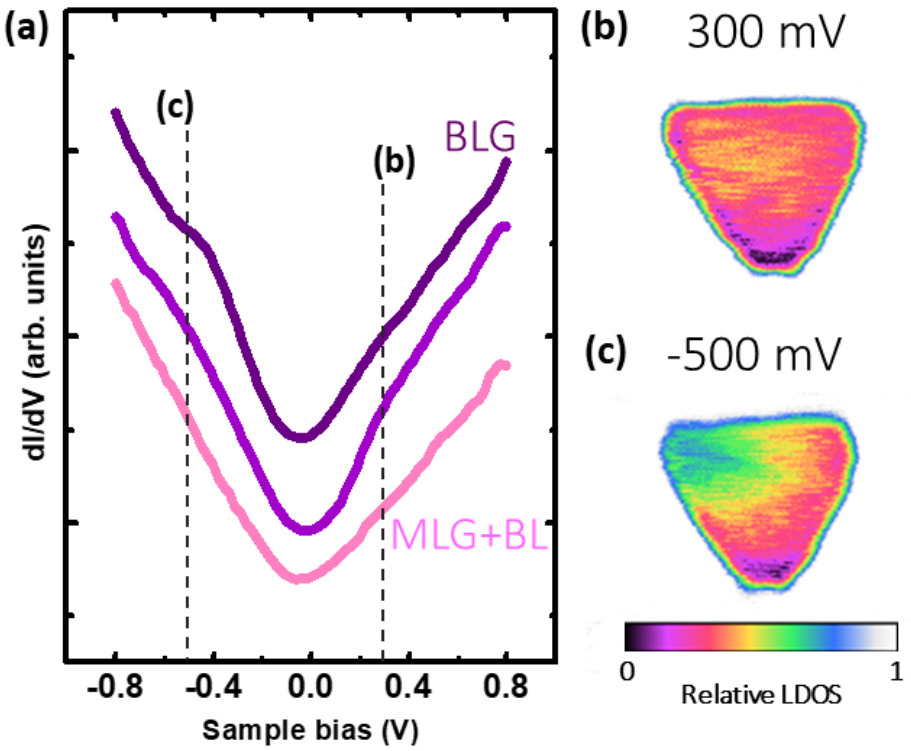

FIG. 4.10 – (a) STS measurements inside distinct nanoholes with three different electronic behaviors, varying among BLG, an intermediate condition and a MLG + BL response. STM measurements of the same nanostructure are presented for distinct bias voltage: (b) 300 mV and (c) -500 mV. For these images the topography remains unchanged and the observed patterns inside the nanostructure are modified due to the LDOS. In panel (b) one observes a more homogenous distribution, which evolves to an asymmetric distribution in panel (c). These different electronic responses evidence intermediate conditions where one observes the coexistence of some regions of BLG and MLG + BL inside the same nanohole. The nanohole side length is 16 nm. The color scale represents a normalized apparent height influenced by LDOS.

4.6 THEORETICAL MODELING

In our theoretical model, which was done in collaboration with M. Pelc, J. González and A. Ayuela (Donostia International Physics Center, Spain), freestanding bilayer graphene with triangular regions of few hundred atoms, interacting with the substrate, was considered. In order to make the system independent of finite effects, translational symmetry was set in armchair direction, keeping the triangles well separated between them. As discussed in chapter II the low energy properties in graphene systems are mainly determined by the π-bands. Thus, in the atomistic calculations shown here a π-band tight-binding Hamiltonian with nearest-neighbor in-

plane interaction was adopted. Bilayer graphene with Bernal stacking consists of two coupled graphene layers shifted with respect to each other. Near the neutrality point, the interlayer coupling was modeled with a single hopping connecting atoms directly on top of each other. In addition, the interaction with the substrate in the triangular region was included in the effective Hamiltonian in three steps: (i) a gate voltage and staggered potential applied to the bottom layer, (ii) lowered intralayer hoppings in the bottom layer, and (iii) lowered intralayer hoppings at the edges of the triangle in both layers. Also, the LDOS was calculated using the Green function matching approach [161-163]. The LDOS in the top layer was averaged in the triangle nodes, integrated over the Brillouin zone and broadened.

Modeling the nanoholes provides further insight on the analysis of our experimental results. Tight-binding simulations were performed in order to study the spectroscopic response of both BLG and triangular nanostructures that interact with the SiC substrate (MLG + BL). Our model structure and morphology are schematically shown in Fig. 4.11a. It consists of two graphene slabs in Bernal stacking, including a triangular region that corresponds to nanoplateaus or nanoholes. Its noteworthy that the results presented here are practically independent of the triangle size. In our model the region around the triangular nanostructures behaves as BLG. In addition, the substrate interaction is taken into account for the triangle in the bottom layer using an effective local potential and smaller hopping values than in pristine bilayer graphene, due to the presence of sp^3 hybridization in some carbon atoms. The STM experiments discussed in section 4.3 show that triangle edges run along the zigzag directions, where the atoms inside the triangle are located up and down with respect to the substrate level at nanoholes and nanoplateaus, respectively. These experimental findings were simulated using a local stretching of the graphene lattice, which was implemented by decreasing the value of the in-plane hopping parameter along the edge of nanostructures.

A sketch of the band structures near the K point for the constituents of the nanostructures, such as the fully detached bilayer graphene (BLG) and substrate-interacting monolayer graphene (MLG + BL) are shown in Fig. 4.11b and 4.11c, respectively. These results agree with reported calculations using density functional theory [164, 165]. As represented in Fig. 4.11b, the band structure of the BLG system is

hyperbolic near the Fermi level. In addition, as a consequence of the interaction with the substrate, the band structure of the MLG + BL system (Fig. 4.11c) consists of linear bands related to the top layer (red) and a nearly flat band (green) that is originated by the bottom (buffer) layer.

By introducing parameters at the area corresponding to the triangular nanostructures layer, resolved LDOS was calculated for the nanohole region. The interaction between the confined states within the MLG + BL triangular region with the surrounding BLG results in the LDOS shown in Fig. 4.11d. As one observes in this figure, the substrate strongly affects the LDOS of the buffer layer.

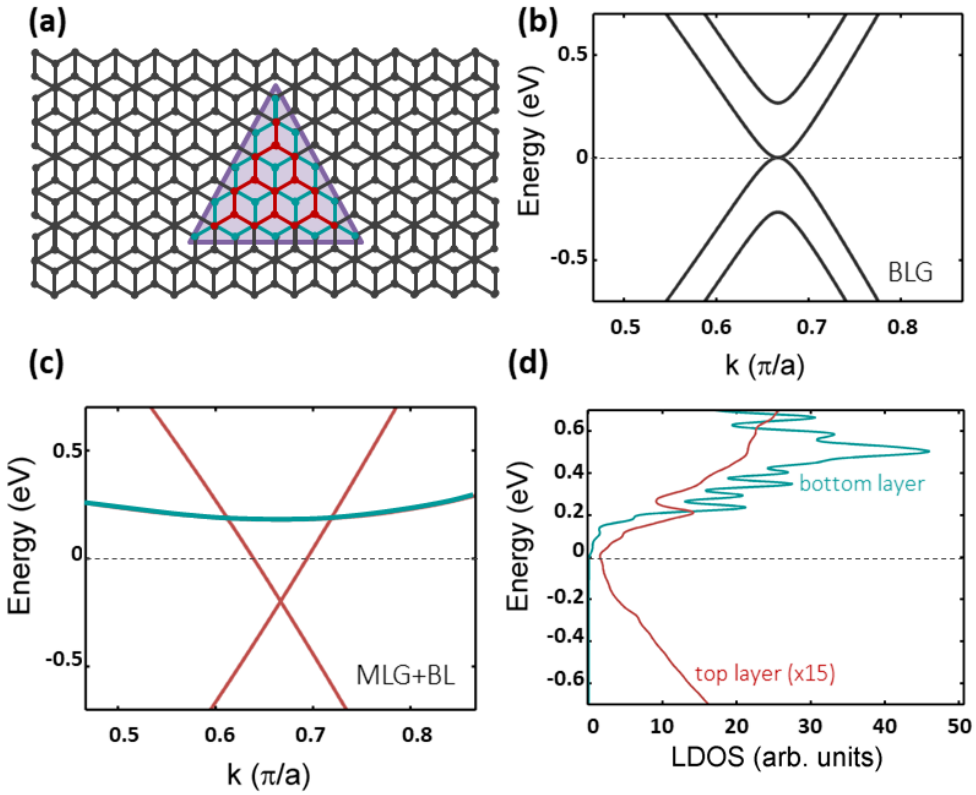

FIG 4.11 – (a) Representation of the model used for simulating STS curves, with a triangular nanostructure (not in scale) inserted into a bilayer graphene slab. Top and bottom layers are represented by red and green atoms, respectively. A sketch of the band structure near the K point is shown in (b) and (c). (b) Band structure for a quasi-free standing (decoupled) BLG. (c) Band structure for a MLG lying on the BL, on top of a SiC substrate. The red and green colors of the bands in (c) refer to the origin of the bands, top and bottom layers, respectively. (d) Layer-resolved local density of states of the nanohole region calculated with our model. The dashed line marks the Fermi level.

Here, the green line displays the LDOS of the buffer layer. As one sees the spectrum is affected by the series of high peaks in the positive energy range. Their origin arises from the quantization of the nearly flat (green) band in Fig. 4.11c when we pattern triangles of nanometer size on the infinite buffer layer. These peaks reflect the presence of strongly confined states within the triangular nanostructure, which is the area where the MLG + BL configuration occurs. The peaks in the buffer layer spectrum reach higher values than the LDOS in the top layer. Thus, to be compared in the same plot, the spectrum of the top layer (shown in red) had to be scaled, here multiplied by 15 times. The LDOS calculated for the top graphene layer preserves the V-shape with the slightly asymmetrical profile (as also shown in detail in the red curve of Fig. 4.12), which is compatible with the experimental STS as shown in Fig. 4.8. This spectrum reflects the fingerprints of the localized peaks from the buffer layer, showing asymmetry in the V-shape and some peaks overimposed. The interplay between the top and the bottom layers in the STS results has a dominance of the top layer electronic structure, with some features added due to the presence of the bottom layer. Since our calculations do not directly scale with the measurement, the correspondence between simulations and the experimental results is qualitative.

As previously stated, experiments measure dI/dV curves, which are mostly related to the LDOS in the top layer of the triangular nanostructures. In Fig. 4.12 we present the LDOS curves for the BLG (black curve) as well as for the triangular nanostructures interacting with the substrate (red curve). As one observes the simulated LDOS of BLG has electron-hole symmetry and shows humps at energies $E = \pm$ 270 meV, which originate from the next energy sub-bands that appear above and below the Fermi energy (included in Fig. 4.11b). This result is consistent with our tunneling spectra measured for flat BLG regions outside triangular nanostructures, which also present inflections and humps for similar energies. The red curve, on the other hand, shows that the LDOS of the top layer of the triangle interacting with the substrate (MLG + BL) has some peaks above the Fermi level overimposed with a monotonically increasing profile for large bias. The typical structure around the humps is affected by the peaks, and presents distinct slopes near $V = 0$. The experimental observation of localized states, however, would only be feasible for measurements at temperatures of the order of 100 mK, given the small

difference of potentials inside and outside nanostructures. Another clear difference between the BLG and MLG + BL is that the bands acquire different slopes (in average), corresponding to different Fermi velocities for carriers, either electrons or holes.

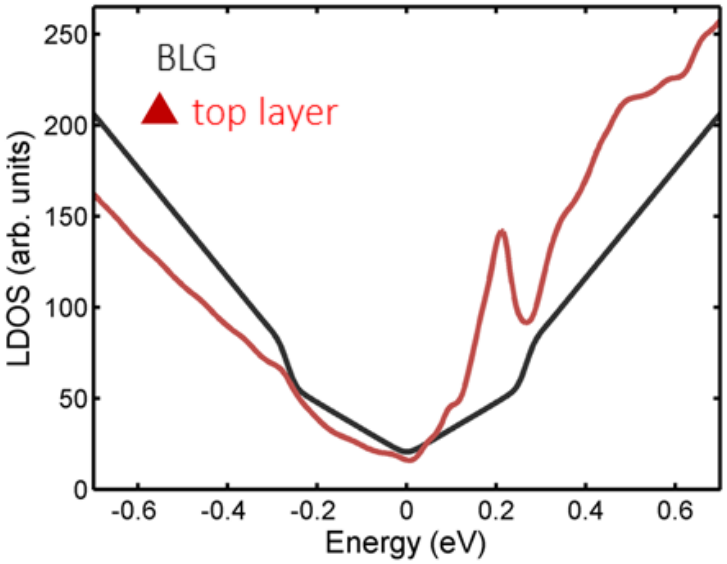

FIG. 4.12 – Total LDOS in top layer of the MLG + BL triangle (red curve) compared to the LDOS of a BLG (black curve).

Finally, the spatial distribution of the LDOS in a triangular nanohole interacting with the substrate was calculated. In Fig. 4.13 simulated LDOS maps in the top layer are shown for selected energy values. All panels show that at zero energy the LDOS is nearly uniform within the triangular area. This trend holds for positive or negative energies if the whole triangle has a homogeneous structural configuration, meaning that it is completely covered by BLG or MLG + BL. For the particular case of a triangle with pure MLG + BL configuration, shown in Fig. 4.13a, the simulated LDOS maps follow the triangle symmetry.

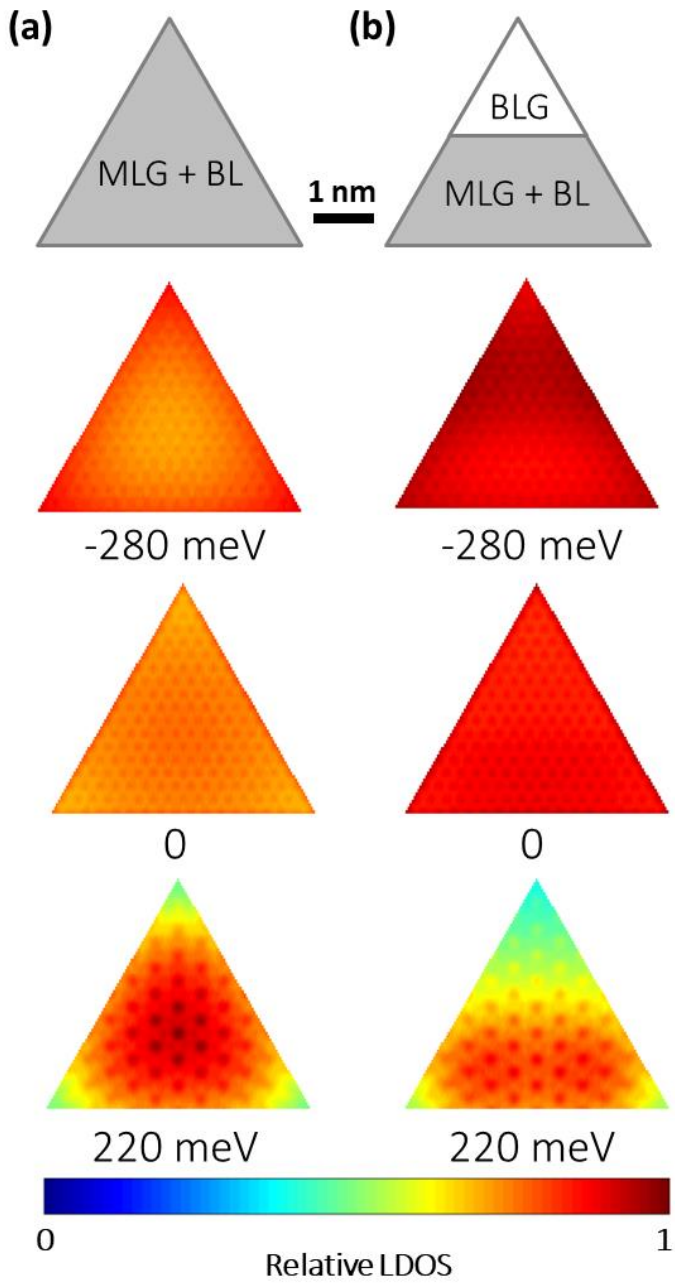

FIG. 4.13 – (a) Spatially distributed LDOS in the top layer for a triangular nanostructure consisting of MLG + BL. (b) The spatial distribution of LDOS is also plotted for a triangular nanostructure consisting of one third of its area of BLG and two thirds of MLG + BL. In these plots the color scale represents the LDOS in arbitrary units for three distinct energies ($E = 0$, -280 meV and 220 meV).

The LDOS in the panels of Fig. 4.13a for $V \neq 0$ for a triangle consisting only of MLG + BL differs from those shown in Fig. 4.13b for a spatially separated coexistence case where BLG and MLG + BL defined regions exist inside the triangle. In our chosen scenario the upper third of the triangle is a BLG, while the lower two-thirds are defined as MLG +

BL. The contrast at the MLG + BL area is due to the asymmetric LDOS profile, being further enhanced in the case of localized LDOS (positive bias). At positive energies the LDOS distribution suffers larger variations because of the states modified due to the buffer layer and its (partial) bonding with the substrate. The simulated data of Fig. 4.13 is in clear correspondence with the STS data and images described in Fig. 4.10. The presence of additional states (peaks) or humps along non-zero energies are the source of changes shown in dI/dV curves, induced by the substrate, which would claim for engineering in the LDOS and band structure within this energy range, following the patterning of nanostructures in BLG.

4.7 CONCLUSIONS

In this work we have employed scanning tunneling microscopy and spectroscopy techniques to investigate structural and electronic properties of individual bilayer graphene nanostructures obtained from SiC substrate sublimation. STM images permitted us to detect the presence of triangular graphene nanostructures that appeared as nanoholes and nanoplateaus. In order to explain the formation of these nanostructures a physical scenario based on (11-20) stacking faults was proposed, resulting in regions of high and low atomic density in the SiC substrate. These extended defects play an important role in the formation of graphene nanostructures since they influence the surface dynamics during the growth process.

Through the analysis of tunneling spectra, we were able to characterize the electronic properties of a number of nanostructures. This revealed distinct electronic responses, spanning from monolayer graphene signatures to bilayer graphene ones. These observations were addressed considering an incomplete hydrogen intercalation scenario in which some regions of the film are still bonded to the substrate. Atomistic calculations were carried out, allowing the understanding of asymmetric STS features.

Considering the production of these nanostructures and their dual electronic response (difference in STS signature for MLG + BL and BLG systems) they could potentially serve as information storage devices, working as a read-only memory units

that could be accessed by an STM/STS instrument. In a scenario where the bonds with substrate are reversible, one would have a read access system of the ultimate minimum size. Therefore, this nanostructured carbon system opens the discussion to atomic scale memory devices in 2D self-assembled materials.

V.

Bi_2:Bi_2Te_3 STACKING INFLUENCE ON THE SURFACE ELECTRONIC RESPONSE OF THE TOPOLOGICAL INSULATOR Bi_4Te_3

In this chapter we report on the successful synthesis of a crystal of the topological insulator Bi_4Te_3 and the study of its surface electronic response. A combination of theoretical and experimental techniques allowed for a systematic study of the composition and electronic properties of the sample. These techniques include density functional theory (DFT), scanning tunneling microscopy and spectroscopy (STM/STS). DFT predicts that distinct surface topological states exist for the two surface terminations of Bi_4Te_3, i. e. Bi_2 and Bi_2Te_3. These terminations are also clearly distinguished in STS measurements, which allow choosing the main conducting channel through a combination of topography and electronic response. We find that the density of states are similar to those of their parent crystals Bi_2 and Bi_2Te_3, albeit shifted in energy. In addition, angle-resolved photoemission spectroscopy (ARPES) measurements highly resemble quintuple-layer terminated Bi_4Te_3 signatures. Constant energy contours also reveal distinct features when directly compared to Bi_2Te_3.

5.1 INTRODUCTION

The discovery of several different types of materials, such as graphene [10], topological insulators [34, 166] and Weyl semimetals [167] (among others) has revolutionized the field of electronic transport. This is due to their unique dispersion relations. From the electronic point of view and as already discussed, graphene exhibits linearly dispersed Dirac cones at the K points in reciprocal space, leading to effective massless conductivity (small dissipation) [3, 10]. Topological insulators, such as Bi_2Se_3 [166] and Bi_2Te_3 [34], exhibit Dirac cones at the Γ point. These topological states are protected by time-reversal symmetry, resulting in spin-protected electronic transport. Weyl semimetals exhibit Fermi arcs connecting gapless states, which have a similar electronic nature [167].

Topological insulators have intrinsic limitations similar to graphene. From the point of view of electronic transport, the most important one is the absence of an electronic gap. This is a serious limitation, since for practical applications the presence of a voltage gap in on/off state is mandatory. In an attempt to introduce such condition, modulated van der Waals lattices have been proposed as a possible solution to overcome this limitation [168, 169]. The prototypical case is Bi_4Se_3 which exhibits a cumbersome electronic band dispersion relation. Bismuth selenide compounds are also extremely temperature sensitive, leading to structural transformations upon annealing [57] and the appearance of bismuth bilayers even close to room temperature. A possible solution to overcome this issue may be bismuth telluride systems, which exhibit a complex bulk electronic structure and are relatively robust upon annealing when compared to other compounds with similar structure and properties, such as Bi_2Se_3 and Sb_2Te_3 [57, 170, 171].

While Bi_2Se_3 exhibits an isolated Dirac cone, Bi_2Te_3 presents one that is nested inside a bulk M state in a limited energy range of nearly 200 meV below the Fermi level [34]. Electronic densities of states with a linear dispersion have been measured in a considerable electronic range for Bi_2Te_3, although not at the Dirac point for the case of nanoplatelets [172].

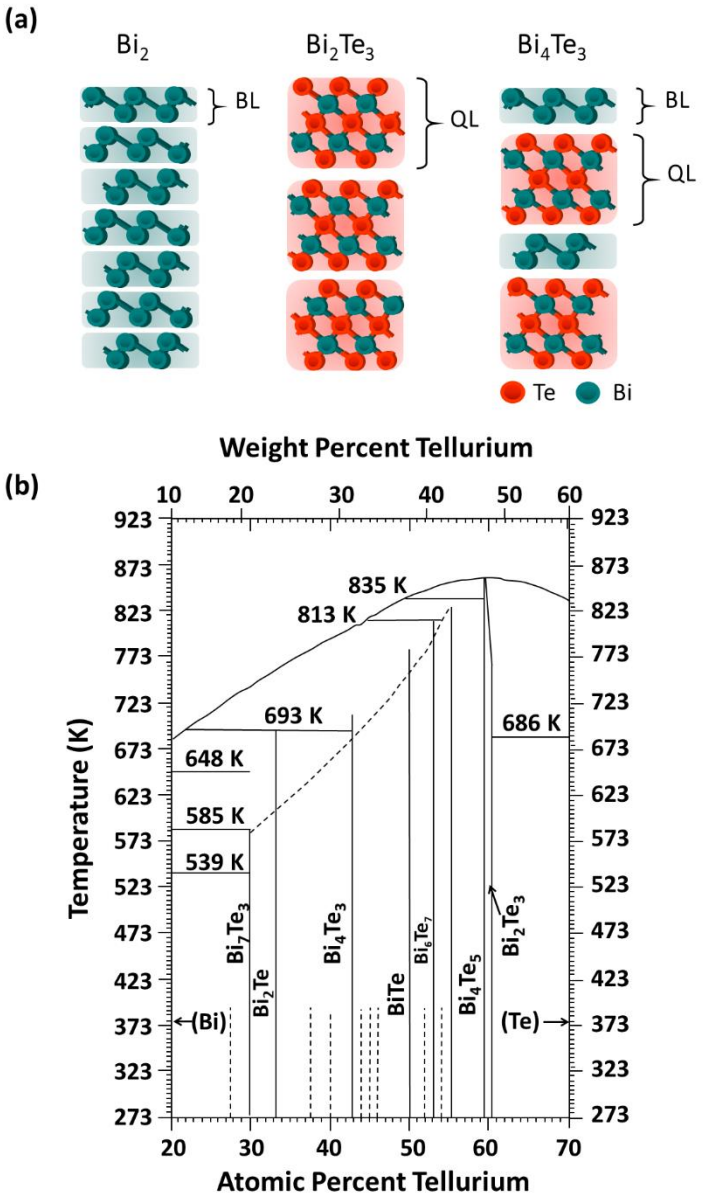

FIG. 5.1 – (a) Atomic structure of Bi_2, Bi_2Te_3 and Bi_4Te_3. Bi_4Te_3 is the first of an infinitely adaptive series of Bi_2-Bi_2Te_3 combinations. (b) Phase diagram of Bi-Te systems showing several possible Bi-Te compounds. Bi_4Te_3 is only obtained in a narrow chemical concentration window in between 33% and 43% of Te (phase diagram adapted from reference [173]).

Similar to Bi_4Se_3, Bi_4Te_3 is a strong topological insulator composed of bismuth bilayers (Bi_2), here referred as BL and quintuple-layers (Bi_2Te_3) or simply QL, both stacked along the (111) direction and bonded by van der Waals interactions [169] (see Fig. 5.1a). The unit cell of this material is composed of three complete stacks of BL + QL [173]. Bi_4Te_3 is the first of an infinitely adaptive series of BL-QL combinations forming different

compounds of type $(Bi_2)_m(Bi_2Te_3)_n$ (see Fig. 5.1a) [174]. As a consequence of its structural configuration, Bi_4Te_3 may present different types of terminations on its surface, i. e. the quintuple-layer termination and the Bi-bilayer termination (its simple exfoliation explains why these two conducting channels were extensively observed by a number of groups in different sorts of topological insulators, with a similar structure, such as Bi_4Se_3 [168, 169]). In addition, both terminations were also observed for topological insulators only formed by quintuple-layers such as Bi_2Te_3 [56] and Bi_2Se_3 [175]. Several methods, from hydrogen etching treatments to sputtering/annealing cycles [176], have been developed to stabilize Bi-bilayers on top of different topological insulators as an attempt to study the topological properties of these systems.

In this chapter we present both theoretical and experimental studies of Bi_4Te_3, which was synthetized here using the Bridgman method, following the growth parameters indicated in the phase diagram of Bi-Te compounds, as presented in Fig. 5.1b. The synthesis of this material was investigated using powder X-ray diffraction of the as-grown samples, which revealed the formation Bi_4Te_3 and other minor phases. In order to understand the electronic properties of Bi_4Te_3, we have first performed an in-depth theoretical analysis of the band structure and electronic density of states of this material using density functional theory (DFT). A study of Bi_2 and Bi_2Te_3 was also necessary for the correct interpretation of our experimental findings. In addition, we have employed scanning tunneling microscopy and spectroscopy (STM/STS) to characterize the structural and electronic properties of Bi_4Te_3. The analysis of height-profiles of the STM topographic images together with the tunneling spectra measured in different regions of the sample allowed us to identify bilayer- and quintuple-layer-terminated regions of Bi_4Te_3 as well as regions of stacked layers of Bi_2 and Bi_2Te_3. Angle-resolved photoemission spectroscopy measurements combined with DFT calculations indicate that the main contributions from the surface are from Bi_4Te_3 terminated in quintuple-layer. Constant energy contours also reveal a highly warped Fermi surface with a hexagonal shape that resembles a snowflake with more elongated and ‘gapped’ branches when compared to Bi_2Te_3.

5.2 THEORETICAL ANALYSIS OF THE ELECTRONIC STRUCTURE OF Bi_4Te_3 AND ITS CONSTITUENTS

A first step towards the surface characterization consists in the determination of the electronic signatures of distinct terminations of Bi-Te phases that may coexist in our sample. For this purpose, DFT calculations [177,178] were carried out in collaboration with M. S. C. Mazzoni and G. A. S. Ribeiro (UFMG, Brazil). These results allowed us to map, for each structural model, the surface contribution to the low-energy electronic states. Also, the determination of the projected density of states (PDOS) is a valuable tool to be used in connection with STS measurements. The methodology employed was based on the OpenMX implementation [179] which employs full-relativistic pseudopotentials [180], a basis set composed of localized pseudoatomic orbitals [181] and the generalized gradient approximation [182] to represent the exchange-correlation functional. An energy cutoff of 160 Ry was used in the wave function expansions, and an 8x8x1 Monkhorst-Pack K-point mesh to sample the Brillouin zone was employed [183]. To achieve convergence in the PDOS calculations, a denser k-point grid was required – a 16x16x1 one was used. Periodic boundary conditions with at least 1.0 nm vacuum distance between images in the non-periodic direction were imposed.

In order to investigate different Bi_4Te_3 terminations, slab models were built based on experimental atomic positions [184] and comprising 40 (six QL + five BL) and 37 atoms (five QL + six BL) for the quintuple-layer (Bi_4Te_3: QL) and Bi-bilayer (Bi_4Te_3: BL) terminations, respectively. Fig. 5.2 presents the calculated band structures along the M-Γ-K path in the first Brillouin zone for these two terminations. The size of the red circles in these plots indicates the contribution from the surface layer, which in our case consists only of a single atomic layer.

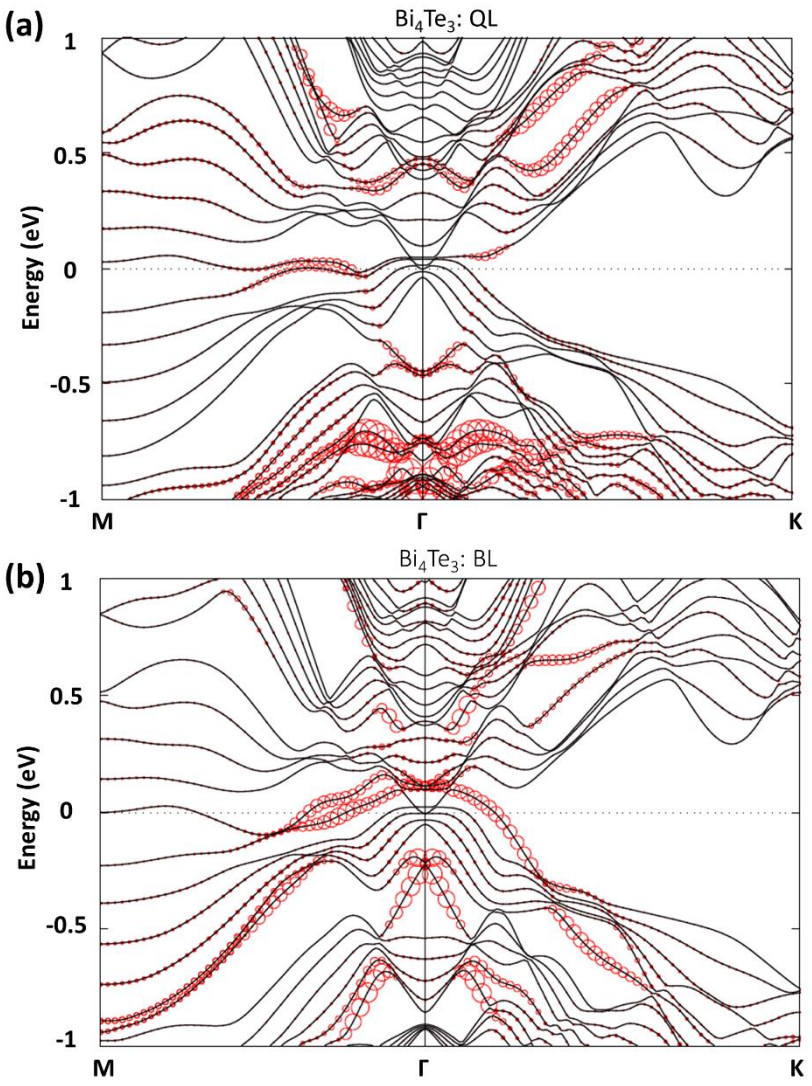

FIG. 5.2 – DFT electronic band structures for Bi_4Te_3. (a) QL-terminated Bi_4Te_3 and (b) Bi-bilayer-terminated Bi_4Te_3. Red circles indicate surface states, and their size measures the degree of surface localization.

An electronic gap at the K point is a common feature in these two band structures. However, there are important differences in other regions of the Brillouin zone. For instance, the two Bi_4Te_3 terminations may be distinguished by the character of surface states in the vicinity of the Γ point. Indeed, an 'inverted-valley'-shaped band around -0.45 eV characterizes the QL-termination (Fig. 5.2a), whereas the BL-terminated structure (Fig. 5.2b) presents an inverted V-shaped band around -0.2 eV on top of which a surface M-shaped band can be seen (the combination of these states represents a crossing similar to an 'X'). These results are resembling to the findings concerning the

related compound Bi_4Se_3 [168, 169]. In the latter, the 'X' and the 'valley', observed in ARPES experiments, are the key ingredients to differentiate between Te- and Bi-rich terminations. Also, there are important differences in the unoccupied region of the spectra: in the QL-terminated structure, two parabolic surface states (concave down) are located at ~0.4 eV, while in the BL-terminated case flat and parabolic (concave up) surface bands can be seen at ~0.1 eV.

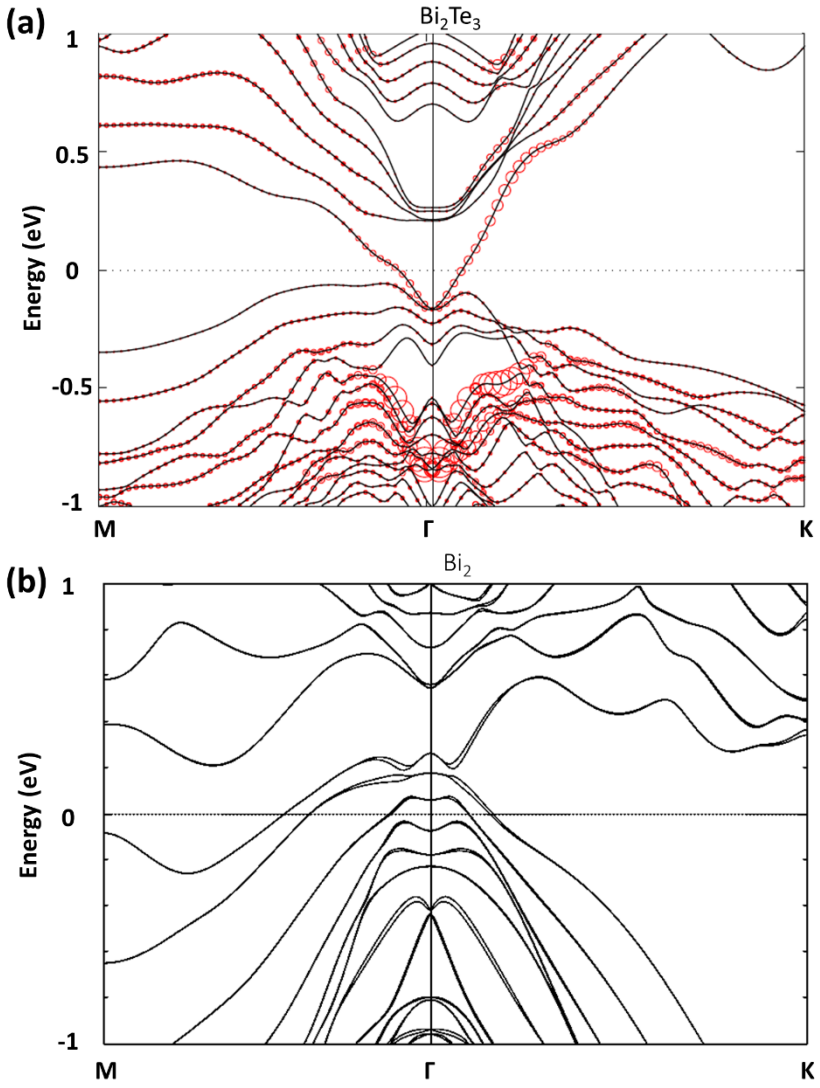

FIG. 5.3 – DFT electronic band structures for (a) Bi_2Te_3 and (b) Bi_2. Red circles in (a) indicate surface states; their size measures the degree of surface localization.

In Fig. 5.3 the band structure structures along the M-Γ-K path in the first Brillouin zone of Bi_2Te_3 (Fig. 5.3a) and Bi_2 (Fig. 5.3b) are shown for reference. These theoretical results were calculated comprising 5 QLs and 6 BLs, respectively. Here, as in the previous

calculation, the red circles in panel 5.3a indicate the surface states. Such calculation was not done for Bi_2. There are significant differences between these two structures: Bi_2Te_3 presents, for instance, a Dirac cone at the region of the Γ point, which is absent in the band structure of Bi_2. Also, Bi_2Te_3 has a series of concave down bands above 0.6 eV in the vicinity of the Γ point, while Bi_2 presents two bands around 0.55 eV with an approximately V-shape. Furthermore, Bi_2Te_3 has some nearly flat bands at 0.21 eV.

5.3 SAMPLE GROWTH AND X-RAY CHARACTERIZATION

Bi_4Te_3 samples investigated in this work were synthesized through the Bridgman method, mixing Bi and Te elements according to the molar proportions and temperatures of the phase diagram of Bi-Te systems shown in Fig. 5.1b. As one sees in the simplified phase diagram, the compositional window of synthesis of Bi_4Te_3 is rather small, in other words, it is obtained only in a chemical concentration window between 33% to 43% of tellurium. The as-grown samples investigated here were prepared in a furnace using bulk bismuth and tellurium spheres (1 mm diameter 99.999%). These spheres were encapsulated in an evacuated quartz tube (base pressure of 10^{-5} mbar). Afterwards, this quartz tube was inserted in the furnace where the temperature could be controlled and constantly monitored. In particular, for the sample investigated here, the temperature was ramped up from 300 K to 1023 K. The melted substance was kept in this temperature for 24 hours. Then, the system was cooled down, reaching room temperature after 7 hours. These procedures gave rise to a number of pieces of highly oriented Bi_4Te_3 crystals, which were freshly cleaved in situ (pressure of 5.0×10^{-8} mbar) using scotch tape before STM/STS measurements. In addition, no change was observed in pressure during the cleavage of the sample. Such a fact indicates that this procedure did not introduced any contamination in the investigated system.

Powder X-ray diffraction measurements using Cu-K_α radiation (0.15406 nm) were utilized to identify the composition of the as-grown samples (see Fig. 5.4). Initial samples made at 4:3 molar proportions gave rise to Bi_4Te_3 and Bi_2Te_3 coexisting together as depicted in Fig. 5.4a. In this figure the Bi_2Te_3 peaks can be identified among the Bi_4Te_3 phase (see the inset of Fig. 5.4a). Further attempts to grow pure Bi_4Te_3 were made

increasing the quantity of Bi, i. e. an off-stoichiometric molar proportion was used, always taking into account the phase diagram of this system (Fig. 5.1b). This procedure resulted in the coexistence of Bi_4Te_3 (major phase) and Bi_2 (minor phase) as one sees in Fig. 5.4b. In the inset of this figure one can observe intense peaks at low angles, which allowed us to confirm the coexistence of these two different phases.

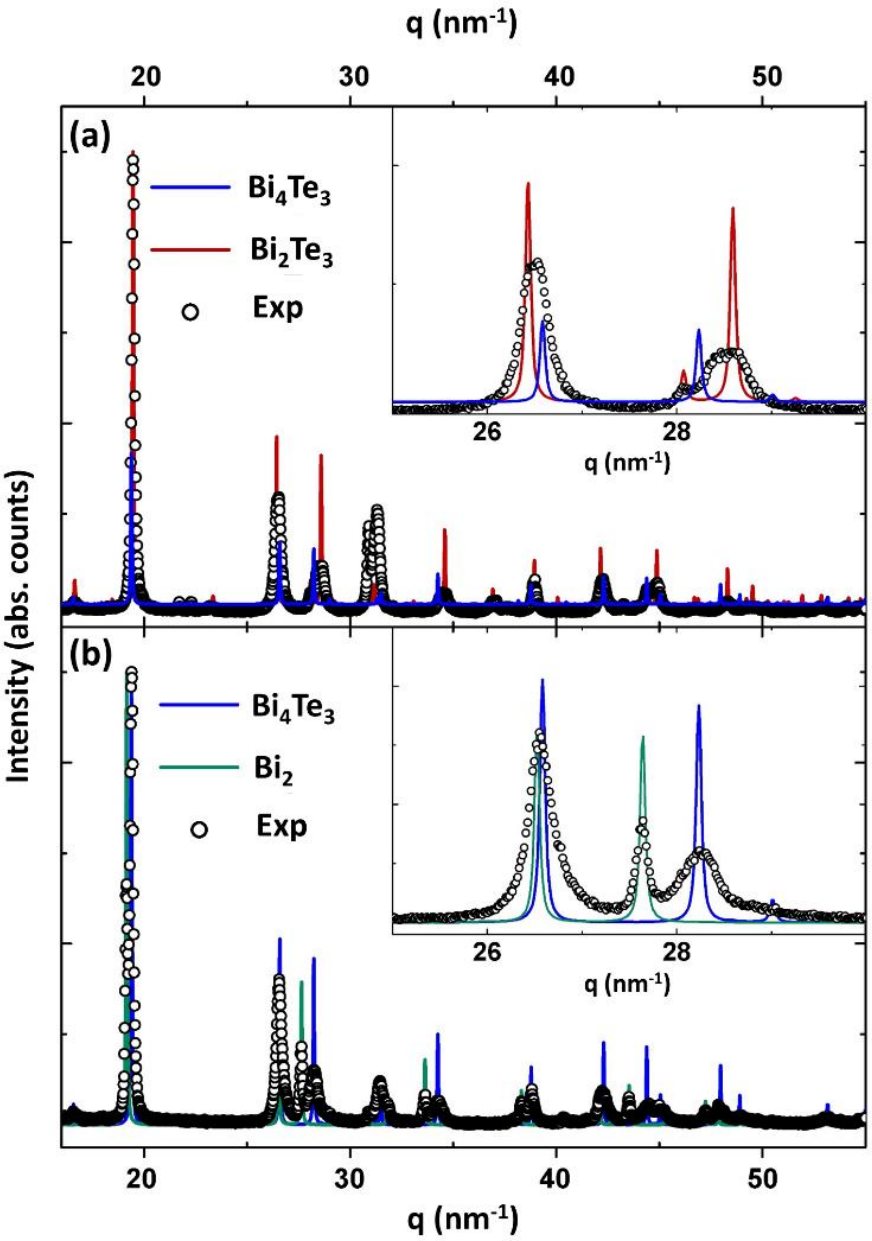

FIG. 5.4 – Selected powder X-ray diffraction pattern of the as-grown samples showing the coexistence of (a) Bi_4Te_3 and Bi_2Te_3 as well as (b) Bi_4Te_3 and Bi_2.

These results demonstrate that attempts to grow pure Bi_4Te_3 usually result in Bi_4Te_3 coexisting with phases. The determination of phases as major or minor was done using commercial peak-search algorithms, which match the overall peak area for the whole diffractogram. This is the reason why some fitted peaks are more intense in this figure, meaning that the percentage of the relate compound is higher (the crystallographic algorithm correctly matches peak areas instead of intensities). Due to strong texturization effects on exfoliated crystals the determination of phase content demands a number of θ-2θ scans on samples prepared by distinct methods and geometries, providing a broad sampling over possible texturizations. For the system studied here, the averaged values, obtained with the use of algorithms, taken into account different scans, are: (64 ± 2)% of Bi_4Te_3, (28 ± 3)% of Bi_2 and (8 ± 2)% of Bi_2Te_3. This last (minor) phase is observed as weak peaks in some of the scans. These observations show that this material does have some local variations in chemical composition, which may lead to technological limitations. In our case it permitted us to study and characterize these distinct Bi-Te phases and obtain a deeper understanding of their electronic properties. Multi-phase systems of other topological insulators have been reported in literature. Gonçalves et al. [57] investigated, using X-ray diffraction and STM techniques, transformations in a Bi_2Se_3 sample upon controlled heating up to 623 K. This study revealed the coexistence of the major Bi_2Se_3 phase together with Bi_4Se_5 and BiSe, which appear as hexagonal grains embedded in the Bi_2Se_3 matrix. Thus, the coexistence of multiple phases within the same sample permits to combine different types of topological insulators and investigate both their individual properties as well as the properties that arise from their interaction with each other.

5.4 SCANNING TUNNELING MICROSCOPY AND SPECTROSCOPY RESULTS

An STM/STS analysis allowed for a detailed characterization of our sample and the observation of different domains as well as the study of their electronic responses. All the STM measurements presented in this chapter were obtained using an Omicron-VT STM microscope (UFMG, Brazil) operating either at room temperature or at low temperature

(25 K) in constant-current mode and ultra-high vacuum conditions (7.0×10^{-11} mbar). STS measurements presented here were acquired using a lock-in amplifier operating in a frequency of 3.01 kHz and a modulation amplitude of 10-20 mV. For all the tunneling spectra shown here the reproducibility of the measurements was considered.

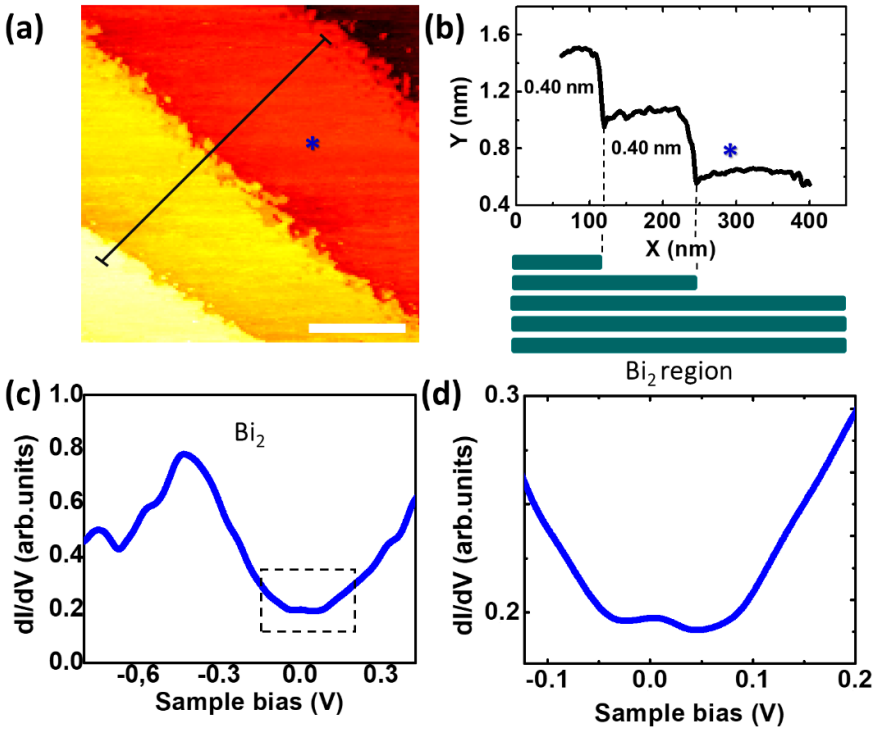

FIG. 5.5 – (a) STM topographic image of a Bi_2 domain of the sample. (b, Upper panel) Height-profile along the black line depicted in (a) showing steps of (0.40 ± 0.09) nm, which is compatible with the height of Bi-bilayers. (b, Lower panel) A scheme of the configuration of this domain showing a number of Bi-bilayers (blue blocks) stacked forming a Bi_2 region. (c) Tunneling spectrum measured at the blue star shown in (a). (d) Zoom of the tunneling spectrum in the low energy range of the black dashed rectangle shown in (c). The scale bar is 110 nm. Measured at 25 K.

Fig. 5.5a presents a region with a series of terraces with approximately 120 nm width. The profile indicated by the black line crossing the steps along this region is shown in Fig. 5.5b (upper panel). In this height-profile, one observes a number of terraces separated by steps of (0.40 ± 0.09) nm height. This indicates the stacking of a series of Bi-bilayers (BL), forming a Bi_2 region [56] (see the scheme of this configuration presented in the lower panel of Fig. 5.5b). One also observes that the step edges in this region are very fuzzy and rough. However, since only mechanical exfoliation (cleavage) was carried out prior to STM, the reason for this remains unclear. In Fig. 5.5c one observes the

spectroscopic signature, which is proportional to the local density of states (LDOS) of the sample, for the region marked with the blue star. In particular, we highlight the conductive behavior of the local density of states. Additionally, a zoom of the tunneling spectrum in the region inside the black dashed rectangle in Fig. 5.5c is shown in panel 5.5d. The electronic signature of this material consists of a very broad shoulder at the Fermi level. Similar features were also observed by Yang et al. [185], who investigated edge states in single Bi(111) islands on top of Bi_2Te_3.

By analyzing other regions of our sample with a combination of STM/STS techniques, we were able to identify distinct surface terminations of Bi_4Te_3. An example is given in Fig. 5.6a, which presents an STM topographic image of a region of coexistence of Bi_4Te_3 and Bi_2Te_3 domains, as we shall show. A careful analysis of this region shows the presence of a grain boundary indicated by the dashed gray line and the gray arrows in the figure. The height-profile along the black line is presented in the upper panel of Fig. 5.6b. It exhibits a series of steps of different heights that, together with STS signatures, allows for the identification of distinct phases and terminations. The terraces located on the left-hand side of the grain boundary, indicated by green and red stars, are separated by a step of (2.40 ± 0.09) nm, which is consistent with the stacking of two quintuple-layers and a Bi-bilayer. This corresponds to the Bi_4Te_3 configuration as shown in the scheme presented in lower panel of Fig. 5.6b. In addition, this scenario points out necessarily to two types of terminations: the region marked with a green star is ascribed to Bi_4Te_3 with a Bi-bilayer termination (Bi_4Te_3: BL), while the terrace marked with a red star presents a quintuple-layer termination (Bi_4Te_3: QL).

For the terraces shown in the middle (labeled with a purple star) and in the right upper corner of Fig. 5.6a, the step heights are of (1.00 ± 0.09) nm. This is indicated in the line profile shown in Fig. 5.6b (upper panel). This indicates a sequence of QLs stacked one on top of the other [172], and it is compatible with the description of the Bi_2Te_3 phase (see sketch in Fig. 5.6b, lower panel).

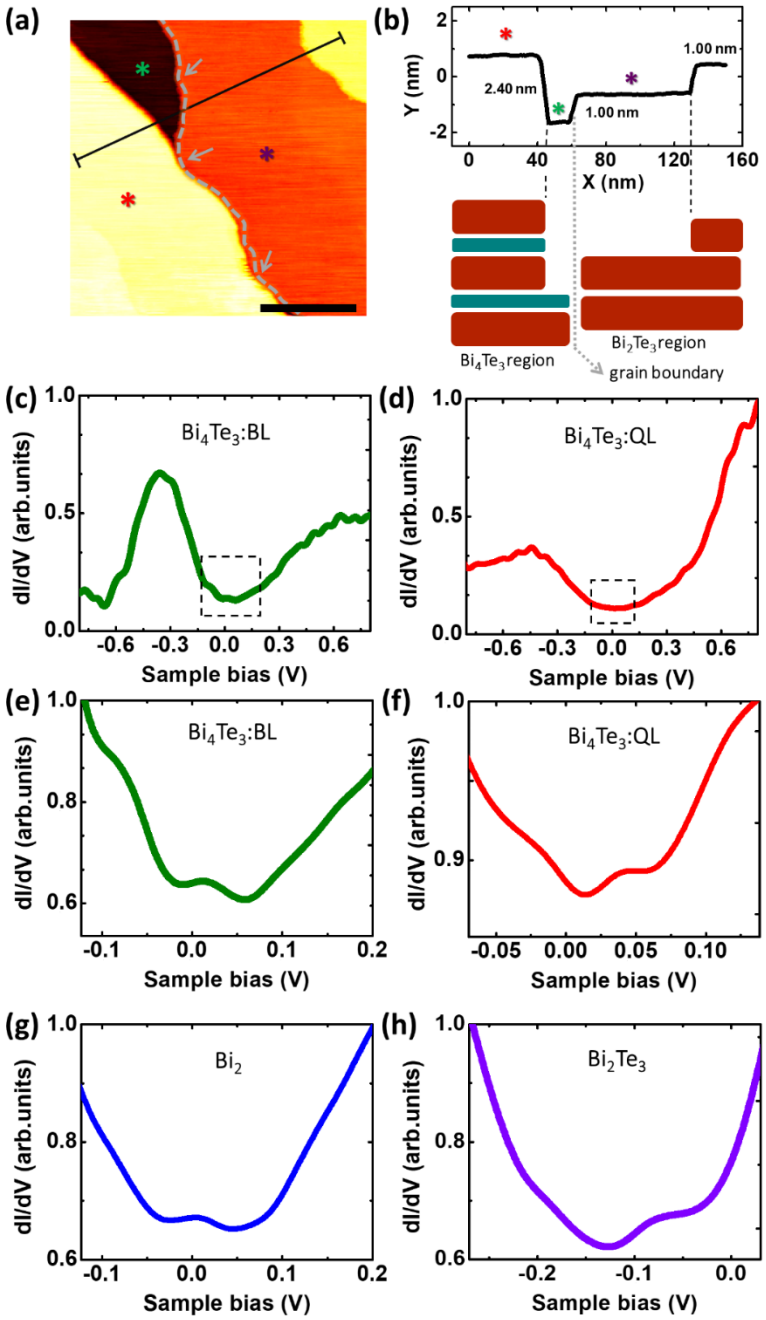

FIG. 5.6 – STM topographic image of a region of coexistence of a Bi_4Te_3 domain and a Bi_2Te_3 domain. (b, Upper panel) Height-profile along the black line depicted in (a) showing a step of (2.40 ± 0.09) nm, compatible with the height of QL and BL, and steps of (1.00 ± 0.09) nm, befitting with the stacking of QL only. (b, Lower panel) Scheme of the configuration of these two domains showing Bi_4Te_3 and Bi_2Te_3 regions separated by a grain boundary. The blue blocks refer to Bi-bilayers and the red ones refer to quintuple-layers. Tunneling spectra measured at Bi_4Te_3 region, i. e. at the (c) green and (d) red star shown in (a). These STS measurements refer to Bi_4Te_3: BL and Bi_4Te_3: QL, respectively. (e) Zoom of the tunneling spectrum in the low energy range of the black dashed square shown in (c). (f) Zoom of the tunneling spectrum in the low energy range of the black dashed square shown in (d). (g) STS measured at a Bi_2 region. (h) STS measured at Bi_2Te_3 region, i. e. at the purple star shown in (a). The scale bar is 60 nm. Measured at 300 K.

Scanning tunneling spectra were measured for each of these regions marked in the STM image presented in Fig. 5.6a. For the regions identified as Bi_4Te_3: BL and Bi_4Te_3: QL the STS are shown in Figs. 5.6c and 5.6d, respectively. In addition, in Figs. 5.6e and 5.6f a zoom of the tunneling spectra for both regions inside the black dashed squares, depicted in Figs. 5.6c and 5.6d, is shown. The STS response presented in Fig. 5.6e for the Bi-bilayer-terminated Bi_4Te_3 region has strong similarities in the low energy range with the STS of the Bi_2 region (both of them present a very broad shoulder at the Fermi level), reproduced again here in Fig. 5.6g. This indicates a strong contribution of the topmost (surface) layers to the tunneling spectrum.

Tunneling spectra of the terrace labeled with a purple star, i. e. the region ascribed to the surface of Bi_2Te_3 is presented in Fig. 5.6h. This LDOS profile is compatible with others studies of Bi_2Te_3 presented in literature [34, 172], confirming our proposed model. Through this STS measurement one can obtain the energy of the Dirac point through the projection of the Dirac cone to its intersection with the zero-conductance point, i. e. the point in which the density of states is zero [186, 187]. This is because the Dirac cone is not directly exposed in this system, but on the contrary, it is wrapped in bulk bands of the material. For this particular region of the sample, we found that the energy of the Dirac point is -462 meV (obtained by a linear regression), which indicates a n-type doping [26]. In this case also, we observed similar features in the STS responses for the regions with quintuple-layer terminations, i. e. Bi_4Te_3: QL (Fig. 5.6f) and Bi_2Te_3 (Fig. 5.6h).

To further confirm the surface termination assignment, the LDOS, which can be directly compared to the experimental tunneling spectra under the assumption that both the tip density of states and the tunneling matrix elements are constants, was computed using our DFT results. Since the tunneling current is expected to decrease exponentially with the distance from the surface, the density of states was projected in all cases only on the two upper surfaces. The Fermi level is set to zero. A comparison among our theoretical results (see Fig. 5.7) and the tunneling spectra (Fig. 5.6) suggests that our samples should be highly n-doped. One possible origin of such doping is the existence of interfaces, vacancies and antisites defects which are known to n-dope Bi_2Te_3. In fact, we have focused on the energy range that best fitted the STS curves. Thus, we have found that it should be ~0.2-0.4 eV above the Fermi level in the calculation (the energy scale in

the tunneling spectra refers to a distinct reference). Also, the QL- and BL-terminated Bi_4Te_3 retain most of features of the pure Bi_2Te_3 and Bi_2 structures, respectively, which agrees with the experimental results and allows for the distinction of the two terminations.

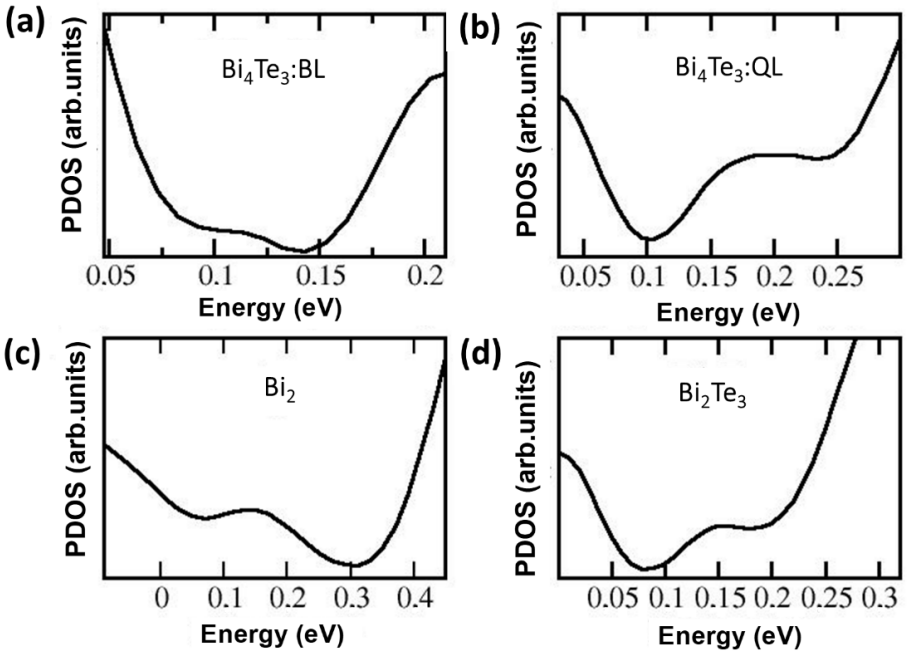

FIG. 5.7 – Projected density of states (PDOS) of band diagrams calculated using DFT for different surface terminations of Bi_4Te_3 and its constituents. PDOS of (a) Bi_4Te_3: BL, (b) Bi_4Te_3: QL, (c) Bi_2 and (d) Bi_2Te_3.

5.5 DISCUSSION

Concerning device applications, the observed phase coexistence of the Bi_2 and Bi_2Te_3 terminations in Bi_4Te_3 could, in principle, be used to produce tracks for selective conductance of electrons, should one need to filter different types of polarized electrons. These tracks could be manufactured by lithographic processes (e. g. via atomic force microscopy) at the surface. One can make use of Kelvin probe force microscopy to determine which portion of the material is finished in bi- or quintuple-layers and then use lithography to oxidize the 'channels' that are not of interest for each device application, designing the surface accordingly. Moreover, if one may control and/or manufacture nanometer-sized terminations by sputtering deposition and lithography, a path for

smaller electronic devices could be opened. Thus, modulated topological materials with different surface terminations are interesting for the fabrication of different topological insulator devices.

The remarkable coincidence of the surface electronic behavior of Bi_4Te_3 with that of the theoretical dispersion relation shows that only a few layers are necessary to reach the bulk electronic behavior. As a result, very thin films of this material may be manufactured in devices and will probably work as spin filter or similar applications.

5.6 ANGLE-RESOLVED PHOTOEMISSION SPECTROSCOPY RESULTS

In order to investigate the electronic structure of our system we have used angle-resolved photoemission spectroscopy (ARPES). ARPES measurements were performed at 77 K in an ultra-high vacuum chamber with pressure better than 2.0×10^{-10} mbar. We used a SPECS Phoibos 150 spectrometer at the PGM beamline of the Brazilian Synchrotron Light Laboratory (LNLS), Brazil. Data was collected using a helium lamp, with a photon energy of 21.21 eV. The energy resolution, including thermal broadening, and angular resolution were better than 77 meV and 0.1°, respectively.

Fig. 5.8 presents the dispersion relations of our Bi_4Te_3 system along the K-Γ-K (left panel) and M-Γ-M (right panel) directions in the first Brillouin zone. In this figure one observes an 'inverted-valley' structure around the Γ point below the Fermi level as well as a V-shaped band ranging from -0.4 eV up to the Fermi level. In particular, this V-shaped band deviates from its linear dispersion along the M-Γ-M direction bending near the Fermi level. This gives rise to a warped Fermi surface as presented in Fig. 5.9 [188-190]. Both structures show a high resemblance to those found for Bi_2Te_3 (see Fig. 2.13a shown in chapter II) [36]. However, important differences are observed in our sample. For instance, the 'inverted-valley' band has opposite and higher concavity than the conduction band of Bi_2Te_3, which is nearly flat close to the Γ point. This can be verified comparing the theoretical band structures of Bi_4Te_3: QL (see Fig. 5.2a) and Bi_2Te_3 (Fig. 5.3a) close to the Γ point to the experimental data presented in Fig. 5.8. In the case of Bi_4Te_3: QL, bulk and surface bands with the same concavity as the one found in our ARPES measurements are clearly seen close to the Γ point. For Bi_2Te_3, on the other hand, the

bulk bands located in the same region are indeed nearly flat. Furthermore, no evidence of an 'X' band is seen in our ARPES experiments. Considering this band to be a key element to identify Bi-rich terminations [16 169], i. e. the Bi-bilayer surface termination, these observations lead to the conclusion that the sample investigated here is mostly QL-terminated Bi_4Te_3. This will be further discussed in the following paragraphs, where our experimental measurements of constant energy contours will be directly compared to the corresponding theoretically calculated maps by means of DFT.

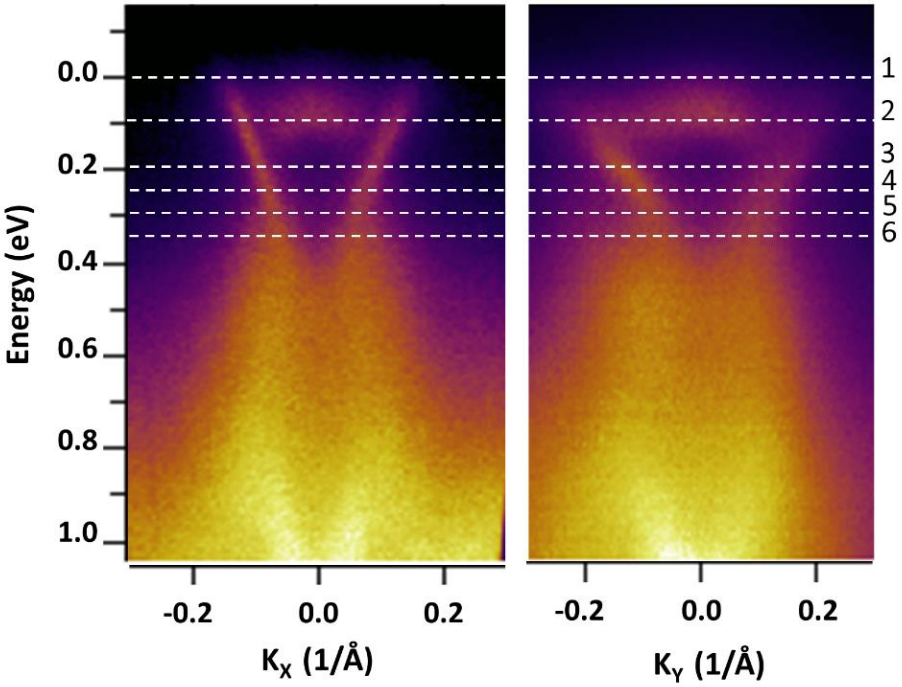

FIG. 5.8 – ARPES measurements of the band dispersions of Bi_4Te_3. ARPES intensity plots for (left panel) k_x and (right panel) k_y scans at the first Brillouin zone.

Fig. 5.9 shows a number of constant energy contours for several binding energies starting at the Fermi level up to 0.350 eV. The cutting planes are shown in Fig. 5.8 by the numbered dashed lines. For the Fermi surface shown in Fig. 5.9 one observes that the outer structure, formed by the V-shaped band, exhibits a hexagonal shape resembling a snowflake, while the inner structure around the Γ point, formed by the states of the 'inverted-valley', has a triangular shape (more clearly seen in panel 2 of Fig. 5.9). One also observes that the warped Fermi surface of Bi_4Te_3 has branches more elongated than those found for Bi_2Te_3 [36] (for a direct comparison, see Fig. 2.13b presented in chapter

II). In addition, these branches present what looks like 'gaps' at the corners of the hexagonal contour (along the Γ-M direction) making it discontinuous. At these regions, i. e. close to the edge of the Brillouin zone, one sees that these constant energy segments are almost parallel to each other, resembling a nesting effect [191, 192]. The increase of the binding energy results in continuous warped constant energy contours. In the case of Bi_2Te_3 warped Fermi surface acts as a platform for surface spin texture and surface scattering processes [189, 193, 194]. In our case, spin-ARPES measurements would be extremely useful to probe the spin properties of our system.

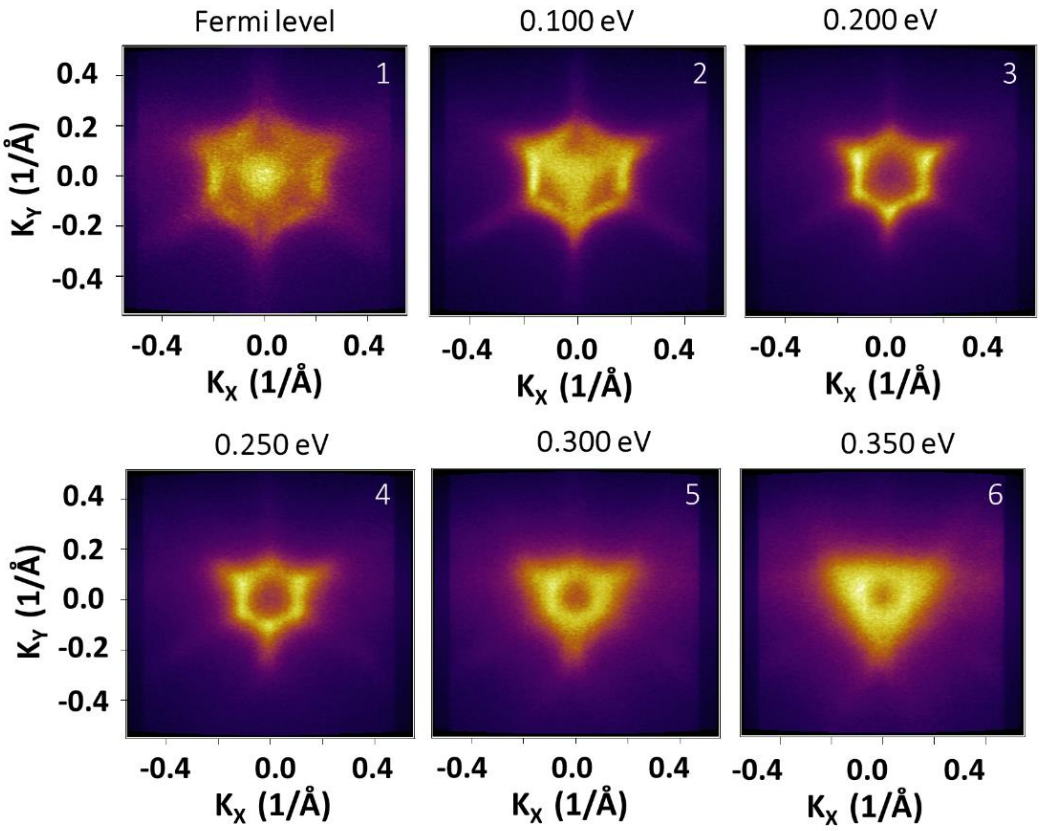

FIG. 5.9 – Constant energy contours of Bi_4Te_3 for different binding energies (indicated in each panel): Fermi level, 0.100 eV, 0.200 eV, 0.250 eV, 0.300 eV and 0.350 eV. The cutting planes are indicated by the numbered dashed lines depicted in Fig. 5.8.

Analyzing the 'inverted-valley' band of Bi_4Te_3 one notices that it has a triangular symmetry as well as the conduction band of Bi_2Te_3, but here it shows a different k_z dependence. In the ARPES experiments of Bi_2Te_3 performed by Chen et al. [36] a three-fold symmetry was observed for its conduction band for a photon energy of 19 eV and

23 eV (see Fig. 2.13b in chapter II). For photons with energy of 21 eV, on the other hand, they showed that the conduction band has six-fold symmetry. In contrast, in our system a three-fold symmetry was found for an energy of 21.21 eV. Furthermore, one observes that this inner band could be hybridized to the outer hexagonal contours, which can be seen more clearly in panel 2 of Fig. 5.9.

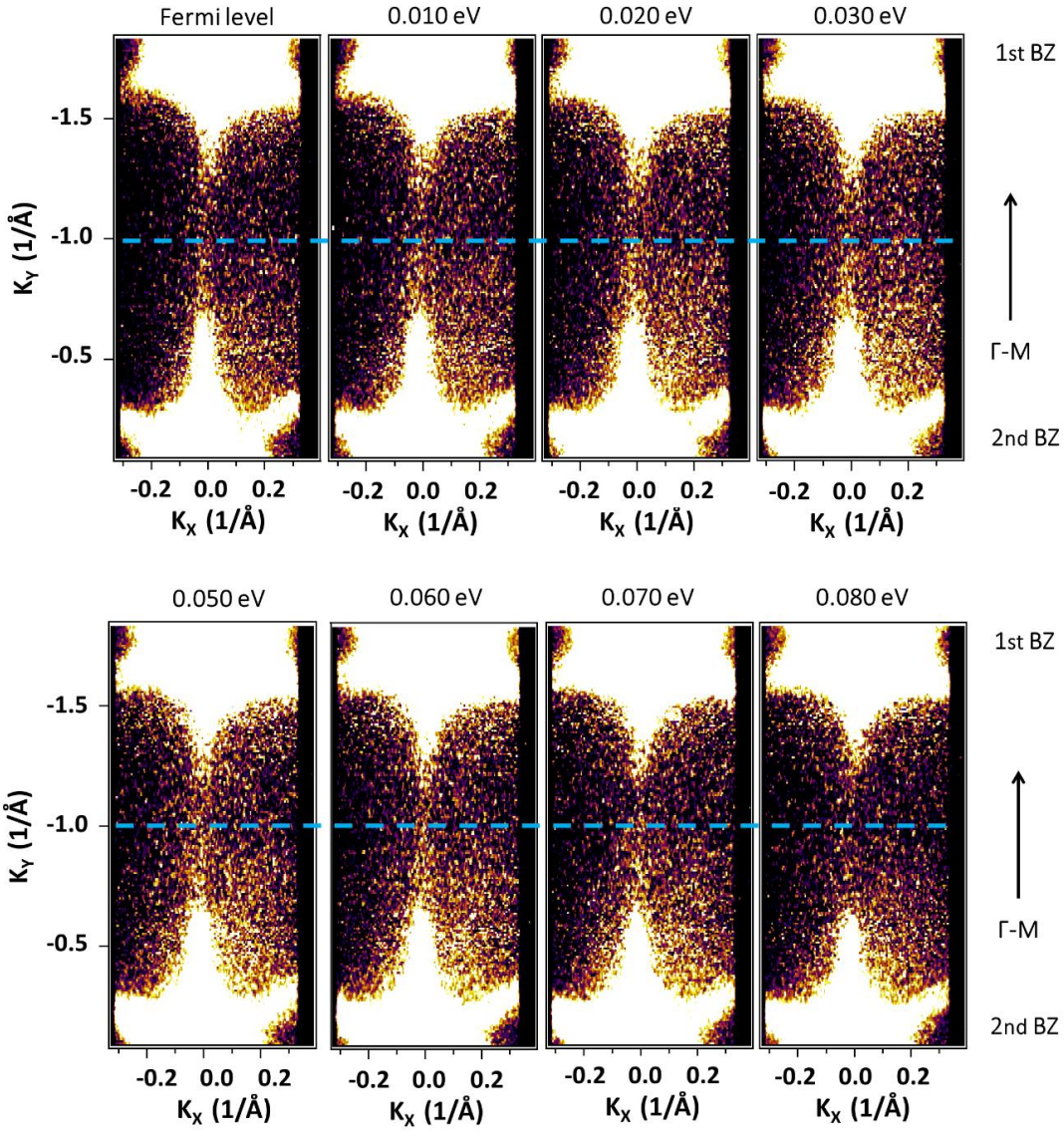

FIG. 5.10 – Constant energy contours of the Bi_4Te_3 system shown with high saturation for different binding energies (indicated in each panel): Fermi level, 0.010 eV, 0.020 eV, 0.030 eV, 0.050 eV, 0.060 eV, 0.070 eV and 0.080 eV. The blue dashed line marks the edge that separates the first and the second Brillouin zones. The Γ-M direction is indicated in this figure.

Additional ARPES measurements taken at 77 K using photon energy of 103.50 eV were carried out. The energy and the angular resolutions in this case, including thermal broadening, were better than 100 meV and 0.1°, respectively. This experimental data was also collected at PGM beamline at LNLS using the same experimental setup as previously stated. In this experiment the pressure was better than 2.0×10^{-10} mbar. These measurements were used to further investigate the elongated branches observed for the hexagonal constant energy contours and the 'gaps' along the Γ-M direction. In particular, the use of a higher photon energy allowed us to probe more than a single Brillouin zone and better understand the physical phenomena that take place at the edges of the Brillouin zone.

In Fig. 5.10 several constant energy contours for different binding energies (specified in each panel) are shown. In this figure one observes the first and the second Brillouin zones separated by a blue dashed line. In this data we have saturated the color scale to highlight the behavior of the branches along the Γ-M direction (which is indicated in the figure) close to the edge of the Brillouin zone. In particular, it is possible to observe that at the Fermi level the elongated branches do not seem to touch the edges of the Brillouin zone. As we show other slices of constant energy contours for higher binding energies one observes that the intensity at the M point increases, with a giant stretching forming a bridge-like structure connecting the first and the second Brillouin zones (see constant energies contours from 0.030 eV up to 0.060 eV to see this more clearly). As we further increase the binding energy, going to values above 0.060 eV, these elongated branches no longer touch the edge of the Brillouin zone as one can see for a binding energy of 0.080 eV. This is an indication of a band distortion of Bi_4Te_3 in relation to the Bi_2Te_3 bands. Bi_2Te_3 has a topological state, i. e. the Dirac cone that crosses the Fermi level as a single band. As we introduce Bi_2 layers into the system forming Bi_4Te_3 this topological state bends below the Fermi level. In this context, one observes what could be an 'electronic topological gap' of 0.060 eV along the Γ-M direction. It is noteworthy that this phenomenon is at the limit of the system resolution and would have to be further investigated with higher resolution to be confirmed. This remarkable effect opens up possibilities for a number of new experiments with a lot of interesting physics to be further explored.

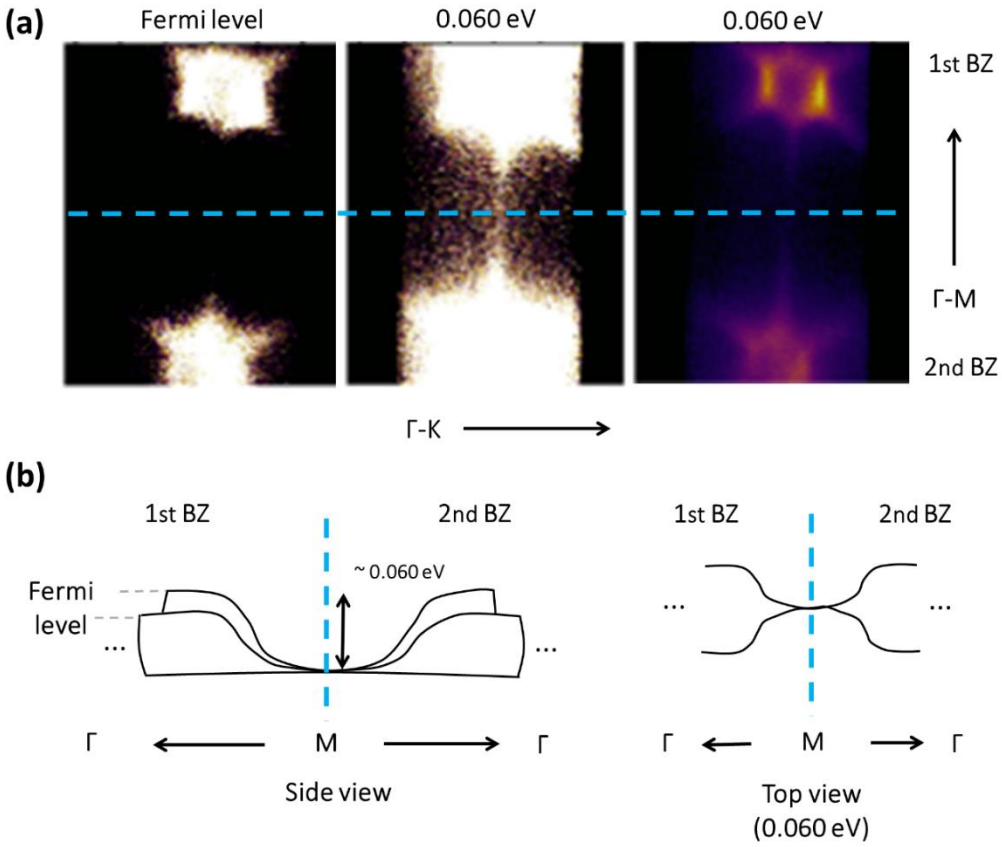

FIG. 5.11 – (a) Constant energy contours of Bi_4Te_3 shown (left panel) with high saturation at the Femi level and at (middle panel) a binding energy of 0.060 eV. (Right panel) Constant energy contour at a binding energy of 0.060 eV shown without high saturation for comparison. The blue dashed line marks the edge that separates the first and the second Brillouin zones. The Γ-M direction is indicated in this figure. (b) Schematics of the branches of the hexagonal constant energy contours. (Left panel) The bands are shown from the side and (right panel) from the top along the Γ-M direction.

This phenomenon can be seen more clearly in Fig. 5.11a where we present constant energy contours collected at the Fermi level and at 0.060 eV, as indicated in each panel. In both cases the data is again presented with high saturation. The energy contour at 0.060 eV is also presented in a distinct color scale for comparison purposes. At the Fermi level, as previously discussed, the branches do not extend up to the edge of the first Brillouin zone. For the equipotential surface at 0.060 eV, on the other hand, the opposite behavior is seen, with the giant stretching forming a bridge-like structure between the first and the second Brillouin zones. This is schematically indicated in Fig. 5.11b, in which these bands are shown along the Γ-M direction from the side (left panel)

and from the top (right panel). As previously described, a 'gap' between the branches slowly decreases and is completely absent at 0.060 eV. This opening, together with the giant stretching for higher binding energies, gives rise to what resembles an 'electronic topological gap' of approximately 0.060 eV along the Γ-M direction, meaning that in this system no topological states cross the Fermi level along this direction

5.7 THEORETICAL CONSTANT ENERGY CONTOURS OF Bi_4Te_3

The band structures of Bi_4Te_3: QL and Bi_4Te_3: BL, as shown in Fig. 5.2, were used to plot the constant energy contours of both terminations and, consequently, allowed us to do a comparative analysis. The bulk Bi_4Te_3 (21 atoms) tight-binding Hamiltonian was obtained by interpolating the bands via Wannier functions [195]. With this Hamiltonian one can calculate spectral functions for a given surface. In our case both surface terminations were considered, i. e. the quintuple-layer and the bilayer terminations. A slab composed of 30 heptalayers of Bi_4Te_3 was used. The formalism used here is described in reference [196]. It is noteworthy that when calculating the constant energy contours, the Brillouin zone mapping was done using primitive vectors. This is the reason why some structures with elliptical symmetry (in some cases this symmetry deviates) appear in some constant energy contours, presented in Figs. 5.12 and 5.13, where the Wigner-Seitz cell should have ended.

In Fig. 5.12 and Fig. 5.13 several equipotential theoretical maps of Bi_4Te_3: QL and Bi_4Te_3: BL are presented, respectively. The corresponding energies, below (indicated with the use of a minus signal) and above the Fermi level (indicated with the use of a plus signal), are shown in each panel. In addition, the redder the structures the greater the contribution of surface states. As one observes the Fermi surface (0 eV) of Bi_4Te_3: QL (see Fig. 5.12) has a six-fold symmetry that highly resembles our experimental measurements shown in Fig. 5.9. In this panel, a hexagonal contour with elongated branches is seen. For +0.050 eV the 'gaps' at the corners of the hexagonal contours are more pronounced. Also, an inner structure is visible in these panels at the middle of this hexagonal structure, i. e. at the Γ point. As the energy further increases the constant energy contours become more complex. The same happens when the energy is decreased below the Fermi level.

The constant energy maps of Bi_4Te_3: BL have similar features. However, important differences allow one to distinguish between these two cases, especially for energies close to the Fermi level. For 0 eV, +0.050 eV and -0.050 eV a six-fold symmetry similar to a snowflake is seen, but in this particular case there is no nesting and the contours are continuous, which here is the key element to distinguish between the two terminations. These results, together with the analysis of the band structure, strongly suggest that Bi_4Te_3: QL covers up most of the sample surface.

In summary, a comparison between our experimental data and the DFT calculations indicates that the 'inverted-valley' state at Fermi level observed in the ARPES diagram may be ascribed to the n-doped QL-terminated Bi_4Te_3. In addition, the theoretical maps also indicate that the V-shaped band can be attributed to Bi_4Te_3: QL. No specific features of isolated Bi_2 layers or Bi_2Te_3 were observed in our measurements, albeit the sample is composed of (28 ± 3)% of Bi_2 and (8 ± 2)% of Bi_2Te_3. This result is likely because the contributions of these phases were overlapped by the Bi_4Te_3 contributions. In this context, one can speculate that the relation between the large size of the beam (1000 x 1000 nm) and the reduced sized of Bi_2 and Bi_2Te_3 domains plays a crucial role on reducing their ARPES footprints.

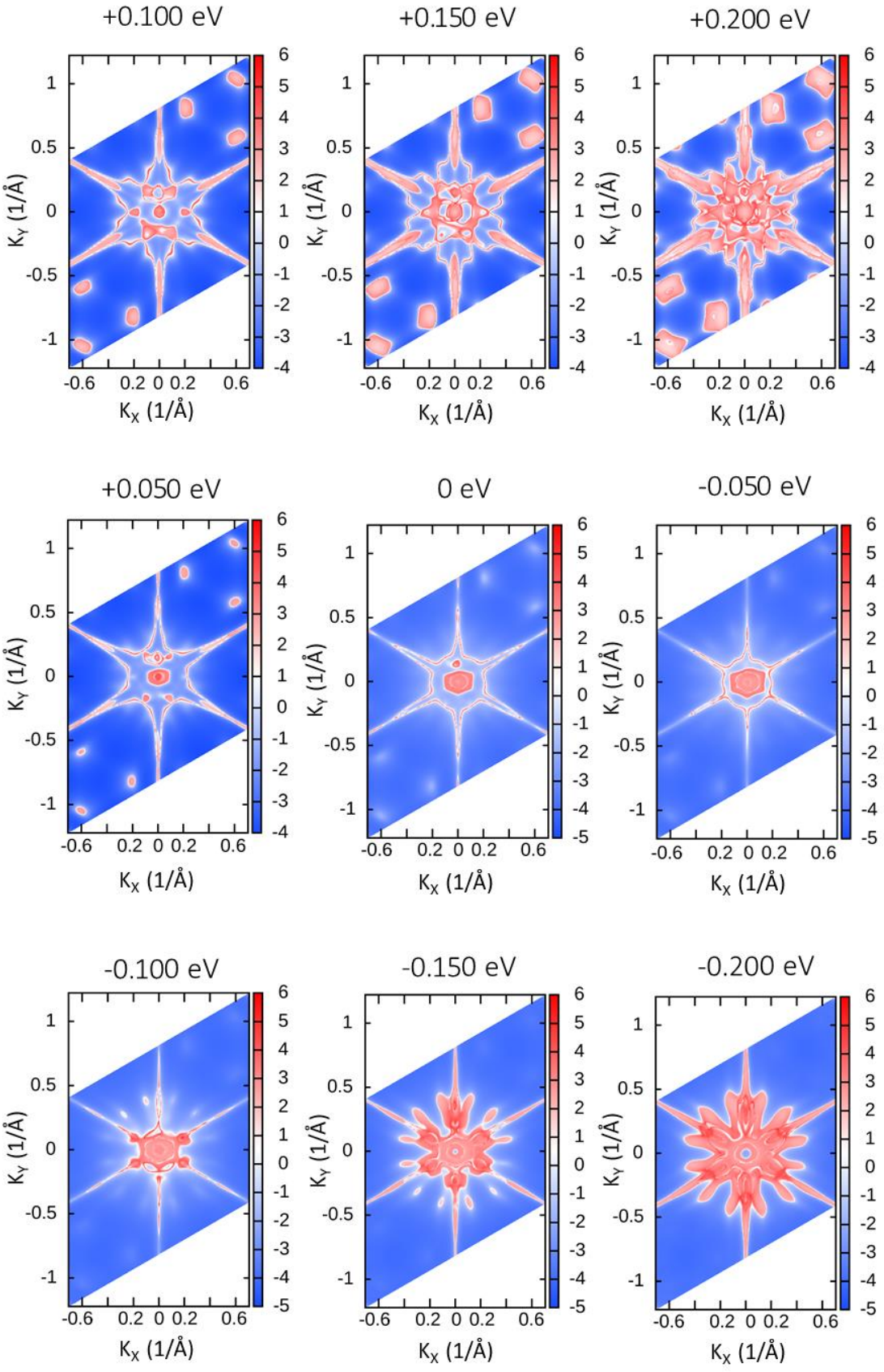

FIG. 5.12 – Constant energy theoretical maps calculated for Bi_4Te_3: QL. The energy is indicated in each panel. The Fermi level is set to zero.

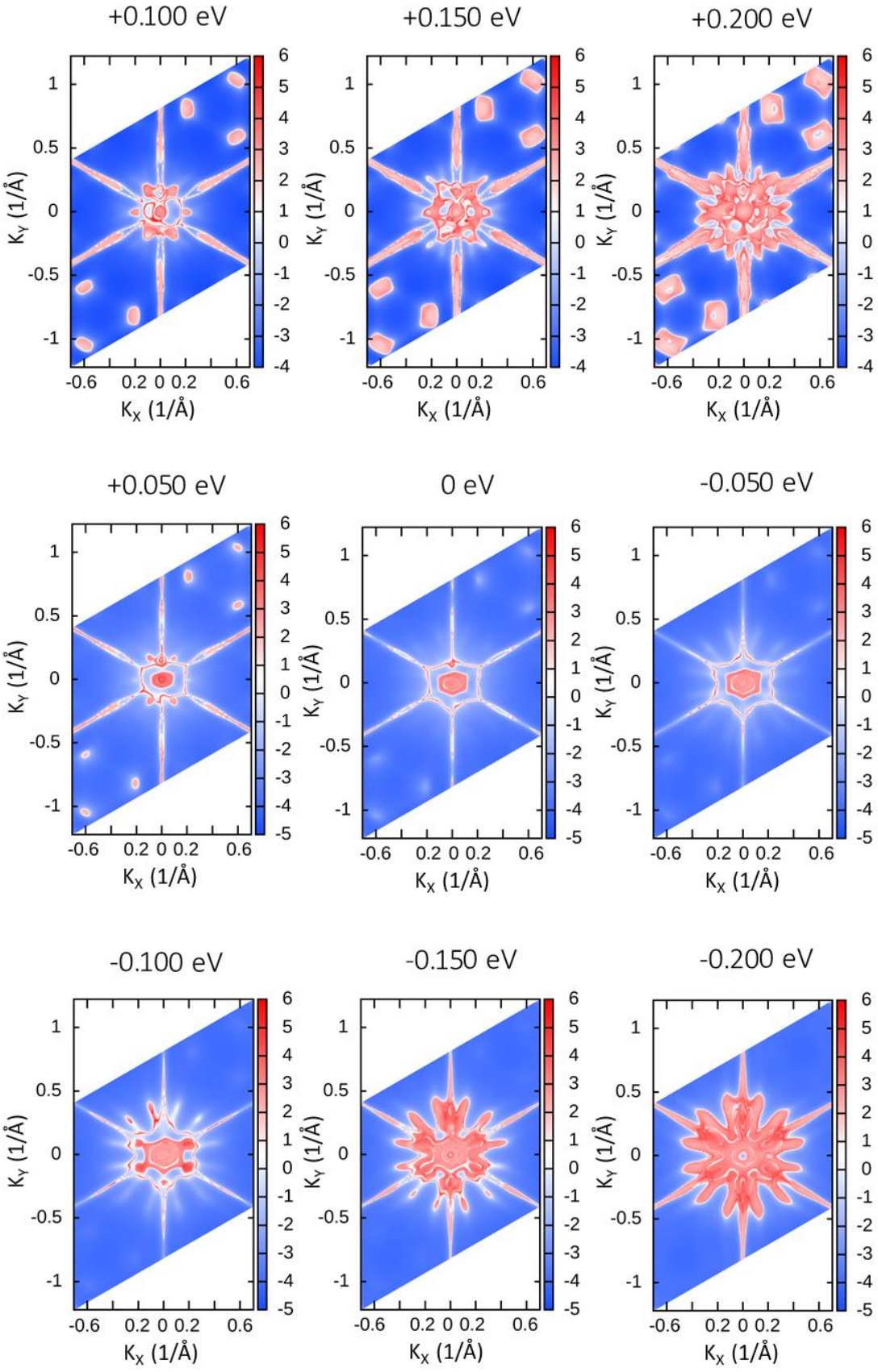

FIG. 5.13 – Constant energy theoretical maps calculated for Bi_4Te_3: BL. The energy is indicated in each panel. The Fermi level is set to zero.

5.8 CONCLUSIONS

In this chapter an original study of the electronic properties of the strong topological insulator Bi_4Te_3 was presented. A combination of density functional theory and scanning tunneling microscopy/spectroscopy techniques were used to investigate its electronic properties. We have been able to separate the contributions from the surface states of this material, which are more important for electronic transport than the bulk ones. The dispersion relations of the two surface terminations of Bi_4Te_3, i. e. Bi_2 and Bi_2Te_3 were also studied separately. In addition, the analysis of height-profiles of the STM topographic images and STS signatures of different areas of our system permitted us to identify regions of Bi_4Te_3: QL, Bi_4Te_3: BL, Bi_2Te_3 and Bi_2. This allowed us to understand both structural and electronic properties of all these distinct Bi-Te phases. Such information may be used to produce tracks manufactured by lithographic processes for selective conductance of electrons at the surface, which would be interesting for the fabrication of different topological insulator devices. Finally, angle-resolved photoemission spectroscopy measurements suggest that the main composition of the sample surface is Bi_4Te_3: QL. Highly warped constant energy contours with 'gapped' branches give rise to an 'electronic topological gap' along the Γ-M direction and as a result no topological states cross the Fermi level along this specific direction.

VI.

SELF-ASSEMBLY OF TRIANGULAR S TRIMERS ON Au(111)

In this chapter we systematically investigate structural and electronic properties of TaS_2 on Au(111) using scanning tunneling microscopy/spectroscopy and low-energy electron diffraction. TaS_2 films were synthetized through the evaporation of tantalum in a background of H_2S, used as a source of sulfur. The use of high H_2S pressures and annealing temperatures proves not to be ideal for growth of TaS_2 domains, since the quantity of islands scattered throughout the sample surface considerably decreases, and is replaced by a number of S trimers at the high temperature regime. The emergence of these structures distorts the Au(111) herringbone reconstruction. In addition, the nanoclusters, which cover approximately 0.60 % of the surface, are mostly located on the face-centered cubic regions of Au(111). High resolution scanning tunneling microscopy images were carried out, revealing not only a well-defined triangular shape of these nanoclusters, but also demonstrating different orientations depending on the region of Au(111) in which they sit. Finally, density functional theory calculations are presented to investigate different structures adsorbed and also embedded on Au(111).

6.1 INTRODUCTION

Transition metal dichalcogenides (TMDCs) have attracted enormous attention in past years due to their unique properties, especially as ultrathin layers [37-39]. These materials have emerged as an alternative to graphene, overcoming some of its intrinsic limitations, such as the absence of an electronic band gap [3]. Nevertheless, TMDCs are not suitable replacements for graphene in all device applications, since their structure leads to the loss of some of its remarkable properties, such as its mobility [24]. Many TMDCs have a semiconductor behavior with sizable band gaps, making them promising candidates for nanoelectronics devices [40]. Metallic TMDCs, like TaS_2, have distinct, but exotic properties, like charge density waves and superconductivity [44-46].

In order to incorporate this class of materials into current electronic devices, an in-depth comprehension of their properties under different conditions is required. In this context, it is important to increase the knowledge of the role played by the growth parameters on their synthesis, which is essential not only to establish a controlled growth on different platforms, but also to improve the understanding of thin films formation. From the fundamental point of view, this process starts with the deposition of the constituents of the transition metal dichalcogenide on a proper substrate. Studies focusing on such goals represent a relevant contribution, building up the knowledge of epitaxial growth processes, revealing valuable information about the nucleation sites and the deposition kinetics [197-202]. In addition to these contributions, important particularities about the elementary blocks of TMDCs as intercalant elements are unveiled, which are useful for modifying properties of layered materials. Also, it is often reported in the literature that these adsorbates can aggregate and form clusters. These nanometer-sized structures can present interesting and desirable properties for catalytic and magnetic applications [197-200].

In this chapter, we investigate, using scanning tunneling microscopy, TaS_2 films synthetized on Au(111) substrates. In particular, the effect of high H_2S pressures and high annealing temperatures on the formation of these thin films was studied. At such conditions the formation of regular triangular TaS_2 islands is no longer favorable, and the substrate is covered mainly with nanoclusters. These self-assembled structures sit

preferentially on face-centered cubic (fcc) sites of the Au(111) surface and modify its well-known herringbone reconstruction. In addition, atomically-resolved images reveal that these nanometer-sized S trimers present a well-defined triangular shape with distinct orientations depending on the region of the Au(111) substrate in which they are located, i. e. fcc or hexagonal close-packed (hcp) regions.

6.2 SAMPLE GROWTH: TaS_2 on Au(111)

TaS_2 islands grown on Au(111) substrates were synthesized and investigated during my doctoral stay (PDSE-CAPES fellowship) at Universität Siegen, Germany. The first step of the sample growth consists in the preparation of the Au(111) substrate, which is done through cycles of sputtering and annealing. In particular, the sample was sputtered using 1.50 kV argon ions (pressure of 1.0×10^{-7} mbar) at 300 K for 30 minutes. This process was followed by another cycle of sputtering at 900 K also for 30 minutes and completed by annealing the substrate at 900 K for 10 minutes. After the preparation of the Au(111) substrate, low-energy electron diffraction (LEED) and scanning tunneling microscopy/spectroscopy (STM/STS) were used to characterize the sample and assure that the substrate was clean and free of contaminations (resulting from previous preparations). An assurance that would serve as a guarantee of the suitableness of the substrate for the synthesis of TaS_2 films. All STM images presented in this chapter were obtained using the scanning tunneling microscope TuMA III operating at room temperature (300 K) and ultra-high vacuum conditions ($< 1.0 \times 10^{-10}$ mbar). In addition, spectroscopic data were acquired measuring current versus voltage profiles at specific regions. dI/dV curves were obtained through numerical derivative of an average of a number of I(V) curves. The reproducibility of the experimental data was always taken into account by analyzing the shape of several STS curves measured at the specific points.

In Fig. 6.1a one observes a LEED pattern of the clean Au(111) substrate measured at 65 eV. In this image one sees the diffraction spots of the Au(111) surface in brighter contrast surrounded by satellite spots related to the herringbone reconstruction. In particular, the diffraction peaks inside the black circle in this figure can be seen in greater detail in the inset of this panel. In Fig. 6.1b an STM topographic image of an atomically

flat terrace of this sample is presented. In this figure one sees the herringbone reconstruction formed by a pattern with a number of straight and parallel ridges. It is well-known that in this reconstruction these ridges are Au atoms at a higher level sitting in the saddle positions between regions of fcc surface structure, seen as large alternating regions, and hcp structures, seen as narrow alternating regions [203-206]. In addition, an atomically-resolved STM image and a scanning tunneling spectrum, which is proportional to the local density of states of the sample, could also be measure as presented in Figs. 6.1c and 6.1d, respectively. In Fig. 6.1d one also identifies the surface state of Au(111) approximately at -0.40 eV [207].

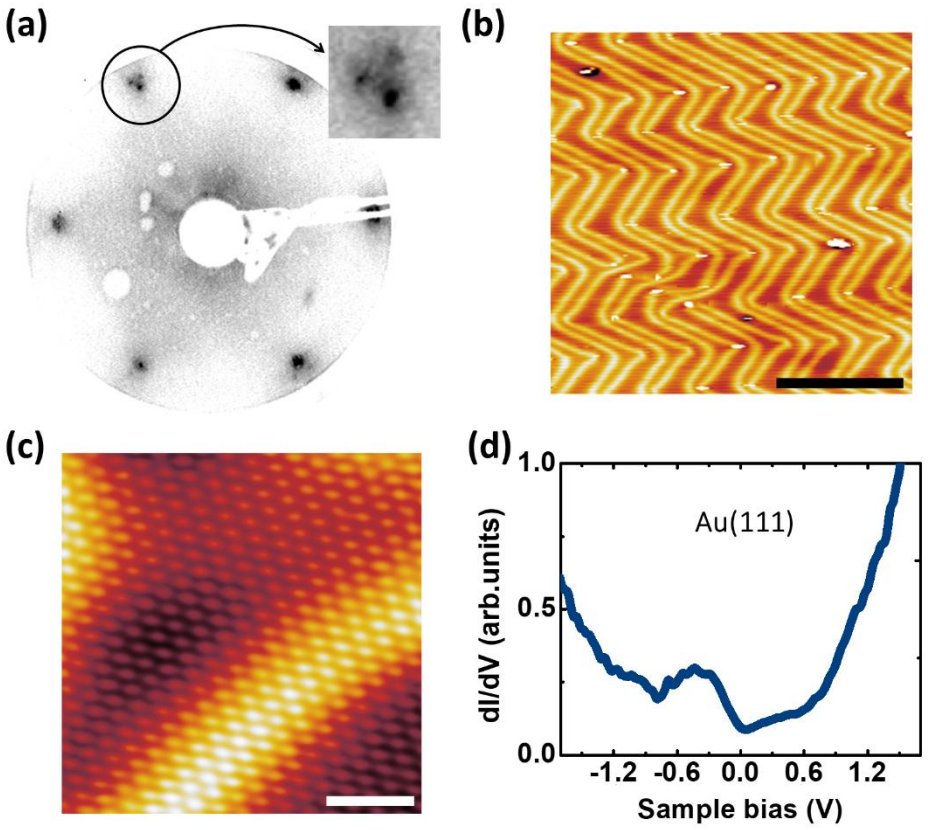

FIG. 6.1 – (a) LEED data of clean Au(111) measured at 65 eV (inverted contrast). The diffraction spots are shown in detail in the inset of this panel. (b) STM topographic image of Au(111). The stripe pattern seen refers to the herringbone reconstruction. (c) Atomically-resolved STM image of Au(111). (d) Tunneling spectrum measured in a clean Au(111) sample. The scale bars are: (b) 20 nm and (c) 1 nm.

TaS_2 films were synthetized in situ using an evaporator which allows the deposition of the transition metal (in this particular case tantalum) directly onto the

Au(111) substrate. A scheme of the growth process is shown in Fig. 6.2. In particular, for the system investigated here the power of the evaporator was adjusted to 73 W and tantalum was evaporated for 2 minutes and deposited on Au(111) at room temperature (300 K). Simultaneously, the sample was exposed to an H_2S environment (used as source of sulfur) at a pressure of 1.0×10^{-6} mbar (see Figs. 6.2a and 6.2b). After the tantalum deposition the sample was annealed at 950 K for 20 minutes (Fig. 6.2c). In this growth process the following chemical reaction takes place, starting the formation of TaS_2 islands [208]:

$$\mathrm{Ta} + 2\mathrm{H_2S} \rightarrow \mathrm{TaS_2} + 2\mathrm{H_2}. \tag{6.1}$$

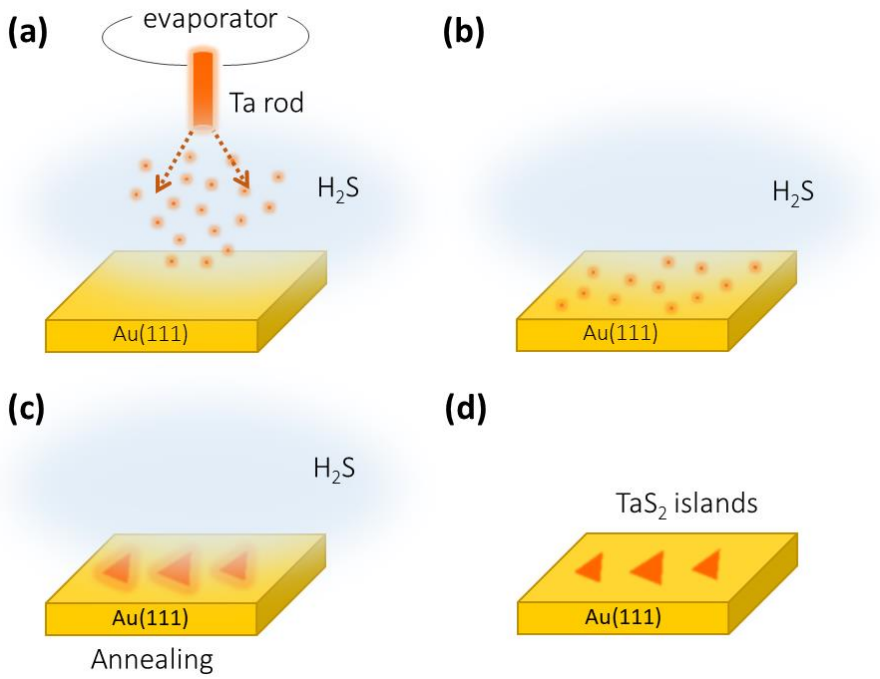

FIG. 6.2 – Schematic representation of the synthesis of TaS_2 films on Au(111). (a) Ta rods are evaporated onto clean Au(111) at room temperature in an H_2S environment. (b) The Ta particles adsorb on the Au(111) surface. (c) After the Ta deposition the system is annealed (starting the formation of TaS_2 islands) and, subsequently, cooled down in H_2S. (d) At the end of the process several TaS_2 islands with a triangular morphology are formed on Au(111) surface.

After annealing, the system was cooled down also in an H_2S environment until 450 K was reached. At the end of this procedure, a number of TaS_2 islands was formed on top of the Au(111) substrate as schematically depicted in Fig. 6.2d.

Subsequently, the system was investigated using LEED to ensure a good sample preparation (see Fig. 6.3a). In this LEED pattern one can see Au(111) diffraction peaks (one of which is labeled with a blue circle) as well as the TaS_2 spots (pink circle). In particular, this LEED pattern also reveals, through the observation of satellite peaks, the formation of a moiré pattern as a result of the mismatch of the Au(111) and the TaS_2 lattices. The in-plane lattice parameters of Au(111) and 1H-TaS_2 are 0.2885 nm [209] and 0.3342 nm [96], respectively. In the inset of this panel these diffraction spots can be seen in more detail.

In addition, the system was also investigated using STM/STS techniques. STM images revealed the formation of a number of 2D TaS_2 islands (in brighter contrast) scattered throughout the sample as depicted in Fig. 6.3b. The TaS_2 islands have a triangular morphology and varied sizes. One also observes that the TaS_2 islands have well-defined orientations, with some islands pointing up or down (see the islands located on the upper left side in Fig. 6.3b).

In Fig. 6.3c one of the TaS_2 islands is shown in more detail. In this image one identifies the moiré pattern within the TaS_2 domain surrounded by the Au(111) herringbone reconstruction. Moreover, in the inset of this figure some nanoclusters, appearing as white dots, can be seen on the Au(111) regions. These nanoclusters are further investigated in the following sections. In Fig. 6.3d a different region of the sample, with relatively large TaS_2 islands, is presented. Fig. 6.3e is a magnification of the upper Tas_2 domain shown in Fig. 6.3d. In this atomically-resolved image the moiré pattern with some defects is seen in detail. Through the analysis of this moiré pattern one can also identify the formation of distinct TaS_2 phases, i. e. 1H-TaS_2 or 1T-TaS_2. In the particular case of this domain, the TaS_2 lattice constant was found to be (0.332 ± 0.002) nm, which is compatible with the 1H phase, consistent with the study of Sanders and her co-workers, who also investigated TaS_2 on Au(111) [46]. In Fig. 6.3f the tunneling spectrum of the TaS_2 island, in which one observes the metallic character of this structure, is presented.

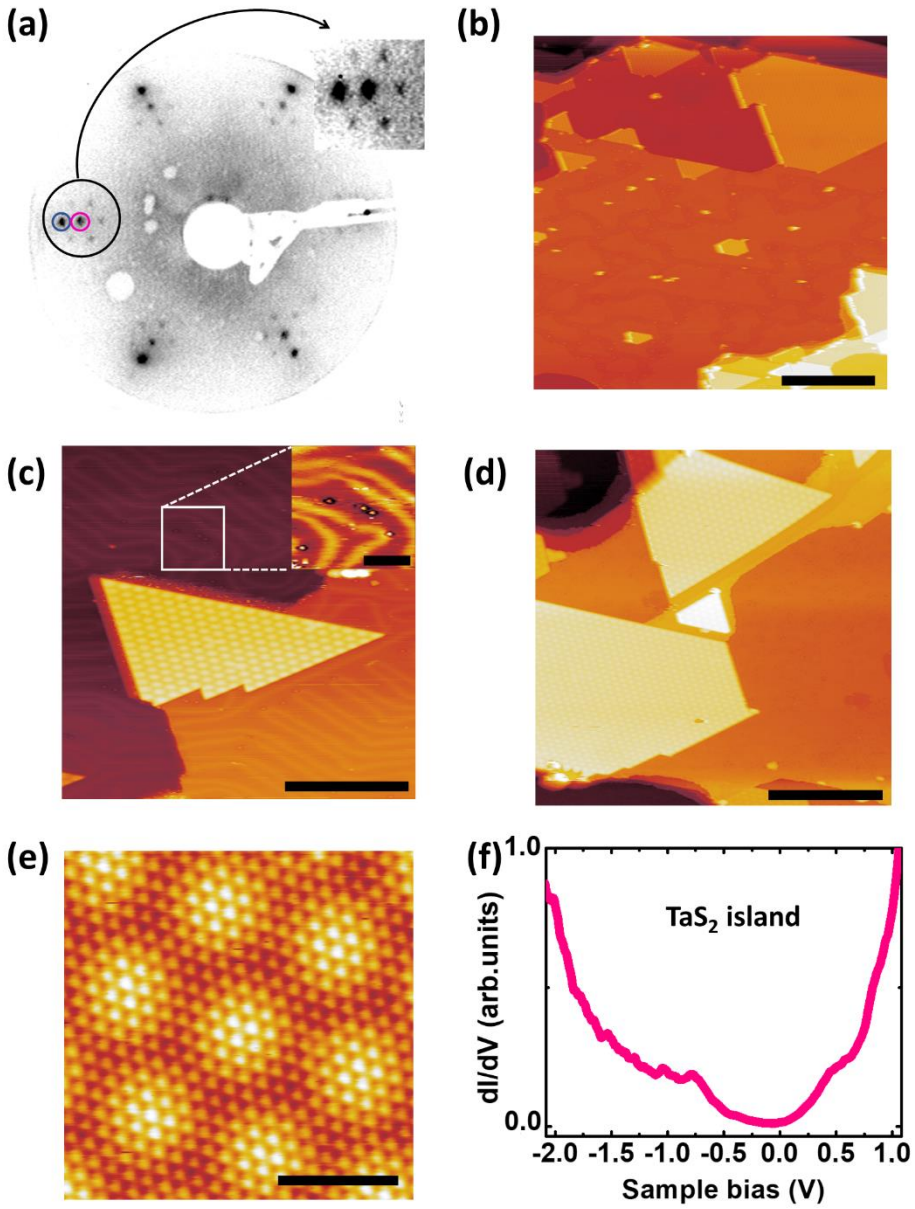

FIG. 6.3 – (a) LEED data of TaS_2 on Au(111) – sample partially covered – measured at 65 eV (inverted contrast). The diffraction spots of Au(111) and TaS_2 are marked with blue and pink circles, respectively. The satellite spots are due to the moiré pattern. These spots are also shown in detail in the inset of this panel. (b) STM topographic image of TaS_2 islands on Au(111). The islands have a triangular morphology and can be seen in brighter contrast. (c) Zoom image of a TaS_2 island. In this image one sees the moiré pattern within the triangular island as well as the herringbone reconstruction on Au(111). On the Au(111) region it is possible to observe (inset) some nanoclusters that appear as bright dots on the herringbone reconstruction. (d) A different region of the sample showing more TaS_2 islands. (e) Atomically-resolved image of the moiré pattern of the island shown in the upper region of panel (d). (f) STS measured at a TaS_2 island. The scale bars are: (b) 50 nm, (b, inset) 5 nm, (c) 20 nm, (d) 30 nm and (e) 2 nm.

6.3 STRUCTURAL AND ELECTRONIC PROPERTIES OF TRIANGULAR S TRIMERS

It is well-known that the variation of the growth parameters such as temperature and pressure plays an important role in the synthesis of different systems. The size and density of the TaS_2 domains as well as their formation, for example, are strongly affected by the growth conditions. Thus, by varying the growth parameters one can modified the system of interest and, consequently, better understand the dynamics of the formation of TaS_2 islands on Au(111). In particular, the increase in the growth temperature and pressure completely modified the system investigated here giving rise to a number of nanoclusters, like the ones observed in the inset of Fig. 6.3c, which replace almost completely the regular triangular TaS_2 islands.

In Fig. 6.4 some STM images of the sample synthetized as described in section 6.2, but at a pressure of 1.0×10^{-5} mbar of H_2S and annealed at 1100 K for 20 minutes, are presented. In Fig. 6.4a one sees large atomically flat terraces and a triangular TaS_2 island in the middle. This image shows how the density of TaS_2 islands decreased for this sample preparation (this was confirmed by analysis of other regions of the as-grown system). Fig. 6.4b, which is a magnification of the island shown in Fig. 6.4a, highlights the moiré pattern of the TaS_2 domain. In addition, one sees a number of small dots on the Au(111) surface. Moreover, Fig. 6.4a reveals some medium-sized triangular islands (brighter contrast), shown in detail in Fig. 6.4c. A region of the Au(111) substrate with a number of nanoclusters, appearing as small white dots, on the distorted herringbone reconstruction is depicted in Fig. 6.4d. The analysis of large atomically flat regions of the Au(111) surface with clusters revealed that (0.60 ± 0.09)% of the system is covered with these adlayer structures [209].

Additional measurements were carried out to investigate the composition of the nanoclusters. The first experiment consisted in a sample preparation without H_2S, meaning that tantalum was be deposited onto Au(111) at room temperature and, posteriorly, annealed at high temperatures. Our experimental data (not shown) revealed the appearance of larger clusters without well-defined shapes coexisting with some triangular trimers (the mean distance among the adatoms for this structure is (0.785 ±

0.003) nm, which does not correspond to the mean distance among the adatoms for the nanoclusters observed in standard preparations). In the second experiment Au(111) substrate was annealed at high temperatures in a H_2S background. Such study revealed the formation of triangular nanoclusters like the ones previously observed (the mean distance among the adatoms in this case is (0.324 ± 0.003) nm, compatible with the trimers as shall be shown, which is a strong indication that these structures are triangular S trimers).

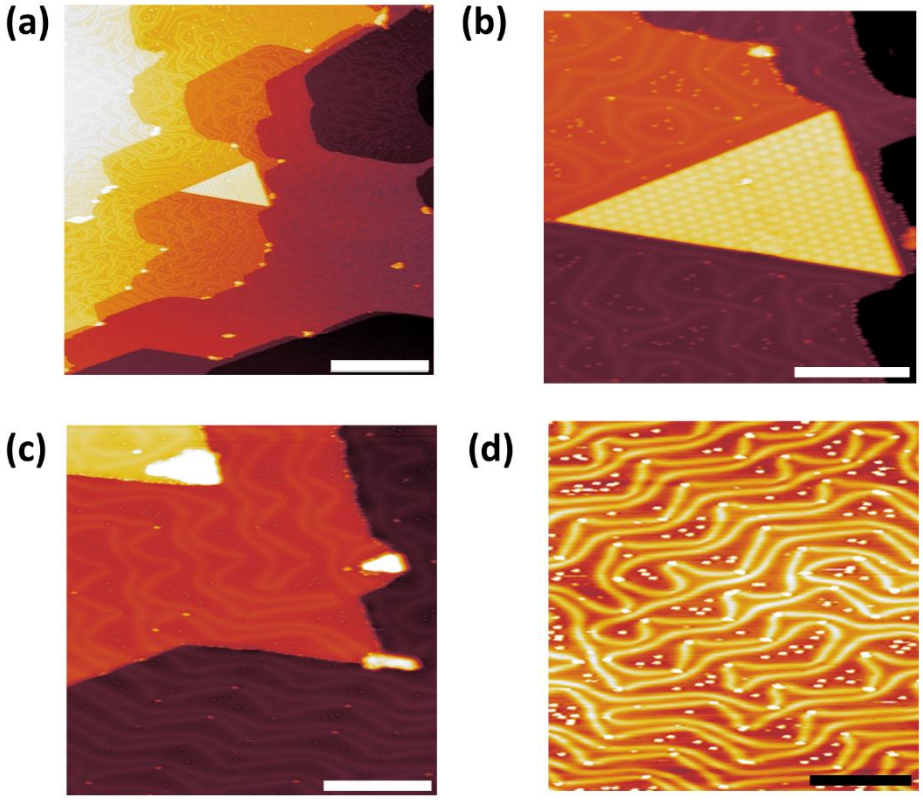

FIG. 6.4 – STM topographic images of TaS_2/Au(111) covered with a number of nanoclusters. In panel (a) one sees a large TaS_2 island (highlighted in (b)) in the middle of Au(111) terraces. Middle-size triangular islands and a number of nanoclusters on the distorted Au(111) herringbone reconstruction are also visible in (a), but are magnified in panels (c) and (d), respectively. The scale bars are: (a) 50 nm, (b) 15 nm, (c) 15 nm and (d) 15 nm.

In Fig. 6.5 atomically-resolved STM images of the S trimers as well as the Au(111) substrate are presented to provide further insights on the understanding of this adlayer structure. In Fig. 6.5a one sees a number of S trimers scattered throughout the substrate. In this figure one observes that these nanoclusters are grouped in a well-defined

triangular morphology and that all of them have the same alignment regarding Au(111). One of these triangular trimers, shown in Fig. 6.5a, is magnified in Fig. 6.5b. In Figs. 6.5a and 6.5b it can be noticed that a dark contrast surrounds the left side of the triangular S trimers. Also, in this distorted region the atomic resolution of the Au(111) is not as visible. Forward and backward STM topographic scans were analyzed, but no significant differences regarding these dark regions were observed, meaning that this is probably not a scanning effect. It is well-known that the deposition of different elements starts at defects on terraces and step edges [197, 198]. For our system, a large number of S trimers were observed at monoatomic step edges (not shown) and on terraces, in such case very often with a dark region surrounding them. This is an evidence that these regions are structural defects of Au(111) caused by the high annealing temperatures of the system in the synthesis (1100 K). It is noteworthy that during the STM measurements surface diffusion was not detected and the S trimers remained static even with the application of very low sample bias and high tunneling currents. This indicates that these structures are well anchored on the substrate.

In addition, the distances among the three adatoms of this triangular trimer were measured through the height-profiles indicated by the black solid numbered lines depicted in Fig. 6.5a. These profiles are shown in Fig. 6.5c. The measurements in question revealed the 'interatomic distances' along the directions 1, 2 and 3 as (0.304 ± 0.003) nm, (0.279 ± 0.003) nm and (0.304 ± 0.003) nm, respectively. Fig. 6.5a allowed also the determination of the surface lattice constant of Au(111): (0.292 ± 0.005) nm, compatible with the values reported in literature [210]. Other trimers were analyzed and the average results in the directions 1, 2 and 3 are: (0.303 ± 0.003) nm, (0.297 ± 0.003) nm and (0.314 ± 0.003) nm, respectively. This result is compatible with the mean distance among the adatoms for the Au(111) sample prepared in a H_2S background, as previously stated. The mean distance between trimers localized only in the same fcc region (considering their centers as a reference) was also systematically analyzed. The average value obtained was (2.8 ± 0.5) nm.

In Fig. 6.5d the atomically-resolved STM image of the S trimer, presented in Fig. 6.5b, is used to investigate the atomic positions of this triangular structure regarding the atomic positions of the Au(111) substrate, which are marked with gray circles. From this

image one can verify that the adatoms that compose the trimer are sitting at hollow sites. This is schematically indicated in Fig. 6.5e in which Au(111) is shown through gray circles, while the triangular S trimers are presented using black ones.

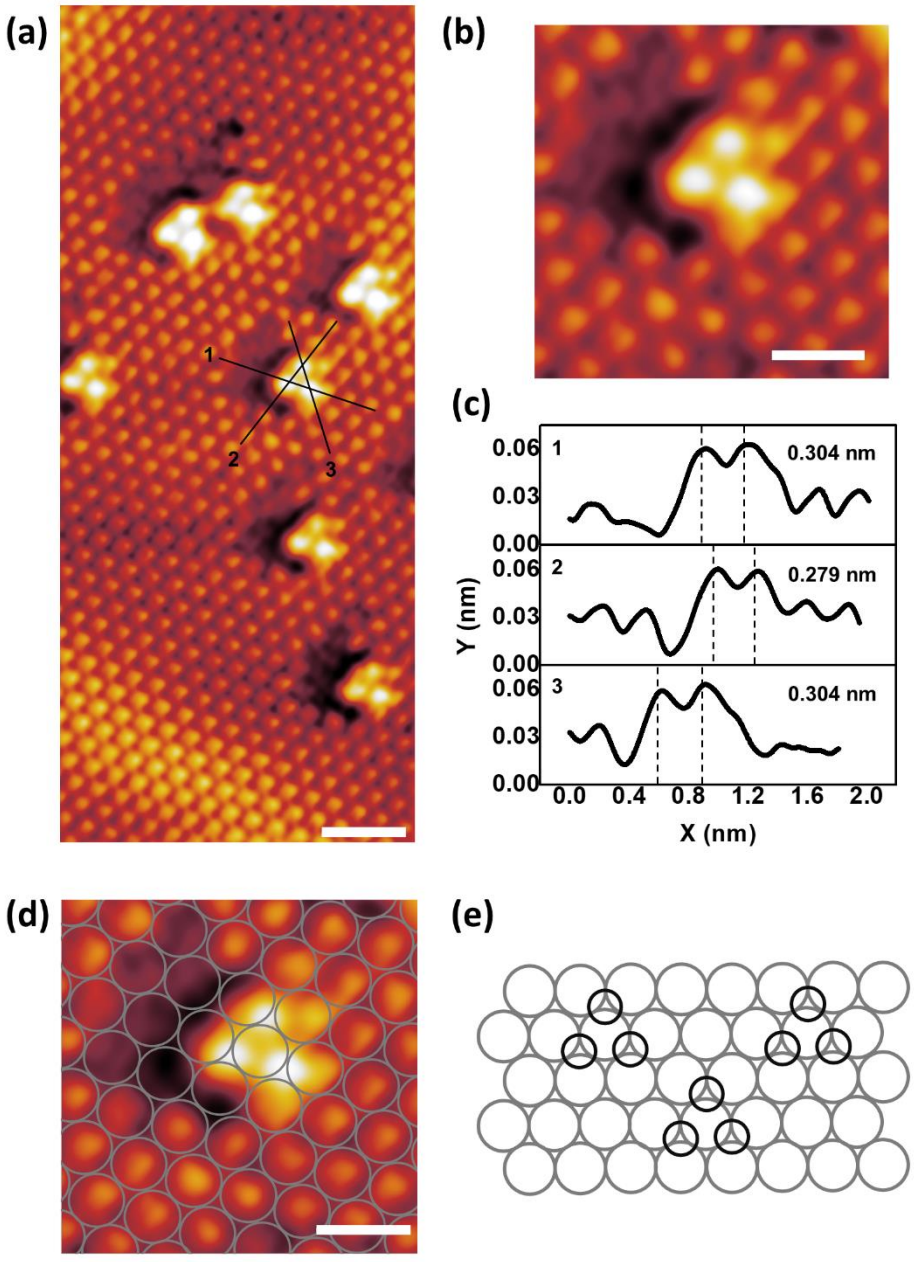

FIG. 6.5 – (a) Atomically-resolved STM topographic image of the triangular S trimers on Au(111). (b) Magnification of one of these adlayer structures shown in (a). (c) Height-profiles along the black solid numbered lines shown in (a). (d) The image shown in (b) is repeated here highlighting the position of the Au atoms of the substrate with gray circles. (e) Schematics of the Au(111) surface (gray circles) and the triangular trimers (black circles) located at the hollow sites. The scale bars are: (a) 1 nm, (b) 0.5 nm and (d) 0.5 nm.

The analysis of different regions of the as-grown system revealed important aspects of the structural properties of the triangular trimers. Fig. 6.6a depicts a region of the Au(111) surface with a large number of nanoclusters. In Fig. 6.6b, which is a magnification of Fig. 6.6a, one observes that these triangular trimers are located preferentially on the fcc regions of the distorted herringbone reconstruction. Some exceptions could be found and are marked with black circles in this image, indicating trimers on the hcp regions. In Fig. 6.6c an hcp region between two fcc regions is shown. This image reveals that triangular S trimers may present two types of orientations: pointing up (see Fig. 6.6d) and pointing down (Fig. 6.6e), similar to what was observed for the triangular TaS_2 islands. Our findings point out that these orientations are directly related to the regions of the modified Au(111) herringbone reconstruction where the trimers are found. For all the regions of our system analyzed, the pointing up triangular trimers are located at the fcc sites, while the pointing down trimers sit on hcp ones. In Fig. 6.6f a schematic model of the herringbone reconstruction, in which the hcp and the fcc regions of Au(111) are indicated, is shown. It is clear that the subatomic layer plays an important role on the orientation of the triangular S trimers (see scheme with green and yellow triangles in this panel). Here we have assumed that the S adatoms adsorb preferentially at hcp hollow sites with an fcc hollow site among them. This simple model explains the observation of distinct orientations on the hcp and fcc sites of Au(111). Through this phenomenological model one can conclude that the formation of triangular S trimers, pointing up or down, is favorable depending on the region of the Au(111) substrate where they are formed, which explains our experimental data. Moreover, as previously stated, the density of trimers pointing up is significantly larger than the ones pointing down. A counting of the investigated ensemble of triangular S trimers indicates a ratio of 93:7 (a total of 1103 trimers were analyzed).

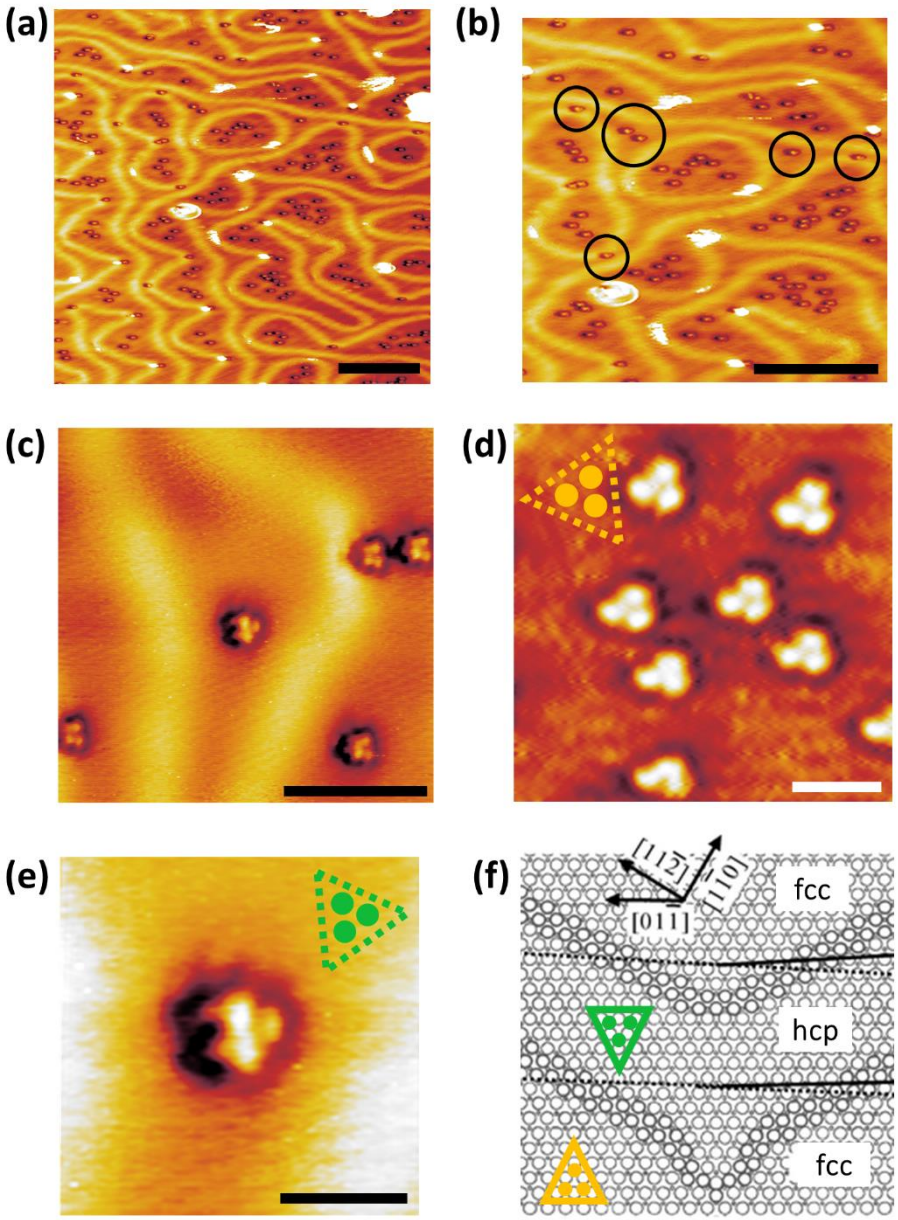

FIG. 6.6 – (a) STM topographic image of a number of triangular S trimers (bright dots) on Au(111). (b) Magnification of the region presented in (a). (c) A different region of the sample in which triangular trimers are found on hcp and fcc sites of the distorted herringbone reconstruction. An analysis of our system permitted us to identify trimers with two types of orientations: (d) pointing up and (e) pointing down. Pointing down trimers are minority in this region and are marked with black circles in panel (b), revealing that they are always located at hcp sites on Au(111). In inset panels (c) and (d) yellow and green triangles schematically indicate the orientation of trimers pointing up and down, respectively. (f) Scheme of the herringbone reconstruction. In this scheme yellow and green triangles indicate triangular trimers pointing up and down, respectively. Figure adapted from reference [203]. The scale bars are: (a) 10 nm, (b) 10 nm, (c) 3 nm, (d) 1 nm and (e) 1 nm.

In Fig. 6.7a another region of high density of triangular S trimers is presented. A tunneling spectrum was measured in this region and is depicted in Fig. 6.7b. For room temperature measurements, like the one presented here, this spectrum is, in fact, an average of the density of states of Au(111) and the trimers around the STM tip position. This tunneling spectrum is completely different from the STS of clean Au(111), presented in Fig. 6.1d, and the STS of TaS_2 islands shown in Fig. 6.3f. Here, one observes very well-defined peaks and a behavior of local density of states that resembles semiconductor systems, with a gap of 300 meV.

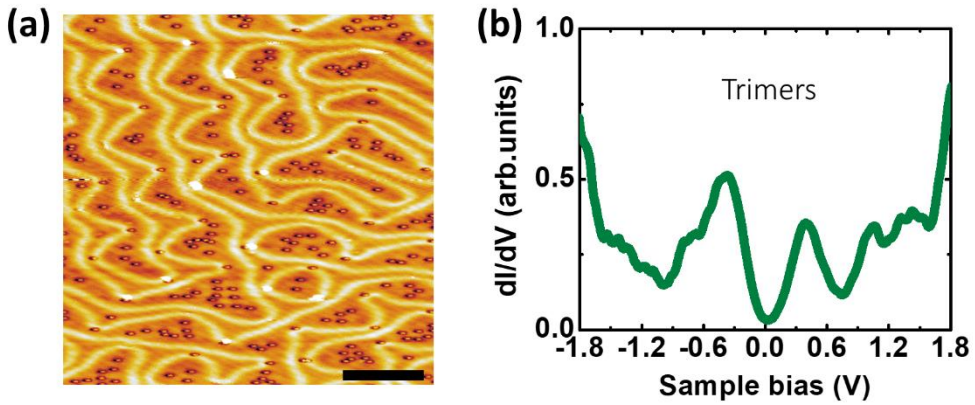

FIG. 6.7 – (a) STM topographic image of triangular S trimers on modified herringbone reconstructed Au(111). (b) Tunneling spectrum measured in this region, carried out on top of a triangular S trimer, in a position with large concentration of other triangular trimers. The scale bar is: (a) 10 nm.

Measurement of identical regions with different sample biases permit one to map out the electronic occupation of states of these triangular S trimers. In Fig. 6.8 two STM images measured at different tunneling conditions are presented. Similarly to what was measured for triangular graphene nanostructures in chapter IV, the differences observed in each panel are due to variations in the local density of states of the clusters. This is a strong evidence of how STM measurements are a combination between topography and the electronic properties of the system. In Fig. 6.8a, measured at -501 mV, the trimers appear as holes. Differently, in Fig. 6.8b, for the same region measured at -355 mV, the contrast is inverted and they appear as bulges. On the other hand, the distorted herringbone reconstructed region and an undefined adsorbate seen on the left side in

both images remain the same. This may be an evidence of the existence of confined states inside the trimers, which also confirms their semiconductor electronic behavior.

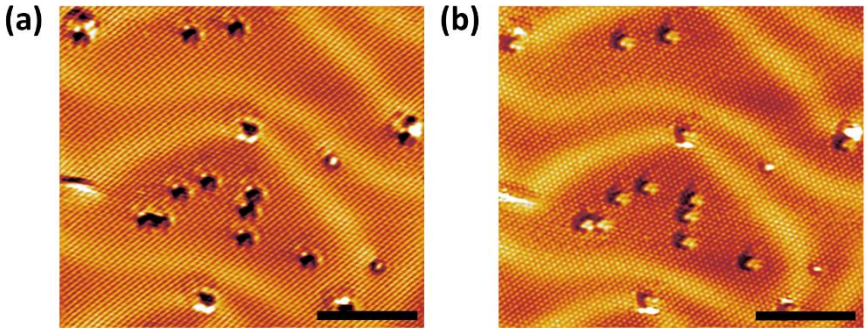

FIG. 6.8 – STM topographic image of triangular S trimers on Au(111). Both images were measured in identical regions, but using different sample biases. In (a) the sample bias used was -501 mV and in (b) -355 mV. One notices that triangular trimers appear in each image with distinct contrasts. The scale bar in both panels is 6 nm.

6.4 DISCUSSION

Walen et al. [211] also studied the self-organization of S adatoms on Au(111) using STM. Differently from our experiment, they reported the observation of an adlayer structure mainly formed by short one-dimensional rows of S atoms preferentially located on fcc regions. Density functional theory calculations were used to investigate the most stable configurations, which also included S-Au structures. At low coverage, these adsorbed species modify the herringbone reconstruction distorting it similarly to what is observed in this work. Furthermore, only about 10% of the adsorbed structures exist in a triangular form. However, in contrast with our experimental data, the distances among these adatoms is 0.494 nm, which is significantly larger than the value reported here. Also, trimers with different orientations could be found on the same sites.

In addition, Kurokawa and his co-workers [212] who studied a similar system, reported not only the adsorption of S adatoms on the surface of unreconstructed regions of Au(111), but also the observation of large structures (with 1 nm diameter), which they assigned to Au_3S_3 (this type of complex was not observed by Walen et al. [211]).

This set of evidences differs from our experimental observations most probably due to growth conditions. This made us use density functional theory to consider and

investigate different types of structures, even though less probable, starting with Ta adatoms adsorbed and embedded on Au(111). Our theoretical calculations are presented in next section.

6.5 THEORETICAL MODELING

The theoretical models were studied in collaboration with A. Samad and U. Schwingenschlögl (KAUST, Kingdom of Saudi Arabia). All calculations are based on non spin-polarized density functional theory (DFT), implemented in the Vienna Ab Initio Simulation Package. The generalized gradient approximation within the Perdew-Burke-Ernzerhof formalism was applied for the electron-electron exchange correlation potential [182], whereas the electron-ion interactions were processed through the projector augmented wave method [213]. All the STM images were plotted in XCrySDen programme [214]. Three different configurations were initially considered to investigate Ta adatoms adsorbed and embedded on Au(111), simulating different scenarios. In these calculations six layers of Au(111) were used always with the three bottom layers fixed. Additionally, the supercell of bare Au(111) had a dimension of 1.144 nm side.

In the first model three Ta atoms (represented in green) are absorbed on hcp hollow sites of the Au(111) surface (see Fig. 6.9a). In this configuration, the supercell used has 1.134 nm side. Simulated STM images of this structural pattern at 1 V are present in Fig. 6.9b. In this figure one observes a triangular pattern with the edges more intense, which does correspond properly to our experimental observations.

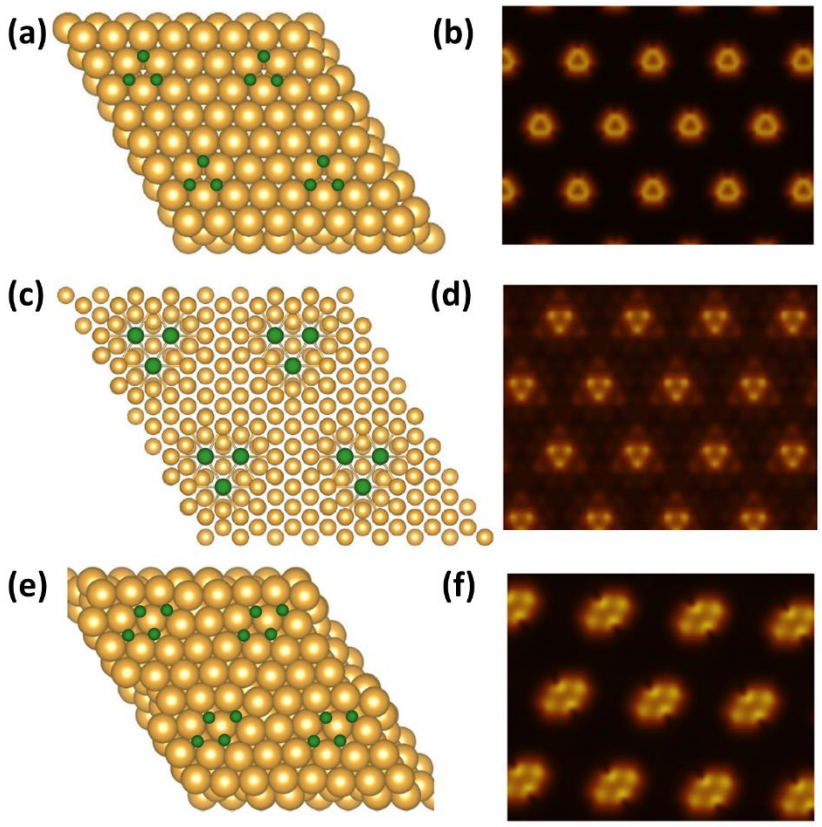

FIG. 6.9 – Structural models and simulated STM images at 1 V calculated by means of DFT for the following structures: (a, b) three Ta atoms adsorbed on hcp hollow sites of the Au(111); (c, d) three Ta atoms embedded on the Au(111); (e, f) four Ta atoms adsorbed on the hcp hollow sites of the Au(111). The Ta atoms are shown in green and the Au(111) substrate is shown in yellow.

In the second model three Ta atoms are embedded on the surface of the substrate as depicted in Fig. 6.9c. As a consequence of the insertion of Ta atoms in the Au(111) matrix, the symmetry of the surface is destroyed since the Ta atoms levels the top Au atoms. In this case the supercell has 1.104 nm side. The simulated STM image for this scenario is shown in Fig. 6.9d. As in the previous case, a triangular pattern is also observed. However, here three circular forms sit at the vertices of a triangle, which highly resembles the atomically-resolved STM images (see Fig. 6.5). The main problem of this model is that the distances between the Ta atoms do not completely correspond to our experimental observations.

Finally, the third and last calculated configuration is seen in Fig. 6.9e. Here, four Ta atoms are adsorbed on the hcp hollow sites of the Au(111) surface. The corresponding

STM image is depicted in Fig. 6.9f, in which one observes a four-fold symmetry not compatible with our measurements.

Even though, as previously discussed, our experimental data do not indicate that the triangular trimers are composed of Ta atoms this was a good starting point, especially considering the differences between our measurements and the results reported in literature. Further theoretical calculations considering S atoms on Au(111) are currently in progress to investigate this second scenario and its stability. This deeper theoretical analysis is beyond this Ph.D. work.

6.6 CONCLUSIONS

In summary, we have presented an experimental/theoretical study of TaS_2 films and self-assembled triangular nanoclusters on Au(111). A combination of scanning tunneling microscopy/spectroscopy and density functional theory were employed to investigate their structural and electronic properties. The sample was synthetized in situ by depositing tantalum onto Au(111) in an H_2S background, producing TaS_2 islands with a triangular morphology. The change in growth parameters, in particular, the increase of H_2S pressure and the annealing temperature modified the system, giving rise to a number of nanoclusters. The majority of these structures, which distort the herringbone reconstruction, is found to be located on fcc sites of the Au(111) surface. Atomically-resolved STM topographic images revealed that these nanoclusters have a well-defined triangular shape, with only two types of orientations, which depend on the regions of the Au(111) substrate where they are formed. Properties like orientation, average size and mean distances were systematically analyzed. In addition, DFT calculations of distinct configurations of Ta adsorbates and Ta atoms embedded on the substrate were presented. Further theoretical work will have to be carried out to study S atoms on Au(111), matching their electronic behavior.

VII.

SUMMARY AND OUTLOOKS

In this thesis a combination of experimental techniques was employed to investigate structural and electronic properties of three different layered materials: graphene, topological insulators and transition metal dichalcogenides. In summary, the first of the projects presented here aimed to study bilayer graphene films grown on SiC substrates. STM images permitted us to detect the presence of triangular graphene nanostructures that appeared as nanoholes and nanoplateaus. In order to explain the formation of these nanostructures a model based on stacking faults in SiC substrate was proposed. As a result of the presence of this type of defect, regions of high and low atomic density were formed in the SiC substrate. These structural modifications played an important role in the formation of the nanostructures since they influenced the surface dynamics during the growth process. Through tunneling spectra, we were able to characterize the electronic properties of a number of nanostructures which revealed distinct electronic responses, ranging from bilayer graphene to a behavior that resembles monolayer graphene systems. It is important to accentuate that these observations were addressed to an incomplete hydrogen intercalation scenario in which some regions of the bilayer graphene are still bonded to the substrate.

In the second project, the topological insulator Bi_4Te_3 was investigated. Here, we reported the synthesis of this material in the bulk form. This was confirmed through powder X-ray diffraction measurements, which also revealed the formation of minor

phases of Bi_2 and Bi_2Te_3. STM/STS allowed the identification of all these phases through the combined analysis of height-profiles and tunneling spectra. Our experimental findings are in agreement with our theoretical prediction calculated by means of density functional theory. In addition, DFT also predicted the existence of different surface states for the two terminations of this material, i. e. the bilayer- and the quintuple-layer terminated surfaces. ARPES measurements were carried out revealing that the major termination of the surface is Bi_4Te_3: QL. Snowflake-shaped with elongated branches at constant energy contours were also found for this system.

The third project studied in this thesis focused on TaS_2 films on Au(111) substrates. The sample was synthetized by depositing tantalum onto Au(111) in an H_2S background. The variation of the growth parameters, in particular, the use of high annealing temperatures and H_2S pressures, drastically modifies the as-grown system, reducing the amount of TaS_2 islands and giving rise to a number of triangular S trimers. Our experimental data showed that these nanostructures present distinct orientations depending on the region of the Au(111) herringbone reconstruction where they are located, i. e. at fcc or hcp sites. Orientation, average size and mean distances between trimers were systematically examined providing important information about the nature of this system.

Our findings open possibilities for further investigations and a number of other experiments. Regarding the triangular graphene nanostructures, one could still explore the recipe to synthetize these nanometer sized triangles. The growth variables, such as pressure, annealing temperatures and intercalation time, could be changed to verify how these nanostructures respond to these modifications. This could be checked through STM images of the as-grown samples. In addition, the role of the stacking faults on the emergence of triangular nanostructures could be studied. In this context, the use and investigation of SiC substrates with different densities of stacking faults would help to better understand the formation of nanostructures, improving the comprehension of the dynamics of the growth process. Synchrotron X-ray diffraction would be a valuable tool to investigate different substrates before and after the synthesis of graphene layers. This, together with STM measurements would considerably improve the control in the sample

preparation. Once a high standard control over the triangular nanostructures has been established their electronic properties could also be further investigated.

In what concerns the work on Bi_4Te_3 a publication discussing the ARPES results is in preparation. With ARPES measurements using synchrotron radiation it will be possible to differentiate bulk and surface states by varying the energy of the light source. This would also help in the investigation of the 'electronic topological gap' along the Γ-M direction. Spin-ARPES would provide important information about the physical nature of the warped constant energy contours and may reveal the existence of spin texture. Also, improvements in sample preparation can be achieved. The experimental setup (not shown or discussed here) can be modified to produce more homogeneous samples. This would result in the synthesis of single crystals not only of Bi_4Te_3, but also other topological insulators. For this, X-ray diffraction measurements would also be essential. Moreover, this system could be doped with different elements and one could also bombard its surface introducing point defects. Both cases would be interesting from the electronic point of view to explore how the properties of Bi_4Te_3 are modified under specific conditions.

Finally, regarding the TaS_2 on Au(111), additional DFT calculations will be necessary to further investigate the formation and stability of triangular S trimers on Au(111). With this information in hand additional investigations can be more easily proposed. About the TaS_2 monolayer on Au(111), intercalation using different elements would be an interesting idea to be further explored as an attempt to induce a phase change in the system, converting the 1H phase into the 1T phase.

VIII.

LIST OF PUBLICATIONS

The following list contains my publications and collaborations (chronologically organized) that were published or are in preparation to be submitted in a near future:

- Chagas, T., Cunha, T. H. R., Matos, M. J. S., dos Reis, D. D., Araujo, K. A. S., Malachias, A., Mazzoni, M. S. C., Ferlauto, A. S. & Magalhães-Paniago, R. Room temperature observation of the correlation between atomic and electronic structure of graphene on Cu(110). *RSC Advances.* **6**, 98001 (2016).

- Gonçalves, P. H. R., Chagas, T., Nascimento, V. B., dos Reis, D. D., Parra, C., Mazzoni, M. S. C., Malachias, A. & Magalhães-Paniago, R. Formation of Bi_xSe_y phases upon annealing of the topological insulator Bi_2Se_3: stabilization of in-depth bismuth bilayers. *J. Phys. Chem. Lett*. **9**, 954 (2018).

- Chagas, T., Pelc, M., Gonçalves, P. H. R., Antoniazzi, I., Gonzalez, J. W., Ayuela, A., Lopes, J. M. J., Oliveira Jr, M. H., Magalhães-Paniago, R. & Malachias, A. Self-assembled triangular graphene nanostructures: evidence of dual electronic behavior. *Carbon*, **142**, 580 (2019).

- Rosa, B. L. T., Parra-Murillo, C. A., Chagas, T., Garcia Junior, A. J., Guimarães, P. S. S., Deneke, Ch., Magalhães-Paniago, R. & Malachias, A. Scanning tunneling

measurements in membrane-based nanostructures: spatially-resolved quantum state analysis in postprocessed epitaxial systems for optoelectronic applications. *ACS Applied Nano Materials*, **2**, 4655 (2019).

- Gonçalves, P. H. R., Calil, L., Antoniazzi, I., Chagas, T., Malachias, A., Soares, E. A., de Carvalho, V. E., Miquita, D., Magalhães-Paniago, R. & Silva, W. S. Experimental realization of a quaternary Bi-chalcogenide topological insulator with smaller effective mass. *J. Phys. Chem. C*, **123**, 14398 (2019).

- Mendes, J. B. S., Alves Santos, O., Chagas, T., Magalhães-Paniago, R., Mori, T. J. A., Holanda, J., Meireles, L. M., Lacerda, R. G., Azevedo, A. & Rezende, S. M. Direct detection of induced magnetic moment and efficient spin-to-charge conversion in graphene/ferromagnetic structures. *Phys. Rev. B*, **99**, 214446 (2019).

- Chagas, T., Ribeiro, G. A. S., Gonçalves, P. H. R., Calil, L., Silva, W. S., Malachias, A., Mazzoni, M. S. C. & Magalhães-Paniago, R. Bi_2:Bi_2Te_3 stacking influence on the surface electronic response of the topological insulator Bi_4Te_3. *Electron. Struct.*, **2**, 015002 (2020).

- Antoniazzi, I., Chagas, T., Matos, M. J. S., Marçal, L. A. B., Soares, E. A., Mazzoni, M. S. C., Miwa, R. H., Lopes, J. M. J., Malachias, A., Magalhães-Paniago, R. & Oliveira Jr, M. H. Oxygen intercalated graphene on SiC(0001): multiphase SiOx layer formation and its influence on graphene electronic properties. *Carbon*, **167**, 746 (2020).

- Chagas, T., Ribeiro, G. A. S., Rosa, B. L. T., Bahrami, D., Davtyan, A., González, J. C., Magalhães-Paniago, R. & Malachias, A. Enhanced surface alloying and electronic properties of Mg-doped GaAs nanowires. (In preparation).

- Chagas, T., Silva, W. S., Ribeiro, G. A. S., Ashour, O. A., Li, Z., Louie, S. G., Petroff, Y. & Magalhães-Paniago, R. Multiple Dirac Cones and Fermi Velocity Renormalization on the Topological States of a Three-Dimensional Strong Topological Insulator Bi_4Te_3. (In preparation).

- Chagas, T., Mehlich, K., Cai, J., Samad, A., Schwingenschlögl, U. & Busse, C. Self-assembly of triangular S trimers. (In preparation).
- Cai, J., Silva, C., Jolie, W., Chagas, T., Mehlich, K., Duncan, D., Schlueter, C., Lee, T.-L. & Busse, C. Incorporation of K and Cs into hBN/Ir(111) and hBN/Ru(0001). (In preparation).
- Mehlich, K., Dombrowski, D., Chagas, T., Kurz, D., Michely, T. & Busse, C. In-plane heterostructures of transition metal dichalcogenide monolayers. (In preparation).

IX.

REFERENCES

[1] Geim, A. K. & Novoselov, K. S. The rise of graphene. *Nat. Mater.* **6**, 183 (2007).

[2] Novoselov, K. S., Fal'ko, V. I., Colombo, L., Gellert, P. R., Schwab, M. G. & Kim, K. A roadmap for graphene. *Nature* **490**, 192 (2012).

[3] Castro Neto, A. H., Guinea, F., Peres, N. M. R., Novoselov, K. S. & Geim, A. K. The electronic properties of graphene. *Rev. Mod. Phys.* **81**, 109 (2009).

[4] McCann, E. & Koshino, M. The electronic properties of bilayer graphene. *Rep. Prog. Phys.* **76**, 056503 (2013).

[5] Reina, A., Jia, X., Ho, J., Nezich, D., Son, H., Bulovic, V., Dresselhaus, M. S. & Kong, J. Large area, few-layer graphene films on arbitrary substrates by chemical vapor deposition. *Nano Lett.* **9**, 30 (2008).

[6] Chae, S. J., Gunes, F., Kim, K. K., Kim, E. S., Han, G. H., Kim, S. M., Shin, H., Yoon, S., Choi, J., Park, M. H., Yang, C. W., Pribat, D. & Lee, Y. H. Synthesis of large-area graphene layers on poly-nickel substrate by chemical vapor deposition: wrinkle formation. *Adv. Mater.* **21**, 2328 (2009).

[7] Sutter, E., Acharya, D. P., Sadowski, J. T. & Sutter, P. Scanning tunneling microscopy on epitaxial bilayer graphene on ruthenium (0001). *Appl. Phys. Lett.* **94**, 133101 (2009).

[8] Gao, L., Guest, J. R. & Guisinger, N. P. Epitaxial graphene on Cu(111). *Nano Lett.* **10**, 3512 (2010).

[9] Levy, N., Burke, S. A., Meaker, K. L., Panlasigui, M., Zettl, A., Guinea, F., Castro Neto, A. H. & Crommie, M. F. Strain-induced pseudo–magnetic fields greater than 300 Tesla in graphene nanobubbles. *Science* **329**, 544 (2010).

[10] Novoselov, K. S., Geim, A. K., Morozov, S. V., Jiang, D., Zhang, Y., Dubonos, S. V., Grigorieva, I. V. & Firsov, A. A. Electric field effect in atomically thin carbon films. *Science* **306**, 666 (2004).

[11] Novoselov K. S., Geim, A. K., Morozov, S. V., Jiang, D., Katsnelson, M. I., Grigorieva, I. V., Dubonos, S. V. & Firsov, A. A. Two-dimensional gas of massless Dirac fermions in graphene. *Nature* **438**, 197(2005).

[12] Morozov, S. V., Novoselov, K. S., Katsnelson, M. I., Schedin, F., Elias, D. C., Jaszczak, J. A. & Geim, A. K. Giant intrinsic carrier mobilities in graphene and its bilayer. *Phys. Rev. Lett.* **100**, 016602 (2008).

[13] Chen, J. H., Jang, C., Xiao, S. Ishigami, M. & Fuhrer, M. S. Intrinsic and extrinsic performance limits of graphene devices on SiO_2. *Nat. Nanotechnol.* **3**, 206 (2008).

[14] Akturk, A. & Goldsman, N. Electron transport and full-band electron-phonon interactions in graphene. *J. Appl. Phys.* **103**, 053702 (2008).

[15] Zhu, Y., Ji, H., Cheng, H.-M. & Ruoff, R. S. Mass production and industrial applications of graphene materials. *Natl. Sci. Rev.* **5**, 90 (2018).

[16] Balandin, A. A., Ghosh, S. Bao, W. Calizo, I., Teweldebrhan, D., Miao, F. & Lau, C. N. Superior thermal conductivity of single layer graphene. *Nano Lett*. **8**, 902 (2008).

[17] Li, Z., Wu, S., Lv, W., Shao, J. J., Kang, F. & Yang, Q. H. Graphene emerges as a versatile template for materials preparation. *Small* **12**, 2674 (2016).

[18] Frank, I. W., Tanenbaum, D. M. van der Zande, A. M. & McEuen, P. L. Mechanical

properties of suspended graphene sheets. *J. Vac. Sci. Technol. B* **25**, 2558 (2007).

[19] Ruffieux, P., Wang, S., Yang, B., Sánchez-Sánchez, C., Liu, J., Dienel, T., Talirz, L., Shinde, P., Pignedoli, C. A., Passerone, D., Dumslaff, T., Feng, X., Müllen, K. & Fasel, R. On-surface of graphene nanoribbons with zigzag edge topology. *Nature* **531**, 489 (2016).

[20] Lee, J., Wong, D., Velasco Jr., J., Rodriguez-Nieva, J. F., Kahn, S., Tsai, H.-Z., Taniguchi, T., Watanabe, K., Zettl, A., Wang, F., Levitov, L. S. & Crommie, M. F. Imaging electrostatically confined Dirac fermions in graphene quantum dots. *Nat. Phys.* **12**, 1032 (2016).

[21] Heerema, S. J., Vicarelli, L., Pud, S., Schouten, R. N., Zandbergen, H. W. & Dekker, C. Probing DNA translocations with inplane current signals in a graphene nanoribbon with a nanopore. *ACS Nano* **12**(3), 2623 (2018).

[22] Chen, Y.-C., Cao, T., Chen, C., Pedramrazi, Z., Haberer, D., de Oteyza, D. G., Fischer, F. R., Louie, S. G. & Crommie, M. F. Molecular bandgap engineering of the bottom-up synthesized graphene nanoribbon heterojunctions. *Nat. Nanotechnol.* **10**, 156 (2015).

[23] Magda, G. Z., Jin, X., Hagymási, I., Vancsó, P., Osváth, Z., Nemes-Incze, P., Hwang, C., Biró, L. P. & Tapasztó, L. Room-temperature magnetic order on zigzag edges of narrow graphene nanoribbons. *Nature* **514**, 608 (2014).

[24] Wang, J., Zhao, R., Yang, M., Liu, Z. & Liu, Z. Inverse relationship between carrier mobility and bandgap in graphene. *J. Chem. Phys.* **138**, 084701 (2013).

[25] Zhan, H., Guo, D. & Xie, G. Two-dimensional layered materials: from mechanical and coupling properties towards applications in electronics. *Nanoscale*, **11**, 13181 (2019).

[26] Moore, J. The birth of topological insulators. *Nature* **464**, 194 (2010).

[27] Fu, L. Topological crystalline insulators. *Phy. Rev. Lett.* **106**, 106802 (2011).

[28] Hasan, M. Z. & Kane, C. L. Colloquium: topological insulators. *Rev. Mod. Phys*. **82**,

3045 (2010).

[29] Bernevig, B. A., Hughes, T. L. & Zhang, S.-C. Quantum spin Hall effect and topological phase transition in HgTe quantum wells. *Science* **314**, 1757 (2006).

[30] König, M. Wiedmann, S., Brüne, C., Roth, A., Buhmann, Molenkamp, L. W., Qi, X.-L. & Zhang, S.-C. Quantum spin Hall insulator state in HgTe quantum wells. *Science* **318**, 766 (2007).

[31] Tian, W., Yu, W., Shi, J. & Wang, Y. The property, preparation and application of topological insulators: a review. *Materials* **10**, 814 (2017).

[32] Lin, Y. M., Rabin, O., Cronin, S. B., Ying, J. Y. & Dresselhaus, M. S. Semimetal-semiconductor transition in $Bi_{1-x}Sb_x$ alloy nanowires and their thermoelectric properties. *Appl. Phys. Lett*. **81**, 2403 (2002).

[33] Teo, J. C. Y., Fu, L. & Kane, C. L. Surface states and topological invariants in three-dimensional topological insulators: Application to $Bi_{1-x}Sb_x$. *Phys. Rev. B.* **78**, 045426 (2008).

[34] Zhang, W., Yu, R., Zhang, H.J., Dai, X. & Fang, Z. First-principles studies of the three-dimensional strong topological insulators Bi_2Te_3, Bi_2Se_3 and Sb_2Te_3. *New J. Phys*. **12**, 065013 (2010).

[35] Analytis, J. G., Chu, J.-H., Chen, Y., Corredor, F., McDonald, R. D., Shen, Z. X. & Fisher, I. R. Bulk Fermi surface coexistence with Dirac surface state in Bi_2Se_3: A comparison of photoemission and Shubnikov–de Haas measurements. *Phys. Rev. B* **81**, 205407 (2010).

[36] Chen, Y. L., Analytis, J. G., Chu, J.-H., Liu, Z. K., Mo, S.-K., Qi, X. L., Zhang, H. J., Lu, D. H., Dai, X., Fang, Z., Zhang, S. C., Fisher, I. R., Hussain, Z. & Shen, Z.-X. Experimental realization of a three-dimensional topological insulator Bi_2Te_3. *Science* **325**, 178 (2009).

[37] Wang, Q. H., Kalantar-Zadeh, K., Kis, A., Coleman, J. N. & Strano, M. S. Electronics and optoelectronics of two-dimensional transition metal dichalcogenides. *Nat Nanotechnol.* **7**, 699 (2012).

[38] Chhowalla, M., Shin, H. S., Eda, G., Li, L.-J., Loh, K. P. & Zhang, H. The chemistry of two-dimensional layered transition metal dichalcogenides nanosheets. *Nat. Chem.* **5**, 263 (2013).

[39] Manzeli, S., Ovchinnikov, D., Pasquier, D., Yazyev, O. V. & Kis, A. 2D transition metal dichalcogenides. *Nat. Rev. Mater*. **2**, 17033 (2017).

[40] Splendiani, A., Sun, L., Zhang, Y., Li, T., Kim, J., Chim, C.-Y., Galli, G. & Wang, F. Emerging photoluminescence in monolayer MoS_2. *Nano Lett.* **10**, 1271 (2010).

[41] Srivastava, A., Sidler, M., Allain, A., Lembke, D. S., Kis, A. & Imamoğlu, A. Optically active quantum dots in monolayer WSe_2. *Nat. Nanotechnol.* **10**, 491 (2015).

[42] Yin, Z., Li, H., Li, H., Jiang, L., Shi, Y., Sun, Y., Lu, G., Zhang, Q., Chen, X. & Zhang, H. Single-layer MoS_2 phototransistors. *ACS Nano*, **6**, 74 (2012).

[43] Klein, J., Lorke, M., Florian, M., Sigger, F., Wierzbowski, J., Cerne, J., Müller, K., Taniguchi, T., Watanabe, K., Wurstbauer, U., Kaniber, M., Knap, M., Schmidt, R., Finley, J. J. & Holleitner, A. W. Atomistic defect states as quantum emitters in monolayer MoS_2. arXiv:1901.01042 [cond-mat.mes-hall] (2019).

[44] Wilson, J. A. & Yoffe, A. D. The transition metal dichalcogenides discussion and interpretation of the observed optical, electrical and structural properties. *Adv. Phys.* **18**, 193 (1969).

[45] Rossnagel, K. On the origin of charge-density waves in select layered transition-metal dichalcogenides. *J. Phys.: Condens. Matter.* **23**, 213001 (2011).

[46] Sanders, C. E., Dendzik, M., Ngankeu, A. S., Eich, A., Bruix, A., Bianchi, M., Miwa, J. A., Hammer, B., Khajetoorians, A. A. & Hofmann, P. Crystalline and electronic structure of single-layer TaS_2. *Phys. Rev. B.* **94**, 081404(R) (2016).

[47] Kolobov, A. V. & Tominaga, J. Two-dimensional transition-metal dichalcogenides. Springer Series in Materials Science, 239. Springer, Cham (2016).

[48] Yu, J. H., Lee, H. R., Hong, S. S., Kong, D., Lee, H. W., Wang, H., Xiong, F., Wang,

S. & Cui, Y. Vertical heterostructure of two-dimensional MoS_2 and WSe_2 with vertically aligned layers. *Nano Lett.* **15**, 1031 (2015).

[49] Yu, Y., Hu, S., Su, L., Huang, L., Liu, Y., Jin, Z., Purezky, A. A., Geohegan, D. B., Kim, K. W., Zhang, Y. & Cao, L. Equally efficient interlayer exciton relaxation and improved absorption in epitaxial and non-epitaxial MoS_2/WS_2 heterostructures. *Nano Lett*. **15**, 486 (2015).

[50] Chen, K., Wan, X., Wen, J., Xie, W., Kang, Z., Zeng, X., Chen, H. & Xu, J. B. Electronic properties of MoS_2-WS_2 heterostructures synthesized with two-step lateral epitaxial strategy. *ACS Nano* **9**, 9868 (2015).

[51] Novoselov, K. S., Jiang, D., Schedin, F., Booth, T. J., Khotkevich, V. V., Morozov, S. V. & Geim, A. K. Two-dimensional atomic crystals. *Proc. Natl. Acad. Sci.* **102**, 10451 (2005).

[52] Press release. NobelPrize.org. Nobel Media AB 2020. Available on: <nobelprize.org/prizes/physics/2010/press-release/> Accessed on 26.03.2020.

[53] Castro Neto, A. H. Escola de altos estudos - CAPES. Física do grafeno: aspectos básicos e avançados. Graphene research center - National University of Singapure/ Boston University. Programa de Pós-Graduação em Física DF/UFMG. Video classes (2012).

[54] Castro Neto, A. H. Les houches notes on graphene. arxiv: 1004.3682 (2018).

[55] Advanced information. NobelPrize.org. Nobel Media AB 2020. Available on: <nobelprize.org/prizes/physics/2016/advanced-information/> Accessed on 26.03.2020.

[56] Coelho P. M., Ribeiro G. A. S., Malachias A., Pimentel V. L., Silva W. S., dos Reis D. D., Mazzoni M. S. C., Magalhães-Paniago R. Temperature-induced coexistence of a conducting bilayer and the bulk-terminated surface of the topological insulator Bi_2Te_3. *Nano Lett*. **13**, 4517 (2013).

[57] Gonçalves, P.H.R., Chagas, T., Nascimento, V.B., dos Reis, D.D., Parra, C., Mazzoni, M.S.C., Malachias, A. & Magalhães-Paniago, R. Formation of Bi_xSe_y

phases upon annealing of the topological insulator Bi_2Se_3: stabilization of in-depth bismuth bilayers, *J. Phys. Chem. Lett.* **9**, 954 (2018).

[58] Kane, C. L. Topological insulators: chapter 1. Topological band theory and the Z_2 invatiant. Elsevier Inc. Volume 6 of Contemporary concepts of condensed matter science (2013).

[59] Nakahara, M. Geometry, topology and physics. Bristol: Adam Hilger (1990).

[60] dos Reis, D. D. Estudo das estruturas atômicas de superfície dos isolantes topológicos Bi_2Se_3 e Bi_2Te_3, e de filmes finos de $La_{0.7}Sr_{0.3}MnO_3$. Ph.D. thesis. (2014).

[61] Thouless, D. J., Kohmoto, M., Nightingale, M. P. & den Nijs, M. Quantized Hall conductance in a two-dimensional periodic potential. *Phys. Rev. Lett*. **49**, 405 (1982).

[62] Thouless, D. J. Topological quantum numbers in nonrelativistic physics. World Scientific, Singapore (1998).

[63] Avron, J. E., Osadchy & D., Seiler, R. A topological look at the quantum Hall effect. *Phys. Today* **56**(8), 38 (2003).

[64] Qi, X.-L. & Zhang, S.-C. Topological insulators and superconductors. *Rev. Mod. Phys*. **83**, 1057 (2011).

[65] Zhang, S. C. Topological states of quantum matter. *Physics* **1**, 6 (2008).

[66] von Klitzing, K., Dorda, G. & Pepper, M. New method for high-accuracy determination of the fine-structure constant based on quantized Hall resistance. *Phys. Rev. Lett.* **45**, 494 (1980).

[67] Kohn, W. Theory of the insulating state. *Phys. Rev*. **133**, A171 (1964).

[68] Kane, C. L. & Mele, E. J. A new spin on the insulating state. *Science* **314**, 1692 (2006).

[69] von Klitzing, K. Developments in the quantum Hall effect. *Phil. Trans. R. Soc. A*

363, 2203 (2005).

[70] Paalanen, M. A., Tsui, D. C. & Gossard, A. C. Quantized Hall effect at low temperatures. *Phys. Rev. B*. 25, 5566(R) (1982).

[71] Laughlin, R. B. Quantized Hall conductivity in two dimensions. *Phys. Rev. B* 23, 5632 (1981).

[72] Kane, C. L. & Mele, E. J. Quantum spin Hall effect in graphene. *Phys. Rev. Lett.* 95, 226801 (2005);

[73] Kane, C. L. & Mele, E. J. Z_2 topological order and the quantum spin Hall effect. *Phys. Rev. Lett.* 95, 146802 (2005).

[74] Bernevig, B. A. & Zhang, S.-C. Quantum spin Hall effect. *Phys. Rev. Lett.* 96, 106802 (2006).

[75] Maciejko, J., Hughes, T. L. & Zhang, S.-C. The quantum spin Hall effect. *Annu. Rev. Condens. Matter Phys.* 2, 31 (2011).

[76] Qi, X. L. & Zhang, S.-C. The quantum spin Hall effect and topological insulators. *Phys. Today* 63(1), 33 (2010).

[77] Fu, L., Kane, C. L. & Mele, E. J. Topological insulators in three dimensions. *Phys. Rev. Lett.* 98, 106803 (2007).

[78] Moore, J. E. & Balents, L. Topological invariants of time-reversal-invariant band structures. *Phys. Rev. B*. 75, 121306(R) (2007).

[79] Roy, R. Topological phases and the quantum spin Hall effect in three dimensions. *Phys. Rev. B* 79, 195322 (2009).

[80] Hsieh, D., Qian, D., Wray, L., Xia, Y., Hor, Y. S., Cava,R. J. & Hasan, M. Z. A topological Dirac insulator in a quantum spin Hall phase. *Nature* 452, 970 (2008).

[81] Xia, Y., Qian, D., Hsieh, D., Wray, L., Pal, A., Lin, H., Bansil, A., Grauer, D., Hor, Y. S., Cava R. J. & Hasan, M. Z. Observation of a large-gap topological-insulator class with a single Dirac cone on the surface. *Nat. Phys.* 5, 398 (2009).

[82] Zhang, H., Liu, C.-X., Qi, X.-L., Dai, X.,Fang, Z. & Zhang, S.-C. Topological insulators in Bi_2Se_3, Bi_2Te_3 and Sb_2Te_3 with single Dirac cone on the surface. *Nat. Phys*. **5**, 435 (2009).

[83] Mishra, S. K., Satpathy, S. & Jepsen, O. Electronic structure and thermoelectric properties of bismuth telluride and bismuth selenide. *J. Phys.: Condens. Matter.* **9**, 461 (1997).

[84] Hor, Y. S., Richardella, A., Roushan, P., Xia, Y., Checkelsky, J. G., Yazdani, A., Hasan, M. Z., Ong, N. P. & Cava, R. J. p-type Bi_2Se_3 for topological insulator and low-temperature thermoelectric applications. *Phys. Rev. B* **79**, 195208 (2009).

[85] Navratil, J., Horak, J., Plechacek, T., Kamba, S., Lostak, P., Dyck, J. S., Chen, W. & Uher, C. Conduction band splitting and transport properties of Bi_2Se_3. *J. Solid State Chem.* **177**, 1704 (2004).

[86] Hsieh, D., Xia, Y., Qian, D., Wray, L., Dil, J. H., Meier, F., Osterwalder, J., Patthey, L., Checkelsky, J. G., Ong, N. P., Fedorov, A. V., Lin, H., Bansil, A., Grauer, D., Hor, Y. S., Cava, R. J. & Hasan, M. Z. A tunable topological insulator in the spin helical Dirac transport. *Nature* **460**, 1101 (2009).

[87] Vanderbilt, D. Berry phases in electronic structure theory. Electric polarization, orbital magnetization and topological insulators. Cambridge University Press (2018).

[88] Ringel, Z., Kraus, Y. E. & Stern, A. Strong side of weak topological insulators. *Phys. Rev. B* **86**, 045102 (2012).

[89] Radisavljevic, B., Radenovic, A., Brivio, J., Giacometti, V. & Kis, A. Single-layer MoS_2 transistors. *Nat. Nanotechnol.* **6**, 147 (2011).

[90] Dickinson, R. & Pauling L. The crystal structure of molybdenite. *J. Am. Chem. Soc.* **45**, 1466 (1923).

[91] Frindt, R. F. & Yoffe, A. D. Physical properties of layer structures: optical properties and photoconductivity of thin crystals of molybdenum disulphide. *Proc. R. Soc. A* **273**, 69 (1963).

[92] Mak, K. F., Lee, C., Hone, J., Shan, J. & Heinz, T. F. Atomically thin MoS_2: a new direct-gap semiconductor. *Phys. Rev. Lett.* **105**, 136805 (2010).

[94] Shao, B., Eich, A., Sanders, C., Ngankeu, A. S., Bianchi, M., Hofmann, P., Khajetoorians, A. A. & Wehling, T. O. Pseudodoping of a metallic two-dimensional material by the supporting substrate. *Nat. Commun.* **10**(1), 180 (2019).

[95] Yu, Y., Yang, F., Lu, X. F., Yan, Y. J., Cho, Y.-H., Ma, L., Niu, X., Kim, S., Son, Y.-W., Feng, D., Li, S., Cheong, S.-W., Chen, X. H. & Zhang, Y. Gate-tunable phase transitions in thin flakes of 1T-TaS_2. *Nat. Nanotechnol*. **10**, 270 (2015).

[96] Yan-Bin, Q., Yan-Lin, L., Guo-Hua, Z., Zhi, Z. & Xiao-Ying, Q. Anisotropic properties of TaS_2. *Chinese Phys*. 16, 3809 (2007).

[97] Binnig, G., Rohrer, H., Gerber, Ch. & Weibel, E. Surface studies by scanning tunneling microscopy. *Phys. Rev. Lett*. **49**, 57 (1982).

[98] Ballentine, L. E. Quantum mechanics: a modern development. World Scientific (1998).

[99] Julian Chen, C. Introduction to scanning tunneling microscopy. Oxford science publications. Oxford University Press (2008).

[100] Binning, G., Rohrer, H., Gerber, Ch. & Weibel, E. Tunneling through a controllable vacuum gap. *Appl. Phys Lett*. **40**, 178 (1982).

[101] Press release. NobelPrize.org. Nobel Media AB 2020. Available on: <nobelprize.org/prizes/physics/1986/press-release/> Accessed on 26.03.2020.

[102] Gottilieb, A. D. & Wesoloski, L. Bardeen's tunnelling theory as applied to scanning tunnelling microscopy: a technical guide to the traditional interpretation. *Nanotechnology*, **17**, R57–R65 (2016).

[103] Lounis, S. Theory of scanning tunneling microscopy. arXiv:1404.0961 [cond-mat.mes-hall] (2014).

[104] Umbach, T. R. Magnetic and electronic properties of supramolecular architectures on metal surfaces. Ph.D. thesis (2013).

[105] Braun, K. -F. & Rieder, K.-H. Engineering electronic lifetimes in artificial atomic structures. *Phys. Rev. Lett*., **88**, 096801 (2002).

[106] Jolie, W., Craes, F. & Busse, C. Graphene on weakly interacting metals: Dirac states versus surface states. *Phys. Rev. B*, **91**, 115419 (2015).

[107] Niebergall, L. Electron confinement in hexagonal vacancy islands: theory and experiment. *Phys. Rev. B*, **74**, 195436 (2006).

[108] Armen, G. B. Phase sensitive detection: the lock-in amplifier. Available on: <server1.phys.utk.edu/labs/modphys/Lock-In%20Amplifier%20Experiment.pdf> Accessed on 26.03.2020. (2008)

[109] Bentham Instruments Ltd. 225 Lock-in amplifier. Available on: <fis.unical.it/files/fl178/8014LockinF225.pdf> Accessed on 26.03.2020.

[110] Stanford Research Systems. About lock-In amplifiers. Available on: <thinksrs.com/downloads/PDFs/ApplicationNotes/AboutLIAs.pdf> Accessed on 26.03.2020.

[111] Huennekens, J. Lock-in amplifier and applications. Available on: <lehigh.edu/~jph7/website/Physics262/LockInAmplifierAndApplications.pdf> Accessed on 26.03.2020.

[112] Nunes, R. A. A., Albuquerque, M. P. & Albuquerque, M. P. O amplificador lock-in. Available on: <cbpf.br/~rastuto/pdf/NT-CBPF002-2006.pdf> Accessed on 26.03.2020. (2007).

[113] Gonçalves, P. H. R. Structural and electronic transformations upon heating of the topological insulator Bi_2Se_3. Master thesis (2018).

[114] Chagas, T. Estudo por microscopia/espectroscopia de tunelamento e difração de raios X da correlação entre propriedades estruturais e eletrônicas de grafeno epitaxial sobre cobre. Master thesis (2016).

[115] Chagas, T., Cunha, T. H. R., Matos, M. J. S., dos Reis, D. D., Araujo, K. A. S., Malachias, A., Mazzoni, M. S. C., Ferlauto, A. S. & Magalhães-Paniago, R. Room temperature observation of the correlation between atomic and electronic structure of graphene on Cu(110). *RSC Advances* **6**, 98001 (2016).

[116] Einstein, A. *Ann. Physik* **17**, 132 (1905).

[117] The Nobel Prize in Physics 1921. NobelPrize.org. Nobel Media AB 2020. Available on: <nobelprize.org/prizes/physics/1921/summary/> Accessed on 26.03.2020.

[118] Eisberg, R. & Resnick, R. Física Quântica – Átomos, moléculas, sólidos, núcleos e partículas. Campus (1994).

[119] Simões e Silva, W. Estudos das propriedades morfológicas e eletrônicas em: interfaces grafeno/metal e isolantes topológicos. Ph.D. thesis (2014).

[120] Damascelli, A., Hussain, Z. & Shen, Z. Angle-resolved photoemission studies of the cuprate superconductors. *Rev. Mod. Phys*, **75**, 473 (2003).

[121] Guinea, F., Castro Neto, A. H. & Peres, N. M. R. Electronic properties of stacks of graphene layers. *Solid State Commun.* **143**, 116 (2007).

[122] Zhou, S. Y. Gweon, G.-H., Fedorov, A. V. , First, P. N., de Heer, W. A., Lee, D.-H., Guinea, F., Castro Neto, A. H. & Lanzara, A. Substrate-induced bandgap opening in epitaxial graphene. *Nat. Mater.* **6**, 770 (2007).

[123] Sutter, P., Sadowski, J. T. & Sutter, E. Graphene on Pt(111): growth and substrate interaction. *Phys. Rev. B* **80**, 245411 (2009).

[124] Wang, Y. Y., Ni, Z. H., Yu, T., Shen, Z. X., Wang, H. M., Wu, Y. H., Chen, W. & Wee, A. T. S. Raman studies of monolayer graphene: the substrate effect. *J. Phys. Chem. C* **112**, 10637 (2008).

[125] Li, X., Cai, W., Na, J., Kim, S., Nah, J., Yang, D., Piner, R., Velamakanni, A., Jung, I., Tutuc, E., Banerjee, S. K., Colombo, L. & Ruoff, R. S. Large-area synthesis of high-quality and uniform graphene films on copper foils. *Science* **324**, 1312 (2009).

[126] Wood, J. D., Schmucker, S. W., Lyons, A. S., Pop, E. & Lyding, J. W. Effects of polycrystalline Cu substrate on graphene growth by chemical vapor deposition. *Nano Lett.* **11**, 4547 (2011).

[127] de Heer, W. A., Berger, C., Ruan, M., Sprinkle, M., Li, X., Hu, Y., Zhang, B., Hankinson, J. & Conrad, E. Large area and structured epitaxial graphene produced by confinement controlled sublimation of silicon carbide. *Proc. Natl. Acad. Sci.* **108**, 16900 (2011).

[128] Robinson, J., Weng, X., Trumbull, K., Cavalero, R., Wetherington, M., Frantz, E., LaBella, M., Hughes, Z., Fanton, M. & Snyder, D. Nucleation of epitaxial graphene on SiC (0001). *ACS Nano* **4**, 153 (2009).

[129] Riedl, C., Coletti, C., Iwasaki, T., Zakharov, A. A. & Starke, U. Quasi-free-standing epitaxial graphene on SiC obtained by hydrogen intercalation. *Phys. Rev. Lett.* **103**, 246804 (2009).

[130] Oliveira Jr., M. H. Schumann, T., Fromm, F., Koch, R., Ostler, M., Ramsteiner, M., Seyller, T., Lopes, J. M. J. & Riechert, H. Formation of high-quality quasi-free-standing bilayer graphene on SiC(0001) by oxygen intercalation upon annealing in air. *Carbon* **52**, 83 (2013).

[131] Strupinski, W., Grodecki, K., Wysmolek, A., Stepniewski, R., Szkopek, T., Gaskell, P. E., Grüneis, A., Haberer, D., Bozek, R., Krupka, J. & Baranowski, J. M. Graphene epitaxy by chemical vapor deposition on SiC. *Nano Lett.* **11**, 1786 (2011).

[132] Berger, C., Song, Z., Li, T., Li, X., Ogbazghi, A. Y., Feng, R., Dai, Z., Marchenkov, A. N., Conrad, E. H., First, P. N. & de Heer, W. A. Ultrathin epitaxial graphite: 2D electron gas properties and a route toward graphene-based nanoelectronics. *J. Phys. Chem. B* **108**, 19912 (2004).

[133] Kulkarni, G. S., Reddy, K., Zhong, Z. & Fan, X. Graphene nanoelectronic heterodyne sensor for rapid and sensitive vapour detection. *Nat. Commun.* **5**, 4376 (2014).

[134] Du, X., Skachko, I., Barker, A. & Andrei, E. Y. Approaching ballistic transport in suspended graphene. *Nat. Nanotechnol.* **3**, 491 (2008).

[135] Oostinga, J. B., Heersche, H. B., Liu, X., Morpurgo, A. F. & Vandersypen, L. M. K. Gate-induced insulating state in bilayer graphene devices. *Nat. Mater.* **7**, 151 (2008).

[136] Yazdi, G., Iakimov, T. & Yakimova, R. Epitaxial Graphene on SiC: A Review of Growth and Characterization. *Crystals* **6**, 53 (2016).

[137] Riedl, C., Coletti, C. & Starke, U. Structural and electronic properties of epitaxial graphene on SiC(0001): a review of growth, characterization, transfer doping and hydrogen intercalation. *J. Phys. D: Appl. Phys.* **43**, 374009 (2010).

[138] Son, Y. W., Cohen, M. L. & Louie, S. G. Energy gaps in graphene nanoribbons. *Phys. Rev. Lett.* **97**, 216803 (2006).

[139] Han, M. Y., Ozyilmaz, B., Zhang, Y. & Kim, P. Energy band-gap engineering of graphene nanoribbons. *Phys. Rev. Lett.* **98**, 206805 (2007).

[140] Tapasztó, L., Dobrik, G., Lambin, P. & Biró, L. P. Tailoring the atomic structure of graphene nanoribbons by scanning tunnelling microscope lithography. *Nat. Nanotechnol.* **3**, 397 (2008).

[141] Phark, S. H., Borme, J., Vanegas, A. L., Corbetta, M., Sander, D. & Kirschner, J. Direct observation of electron confinement in epitaxial graphene nanoislands. *ACS Nano* **5**, 8162 (2011).

[142] Fernández-Rossier, J. & Palacios, J. J. Magnetism in graphene nanoislands. *Phys. Rev. Lett.* **99**, 177204 (2007).

[143] Eom, D. Prezzi, D., Rim, K. T., Zhou, H., Lefenfeld, M., Xiao, S., Nuckolls, C., Hybertsen, M. S., Heinz, T. F. & Flynn, G. W. Structure and electronic properties of graphene nanoislands on Co(0001). *Nano Lett.* **9**, 2844 (2009).

[144] Peng, J., Gao, W., Gupta, B. K., Liu, Z., Romero-Aburto, R., Ge, L., Song, L., Alemany, L. B., Zhan, X., Gao, G., Vithayathil, S. A., Kaipparettu, B. A., Marti, A.

A., Hayashi, T., Zhu, J.-J. & Ajayan, P. M. Graphene quantum dots derived from carbon fibers. *Nano Lett.* **12**, 844 (2012).

[145] da Costa, D. R., Zarenia, M., Chaves, A., Farias, G. A. & Peeters, F. M. Energy levels of bilayer graphene quantum dots. *Phys. Rev. B* **92**, 115437 (2015).

[146] Bolen, M. L., Harrison, S. E., Biedermann, L. B. & Capano, M. A. Graphene formation mechanisms on 4H-SiC(0001). *Phys. Rev. B* **80**, 115433 (2009).

[147] Emtsev, K. V., Speck, F., Seyller, T., Ley, L. & Riley, J. D. Interaction, growth, and ordering of epitaxial graphene on SiC{0001} surfaces: a comparative photoelectron spectroscopy study. *Phys. Rev. B* **77**, 155303 (2008).

[148] Mattausch, A. & Pankratov, O. Ab initio study of graphene on SiC. *Phys. Rev. Lett.* **99**, 076802 (2007).

[149] Ferrari, A. C., Meyer, J. C., Scardaci, V., Casiraghi, C., Lazzeri, M., Mauri, F., Piscanec, S., Jiang, D., Novoselov, K. S., Roth, S. & Geim, A. K. Raman spectrum of graphene and graphene layers. *Phys. Rev. Lett.* **97**, 187401 (2006).

[150] Graf, D., Molitor, F., Ensslin, K., Stampfer, C., Jungen, A., Hierold, C., & Wirtz, L. Spatially resolved Raman spectroscopy of single- and few-layer graphene. *Nano Lett*. **7**, 238 (2007).

[151] Malard, L. M., Nilsson, J., Elias, D. C., Brant, J. C., Plentz, F., Alves, E. S., Castro Neto, A. H. & Pimenta, M. A. Probing the electronic structure of bilayer graphene by Raman scattering. *Phys. Rev. B* **76**, 201401(R) (2007).

[152] Robinson, J. A., Puls, C. P., Staley, N. E., Stitt, J. P., Fanton, M. A., Emtsev, K. V., Sevller, T. & Liu, Y. Raman topography and strain uniformity of large-area epitaxial graphene. *Nano Lett.* **9**, 964 (2009).

[153] Lauffer, P., Emtsev, K. V., Graupner, R., Seyller, Th., Ley, L. Reshanov, S. A. & Weber, H. B. Atomic and electronic structure of few-layer graphene on SiC(0001) studied with scanning tunneling microscopy and spectroscopy. *Phys. Rev. B* **77**, 155426 (2008).

[154] Borovikov, V. & Zangwill, A. Step-edge instability during epitaxial growth of graphene from SiC(0001). *Phys. Rev. B* **80**, 121406(R) (2009).

[155] Powell, A. R. & Rowland, L. B. SiC Materials – Progress, Status, and Potential Roadblocks. *Proceedings of the IEEE* **90**, 942 (2002).

[156] Kimoto, T. & Matsunami, H. Surface diffusion lengths of adatoms on 6H-SiC{0001} faces in chemical vapor deposition of SiC. *J. Appl. Phys.* **78**, 3132 (1995).

[157] Mammadov, S., Ristein, J., Koch, R. J., Ostler, M., Raidel, C., Wanke, M., Vasiliauskas, R., Yakimova, R. & Seyller, T. Polarization doping of graphene on silicon carbide. *2D Mater.* **1**, 035003 (2014).

[158] Schumann, T., Dubslaff, M., Oliveira Jr., M. H., Hanke, M., Lopes, J. M. J. & Riechert, H. Effect of buffer layer coupling on the lattice parameter of epitaxial graphene on SiC(0001). *Phys. Rev. B* **90**, 041403 (2014).

[159] Schmidt, D. A., Ohta, T. & Beechem, T. E. Strain and charge carrier coupling in epitaxial graphene. *Phys. Rev. B* **84**, 235422 (2011).

[160] Ristein, J., Mammadov, S. & Seyller, Th. Origin of doping in quasi-free-standing graphene on silicon carbide. *Phys. Rev. Lett*. **108**, 246104 (2012).

[161] Chico, L., Benedict, L. X., Louie, S. G. & Cohen, M. L. Quantum conductance of carbon nanotubes with defects. *Phys. Rev. B* **54**, 2600 (1996).

[162] González, J. W., Rosales, L., Pacheco, M. & Ayuela, A. Electron confinement induced by diluted hydrogen-like ad-atoms in graphene ribbons. *Phys. Chem. Chem. Phys.* **17**, 24707e24715 (2015).

[163] Datta, S. Electronic Transport in Mesoscopic Systems. Cambridge University Press, Cambridge (1995).

[164] Varchon, F., Feng, R., Hass, J., Li, X., Ngoc Nguyen, B., Naud, C., Mallet, P., Veuillen, J.-Y., Berger, C., Conrad, H. & Magaud, L. Electronic structure of

epitaxial graphene layers on SiC: effect of the substrate. *Phys. Rev. Lett.* **99**, 126805 (2007).

[165] Mattausch, A. & Pankratov, O. Density functional study of graphene overlayers on SiC, *Phys. Status Solidi B* **245**, 1425e1435 (2008).

[166] Urazhdin, S., Bilc, D., Mahanti, S. D. & Tessmer, S. H. Surface effects in layered semiconductors Bi_2Se_3 and Bi_2Te_3. *Phys. Rev. B* **69**, 085313 (2004).

[167] Xu, S.-Y., Belopolski, I., Alidoust, N., Neupane, M., Bian, G., Zhang, C., Sankar, R., Chang, G., Yuan, Z., Lee, C.-C., Huang, S.-M., Zheng, H., Ma, J., Sanchez, D. S., Wang, B., Bansil, A., Chou, F., Shibayev, P. P., Lin, H., Jia, S. & Hasan, M. Z. Topological matter: discovery of a Weyl fermion semimetal and topological Fermi arcs. *Science* **349**, 613 (2015).

[168] Gibson, Q. D., Schoop, L. M., Weber, A. P., Ji, H., Nadj-Perge, S., Drozdov, I. K., Beidenkopf, H., Sadowski, J. T., Fedorov, A., Yazdani, A., Valla, T. & Cava, R. J. Termination-dependent topological surface states of the natural superlattice phase Bi_4Se_3. *Phys. Rev. B* **88**, 081108R (2013).

[169] Weber, A. P., Gibson, Q. D., Ji, H., Caruso, A. N., Fedorov, A. V., Cava, R. J. & Valla, T. Gapped surface states in a strong-topological-insulator material. *Phys. Rev. Lett.* **114**, 256401 (2015).

[170] Hatsuta, N., Takemori, D. & Takashiri, M. Effect of thermal annealing on thevstructural and thermoelectric properties of electrodeposited antimony telluride thin films *J.Alloys Compd.* **685**, 147 (2016).

[171] Singkaselit, K., Sakulkalavek, A. & Sakdanuphab, R. Effects of annealing temperature on the structural, mechanical and electrical properties of flexible bismuth telluride thin films prepared by high pressure RF magnetron sputtering *Adv. Nat. Sci: Nanosci. Nanotechnol.* **8**, 035002 (2017).

[172] Parra C., Cunha, T. H. R., Contryman, A. W., Kong, D., Montero-Silva, F., Gonçalves, P. H. R., dos Reis, D. D., Giraldo-Gallo, P., Segura, R., Olivares, F., Niestemski, F., Cui, Y., Magalhães-Paniago, R. & Manoharan, H. C. Phase

separation of Dirac electrons in topological insulators at the spatial limit. *Nano Lett.* **17**, 97 (2017).

[173] Babanlya, M. B., Chulkovb, E. V., Alieve, Z. S., Shevelkovf, A. V. & Amiraslanovg, I. R. Phase diagrams in materials science of topological insulators based on metal chalcogenides. *Russ. J. Inorg. Chem.* **63**, 1703 (2017).

[174] Bos, J. W. G., Zandbergen, H. W., Lee, M. H., Ong, N. P. & Cava, R. J. Structure and thermoelectric properties of the infinitely adaptive series $(Bi_2)_m(Bi_2Te_3)_n$. *Phys. Rev. B* **75**, 195203 (2007).

[175] Hewit, A. S. & Wang, J. Coexisting Bi and Se surface terminations of cleaved Bi_2Se_3 single crystals. *J. Vac. Sci. Technol. B* **32**, 04E103 (2014).

[176] Shokri, R., Meyerheim, H. L., Roy, S., Mohseni, K., Ernst, A., Otrokov, M. M., Chulkov, E. V. & Kirschner, J. Atomic and electronic structure of bismuth-bilayer-terminated Bi_2Se_3(0001) prepared by atomic etching. *Phys. Rev. B* **91**, 205430 (2015).

[177] Hohenberg, P. & Kohn, W. Inhomogeneous electron gas. *Phys. Rev*. **136**, B864 (1964).

[178] Kohn, W. & Sham, L. J. Self-consistent equations including exchange and correlation effects. *Phys. Rev.* **140** A1133 (1965).

[179] Ozaki, T., Kino, H., Yu, J., Han, M. J., Kobayashi, N., Ohfuti, M., Ishii, F., Ohwaki, T., Weng, H. & Terakura, K. OpenMX. Available on: <openmx-square.org/> Accessed on 26.03.2020. (2009).

[180] Theurich, G. & Hill, N. A. Self-consistent treatment of spin-orbit coupling in solids using relativistic fully separable *ab initio* pseudopotentials *Phys. Rev. B* **64**, 073106 (2001).

[181] Ozaki, T. Variationally optimized atomic orbitals for large-scale electronic structures *Phys. Rev. B* **67**, 155108 (2013).

[182] Perdew, J. P., Burke, K. & Ernzerhof, M. Generalized gradient approximation made simple. *Phys. Rev. Lett*. **77**, 3865 (1996).

[183] Monkhorst, H. J. & Pack, J. D. Special points for Brillouin-zone integrations *Phys. Rev. B* **13**, 5188 (1976).

[184] Yamana, K., Kihara, K. & Matsumoto, T. Bismuth tellurides: BiTe and Bi_4Te_3. *Acta Cryst.* **B35**, 147 (1979).

[185] Yang, F., Miao, L., Wang, Z. F., Yao, M.-Y., Zhu, F., Song, Y. R., Wang, M.-X., Xu, J.-P., Fedorov, A. V., Sun, Z., Zhang, G. B., Liu, C., Liu, F., Qian, D., Gao, C. L., Jia & J.-F. Spatial and energy distribution of topological edge states in single Bi(111) bilayer. *Phys Rev. Lett*. **109**, 016801 (2012).

[186] Alpichshev, Z., Analytis, J. G., Chu, J.-H., Fisher, I. R., Chen, Y. L., Shen, Z. X., Fang, A. & Kapitulnik, A. STM imaging of electronic waves on the surface of Bi_2Te_3: topologically protected surface states and hexagonal warping effects *Phys. Rev Lett.* **104**, 016401 (2010).

[187] Granstrom, C. R., Fridman, I., Lei, H.-C., Petrovic, C. & Wei, J. Y. T. Andreev reflection spectroscopy on Bi_2X_3 (X = Se, Te) topological insulators: implications for the c-axis superconducting proximity effect. arXiv:1711.00144 (2017).

[188] Kuroda, K., Arita, M., Miyamoto, K., Ye, M., Jiang, J., Kimura, A., Krasovskii, E. E., Chulkov, E. V., Iwasawa, H., Okuda, T., Shimada, K., Ueda, Y., Namatame, H. & Taniguchi, M. Hexagonally deformed Fermi surface of the 3D topological insulator Bi_2Se_3. *Phys. Rev. Lett*. **105**, 076802 (2010).

[189] Xu, S.-Y., Wray, L. A., Xia, Y., von Rohr, F., Hor, Y. S., Dil, J. H., Meier, F., Slomski, B., Osterwalder, J., Neupane, M., Lin, H., Bansil, A., Fedorov, A., Cava, R. J. & Hasan M. Z. Realization of an isolated Dirac node and strongly modulated: spin texture in the topological insulator Bi_2Te_3. arXiv:1101.3985 [cond-mat.mes-hall] (2011).

[190] Klimovskikh, I. I., Sostina, D., Petukhov, A., Rybkin, A. G., Eremeev, S. V., Chulkov, E. V., Tereshchenko, O. E., Kokh, K. A., & Shikin A. M. Spin-resolved band

structure of heterojunction Bi-bilayer/3D topological insulator in the quantum dimension regime in annealed $Bi_2Te_{2.4}Se_{0.6}$. *Sci. Rep.* **7**, 45797 (2017).

[191] Brouet, V., Yang, W. L., Zhou, X. J., Hussain, Z., Moore, R. G., He, R., Lu, D. H., Shen, Z. X., Laverock, J., Dugdale, S., Ru, N. & Fisher, I. R. ARPES study of the evolution of band structure and charge density wave properties in RTe3 for R = Y, La, Ce, Sm, Gd, Tb and Dy. arXiv:0801.2672 [cond-mat.str-el] (2008).

[192] Wise, W. D., Boyer, M. C., Chatterjee, K., Kondo, T., Takeuchi, T., Ikuta, H., Wang, Y. & Hudson, E. W. Charge-density-wave origin of cuprate checkerboard visualized by scanning tunnelling microscopy. *Nat. Phys.* **4**, 696 (2008).

[193] Fu, L. Hexagonal warping effects in the surface states of the topological insulator Bi_2Te_3. *Phys. Rev. Lett*. **103**, 266801 (2009).

[194] Hasan, M. Z., Lin, H. & Bansil, A. Viewpoint: warping the cone on a topological insulator. *Physics* **2**, 109 (2009).

[195] Pizzi, G., Vitale, V., Arita, R., Blügel, S., Freimuth, F., Géranton, G., Gibertini, M., Gresch, D., Johnson, C., Koretsune, T., Ibañez-Azpiroz, J., Lee, H., Lihm, J. M., Marchand, D., Marrazzo, A., Mokrousov, Y., Mustafa, J. I., Nohara, Y., Nomura, Y., Paulatto, L., Poncé, S., Ponweiser, T., Qiao, J., Thöle, F., Tsirkin, S. S., Wierzbowska, M., Marzari, N., Vanderbilt, D., Souza, I., Mostofi, A. A., & Yates, J. R. Wannier90 as a community code: new features and application. *J. Phys. Cond. Matt.* **32**, 165902 (2020).

[196] Wu, Q., Zhang, S., Song, H.-F., Troyer, M. & Soluyanov, A. A. WannerTools: an open-source software for novel topological materials. *Compt. Phys. Commun.* **224**, 405 (2018).

[197] Kleinert, M., Waibel, H.-F., Engelmann, G. E., Martin, H. & Kolb, D. M. Co deposition on Au(111) and Au(100) electrodes: an in situ STM study. *Electrochim. Acta* **46**, 3129 (2001).

[198] Waibel, H.-F., Kleinert, M., Kibler, L. A. & Kolb, D. M. Initial stages of Pt deposition on Au(111) and Au(100). *Electrochim. Acta* **47**, 1461 (2002).

[199] Ohresser, P. & Brookes, N. B. Magnetism of small Fe clusters on Au(111) studied by x-ray magnetic circular dichroism. *Phys. Rev. B* **64**, 104429 (2001).

[200] Bezerra-Neto, M. M., Ribeiro, M. S., Sanyal, B., Bergman, A., Muniz, R. B., Eriksson, O. & Klautau, A. B. Complex magnetic structure of clusters and chains of Ni and Fe on Pt(111). *Sci. Rep.* **3**, 3054 (2013).

[201] Corcoran, S. G. & Chaarova, G. S. Na in-situ STM investigation of the underpotential deposition of Ag on Au(111) electrodes. *J. Electroanal. Chem.* **377**, 85 (1994).

[202] Fratesi, G. First-principles investigaton of the early stages of Pd adsorption on Au(111). *J. Phys. Condens. Matter.* **23**, 015001 (2011).

[203] Xie, Z.-X., Huang, Z.-F. & Xu., X. Influence of reconstruction on the structure of self-assembled normal-alkane monolayers on Au(111) surfaces. *Phys. Chem. Chem. Phys.* **4**, 1486 (2002).

[204] Wöll, Ch., Chiang, S., Wilson, R. J. & Lippel, P. H. Determination of atom positions at stacking-fault dislocations on Au(111) by scanning tunneling microscopy. *Phys. Rev. B* **39**, 7988 (1989).

[205] Chambliss, D. D., Wilson, R. J. & Chiang, S. Nucleation of ordered Ni island arrays on Au(111) by surface-lattice dislocations. *Phys. Rev. Lett.* **66**, 1721 (1991).

[206] Dakkouri, A. S. & Kolb, D. M. Interfacial electrochemistry: experimental, theory and applications. Ed. by Wieckowski, A. & Dekker, M. New York 151 (1999).

[207] Kevan, S. D. & Gaylord, R. H. High-resolution photoemission study of the electronic structure of the noble-metal (111)surfaces. *Phys. Rev. B* **36**, 5809 (1987).

[208] Mehlich, K. In-plane heterostructures in transition metal dichalcogenide monolayers. Master thesis (2019).

[209] Horcas, I., Fernandez, R., Gomez-Rodriguez, J. M., Colchero, J., Gomez-Herrero, J. & Baro, A. M. WSXM: A software for scanning probe microscopy and a tool for nanotechnology. *Rev. Sci. Instrum.* **78**, 013705 (2007).

[210] Ziliang, S. & Lin, N. Porphyrin-based two-dimensional coordination Kagome lattice self-assembled on a Au(111) surface. *J. Am. Chem. Soc.* **131**, 5376 (2009).

[211] Walen, H., Liu, D.-A., Oh, J., Lim, H., Evans, J., W., Kim, Y. & Thiel, P. A. Self-organization of S adatoms on Au(111): √3R30° rows at low coverage. *J. Chem. Phys.* **143**, 014704 (2015).

[212] Kurokawa, S., Miyawaki, Y. & Sakai, A. Scanning tunneling microscopy observation of sulfur adsorbates on Au(111) at liquid nitrogen temperature. *Jpn. J. Appl. Phys.* **48**, 08JB12 (2009).

[213] Kresse, G. & Furthmüller, J. Efficient iterative schemes for *ab initio* total-energy calculations using a plane-wave basis set. *Phys. Rev. B* **54**, 11169 (1996).

[214] Kokalj, A. XCrySDen - a new program for displaying crystalline structures and electron densities. *J. Mol. Graph. Modelling* **17**, 176 (1999).